Antal Kerpely Doctoral School of Materials Science and Technology

Experimental and Numerical Investigations on Thermal Application of Nanofluids

PhD dissertation

By
Thong Le Ba
MSc in Chemical Engineering

Supervisor
Prof. Imre Miklós Szilágyi, PhD
Institute of Physical Metallurgy, Metal Forming and Nanotechnology

Head of the Doctoral School
Prof. Valéria Mertinger, DSc

Miskolc, 2026

Statement of the supervisor

I, Prof. Dr. Imre Miklós Szilágyi as the supervisor, hereby declare that the thesis written by Thong Le Ba (Neptun code: HH9XL1) titled “Numerical and experimental investigation on thermal applications of nanofluids” is his own writing and that Isupported his work with regular consultations. I also declare that the thesis meets the formaland professional requirements of the University of Miskolc and those of the Antal Kerpely Doctoral School of Materials Science and Technology, thus I support its submission.

(Miskolc, 2026.04.08)

Prof. Dr. Imre Miklós Szilágyi

Table of Contents

Nomenclatures

Symbol	**Description**	**Unit**
PBHTC	Pool boiling heat transfer coefficient	kW/m^2K
$\boldsymbol{k}$	Thermal conductivity	W/mK
$\boldsymbol{\mu}$	Dynamic viscosity	mPas
$\boldsymbol{\varphi}$	Volume fraction	%
$\boldsymbol{\rho}$	Density	kg/m^3
$\boldsymbol{u}$	Velocity	m/s

Abbreviations

BF	Base fluid
CFD	Computational fluid dynamics
CNS	Carbon nanosphere
CNP	Carbon nanopowder
CNT	Carbon nanotube
CTAB	Cetyltrimethylammonium bromide
DOM	Digital optical microscopy
EG	Ethylene glycol
EDX	Energy-dispersive X-ray analysis
FTIR	Fourier transform infrared
GA	Gum Arabic
HTC	Heat transfer coefficient
MWCNT	Multi-walled carbon nanotube
PBHT	Pool boiling heat transfer
PBHTC	Pool boiling heat transfer coefficient
PD	Pressure drop
SCMC	Sodium carboxymethylcellulose
SDBS	Sodium dodecyl benzene sulfonate
SDS	Sodium dodecyl sulfate
SEM	Scanning electron microscopy
T80	Tween 80
TG/DTA	Thermogravimetry/differential thermal analysis
TEM	Transmission electron microscopy
TX	Triton X-100
UV-Vis	Ultraviolet visible spectroscopy
XPS	X-ray photoelectron spectroscopy
XRD	X-ray diffraction
ZP	Zeta potential

Subscripts

nf	Nanofluid
bf	Base fluid

List of Figures

List of Tables

1. Introduction

Conventional heat transfer fluids such as water, propylene glycol, ethylene glycol (EG), and engine oil have been broadly utilized in many industrial applications [1]. The heat transfer enhancement of these fluids can reduce the material cost, energy, process time, and size as well as increase the lifetime of the device [2], [3], [4]. In heat exchange systems, one of the problems is that the conventional heat transfer fluids have low thermal conductivity. The thermal conductivity of these fluids can be enhanced by dispersing the solid particles in them [5]. The study of the thermal conductivity of mixtures of solid particles and liquids was first developed in the 19th century when James Clerk Maxwell dispersed small particles into liquids [6]. Further studies were conducted with millimeter, micro-sized particles, which enhanced the properties of fluids [7]. However, the major problem with these particles was that they settled rapidly in the fluids. Additionally, this caused a pressure drop (PD) and erosion of pipelines. These issues may be resolved by using nano-sized particles [8]. Nano-suspensions are a new class of nanotechnology-based heat-transfer fluids. First, aluminum oxide (Al_2O_3) ultrafine particles were dispersed into water by Masuda et al., and the thermal conductivity enhancement was 30 % [9]. Nanofluids, coined by Choi and Eastman [10] in 1995, are colloidal suspensions of ultrafine metallic or nonmetallic particles in a base matrix host fluid. Some essential requirements should be met, for example, steady-state suspension, low agglomeration of nanoparticles, and the base fluid (BF) should be chemically unchanged [11].

The use of nanoparticles improves the thermal conductivity of fluids but increases their viscosity as well, which causes an increase in pump energy [12]. This trade-off significantly limits the industrial application of nanofluids in heat transfer systems. Like thermal conductivity, the viscosity of nanofluids also depends on the size and shape of particles and clusters [12]. Therefore, the combined investigation of viscosity and thermal conductivity is essential. Numerous studies [9], [13], [14], [15] have addressed these challenges, yet there remains a critical need for highly effective nanofluid formulations. Many investigations focused primarily on nanofluid behavior without a comprehensive characterization of the nanomaterials themselves, which limits the accurate interpretation and comparison of reported results [16].

My research aims to bridge this gap by meticulously investigating the interaction between different material properties to develop nanofluids optimized for heat transfer applications. My thesis provides an in-depth analysis of the thermophysical properties of nanofluids, with a particular focus on thermal conductivity and viscosity. The research focuses on the influence of key factors: nanoparticle size, type, and concentration; nanofluid stability; the role of stabilizers; and nanoparticle synthesis methods. In addition, my research investigates the pool boiling heat transfer (PBHT) performance of the prepared stable nanofluid and conducts numerical simulations using computational fluid dynamics (CFD) under turbulent flow conditions.

2. Literature review

2.1. Types of nanofluids

Nanofluids can be divided into two types: metallic nanofluids (metals: Au, Ag, Cu, Al, Fe; metal oxides: Al_2O_3, CuO, Fe_3O_4, SiO_2, TiO_2, ZnO, etc.; carbides: TiC) and nonmetallic nanofluids (graphite, diamond, single-walled carbon nanotubes (CNTs)/multi-walled carbon nanotubes (MWCNTs), graphene, etc.) [17]. There are two primary methods to produce nanofluids: the one-step method, by creating the BF and nanoparticles together, and the two-step method, by creating the nanoparticles separately and then mixing them with the BF [18], [19]. Nanofluids have some important characteristics for different utilizations, for example, high heat conductivity, ultrafast heat transfer ability, good stability, and good lubrication. These fluids can lower the friction coefficient by facilitating a rolling mechanism between contact surfaces. Furthermore, the formation of a nanoparticle-rich protective layer on the solid boundaries helps in reducing mechanical wear [20].

In 1999, Lee et al. [21] used Al_2O_3 and CuO nanoparticles in water and EG. They found that thermal conductivity was linearly dependent on the volume fraction. In 2001, Eastman et al. [22] dispersed nanometer-sized copper particles in EG, and the effective thermal conductivity was much higher than the BF. Choi et al. [23] showed that non-metallic nanomaterials, MWCNT, in water increased the thermal conductivity up to 160 % at 1 % volume fraction. After that, much research on heat transfer fluids was performed with different nanomaterials, such as aluminum [24], [25], [26], gold [27], copper oxide [28], CNT [29], [30], silicon dioxide, and titanium dioxide [31]. While the influence of nanoparticle type on the thermal conductivity of nanofluids is clear, the effect of particle size remains controversial [32].

The nanoparticles can be prepared by various techniques or by the combination of different techniques, such as ball milling, chemical vapor deposition, and plasma treatment [33], [34], [35]. Based on nanoparticles, there are two types of nanofluids: single material and hybrid or composite nanofluids. The first type of nanofluid is traditional using a single kind of nanoparticle dispersed into the BF. In the literature, there have been many studies reporting that these nanofluids have more advantageous thermophysical properties than the BFs, such as thermal conductivity and heat transfer coefficient (HTC) [36], [37]. Compared to the standard nanofluid, hybrid nanofluids offer even more possibilities. Hybrid nanofluids are innovative and novel types containing a mixture of more than one kind of nanoparticles suspended in BF [38], [39]. In 2007 Jana et al. [40] were the first to investigate the CNTs, copper nanoparticles, gold nanoparticles, and their hybrids. They showed that the Cu/H_2O nanofluids had the highest enhancement in thermal conductivity, while the CNT-Cu/H_2O had better stability than others.

2.2. Preparation of nanofluids

The preparation of nanofluids is the first and main part of the exploratory investigation of nanofluids. It is not just a simple operation of mixing the nanoparticles into the BF. The preparation requires some characteristics such as uni-dimensionality, physical and chemical stability, and dispersibility [41], [42].

There are two types of nanofluid preparations, including the one-step method and the two-step method [43]. In the first case, the production of nanoparticles and dispersion of nanoparticles into BF are combined in one step, as shown in Figure 1. Physical vapor deposition is the most used method, in which the nanoparticles are directly evaporated and condensed in BF. In this way, they produce pure and uniform nanoparticles. As a result, the minimization of the particle agglomeration is an advantage of the one-step synthesis technique. But strict conditions are required for such a process. Additionally, the obtained nanofluids contain residual reactants, and the cost is high. Eastman et al. [44] produced Cu nanofluids by condensing Cu vapor directly with EG at low vapor pressure. Zhu et al. [45] prepared stable Cu nanofluids via chemical reactions in which $CuSO_4.5H_2O$ was reduced with $NaH_2PO_2.H_2O$ in EG under microwave irradiation.

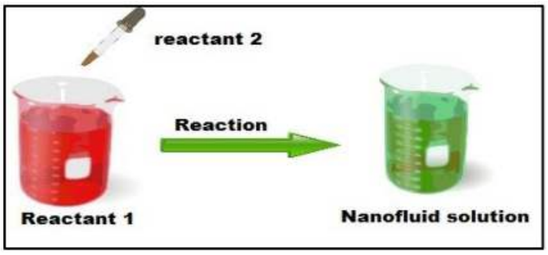

Figure 1. Single-step method [46]

In the two-step method, the nanoparticles are prepared first and then dispersed into the BFs. The volume of a nanoparticle is measured through its mass and density. The two-step preparation process [47] is very popular in research articles as the most convenient process for the production of nanofluids because of its simplicity. Stabilization and proper mixing are required to get nanofluids with homogeneously dispersed nanoparticles due to the strong van der Waals force among nanoparticles. The most common technique is shown in Figure 2.

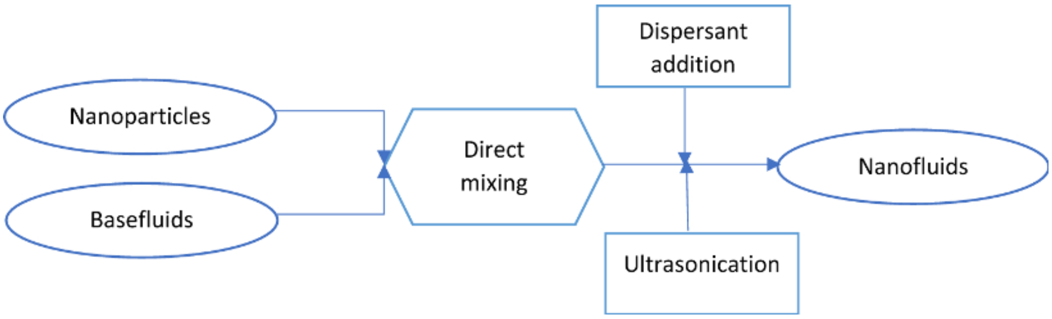

Figure 2. Two-step preparation process of nanofluids

A higher shear mixing or ultrasonic sonication is mostly used to homogenize nano-powders with BFs. In order to reduce particle agglomeration, the intensive use of ultrasonication or stirring is required. In most research articles, water is used as BF. Zhang et al. [48] used the two-step method to prepare the TiO_2/water nanofluids by adding pH stabilizing agent (tetramethylammonium hydroxide) and surface-modifying agent (3-aminopropyltriethoxysilane). Jia et al. [49] produced graphene nanofluids with water and stabilizing agent carboxyl methyl cellulose using ultrasonic vibration. Alberola et al. [50] used halloysite to prepare the halloysite/water nanofluid by sonication and improved its stability by setting pH = 12. Hashemi and Noie [51] prepared the MWCNT/water nanofluids from MWCNT nanoparticles and Gum Arabic (GA) and then sonicated them for 120 min. Yu et al. [52] exhibited a chemical method for producing graphene oxide nanosheet-based nanofluids. Graphene oxide was first exfoliated in anhydrous ethanol, after which the collected nanoparticles were dispersed in EG without additional agents. Agresti et al. [53] dispersed the silica nanoparticles of spherical shape in distilled water, and then the nanofluids were obtained by ultrasonication. Similarly, Nabil et al. [15] prepared the hybrid nanofluids from TiO_2 and SiO_2 nanoparticles and a water/EG mixture. Park et al. [54] and Ghozatloo et al. [55] produced graphene nanosheets by using chemical vapor deposition to develop the graphene nanosheets on copper foil by catalytic decomposition in a quartz tube heater system. With the reflux system and potassium persulfate, the functionalization of graphene took part, and after that, it was mixed with water. Then, it was homogenized in the ultrasonic bath for one hour to produce the graphene nanofluids. With other BFs, Agarwal et al. [56] prepared graphene–kerosene nanofluids with oleylamine as a stabilizing agent by the two-step process. Luo et al. [57] used this technique to produce graphene oxide nanofluids of oil and water, while Su et al. [58] worked with n-butanol alcohol aqueous solution.

2.3. Stability of nanofluids

Nanofluids are able to lose their potentiality to transfer heat for the reason that nanoparticles have a tendency of coagulation involving electrical double-layer action, steric action, and van der Waals forces [59]. Balancing the competing interactions supports nanoparticle dispersion and prevents clustering and aggregation. Meanwhile, agglomeration was investigated as a factor that increases the thermal conductivity of nanofluids. As a result, the investigation of a stable and homogeneous nanofluid is an unavoidable and great challenge for nanofluid preparations.

2.3.1. Stability mechanisms

The stabilization of nanofluids is the most urgent concern, as it ensures that nanoparticles remain dispersed without significant agglomeration over time. The reason for the agglomeration of the nanoparticle is that nanoparticles in nanofluid are able to attach together as a result of the attractive force against the repulsive force. Specifically, van der Waals forces promote attraction, while electrical double-layer forces provide repulsion. Also, the random Brownian motion of nanoparticles increases their chances of encountering and attaching to each other [60]. When attraction prevails over repulsion, two nanoparticles will collide, and nanoparticles tend to agglomerate in clusters. In contrast, if nanoparticles have stronger repulsion than attraction, then nanofluids will exist in a steady state. Accordingly, the enhancement of repulsive force can ensure keeping nanofluid in a steady state and prevent nanoparticle agglomeration. As specified by the repulsion kinds, the fundamental mechanisms are divided into two kinds: steric stabilization and electrostatic stabilization [61], shown in Figure 3.

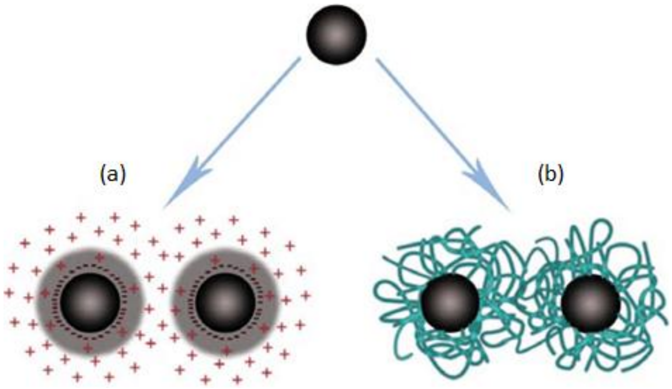

Figure 3. Electrostatically and sterically stable nanoparticles (a: electrostatic stabilization, b: steric stabilization) [62]

For steric stabilization, macromolecules (polymers, surfactants) are involved in the colloidal system. They will be grafted to the surfaces of the particles, producing an additional steric repulsive barrier to prevent the particle from coming close to each other [63], [64]. For instance, Askari et al. [65] grafted oleic acid on the surface of Fe_3O_4-decorated graphene nanoparticles by chemisorption, and the nanofluids had good stability for more than five months. Graphene nanofluids are very stable on account of the protective role of oleylamine, as it prevents the growth and agglomeration of nanoparticles by the steric effect. This effect of stabilizing agents is determined by their concentration. Agarwal et al. [56] found that for maximum stabilization of the nanofluid, a mass ratio of oleylamine to graphene of 0.6 was the optimal value, and the nanofluids were stable for up to 60 days. Pavithra et al. [66] used polyvinylpyrrolidone nonionic-dispersant to increase the stability of CuO nanofluids for more than one week. Bach et al. [67] grafted poly(methyl methacrylate) chains onto the surface of Fe_3O_4 nanoparticles. The steric repulsive force between these chains increased the stability of the nanofluids with organic solvents. The nanocomposite content only decreased slightly, even after centrifugation.

For electrostatic stabilization, the existence of surface charge or Coulomb repulsion is a major source of stabilization. Electrostatic stabilization is developed through the following mechanisms: preferential adsorption of ions, the isomorphic substitution of ions, dissociation or physical adsorption of surface-charged species, and accumulation or depletion of electrons at the surface [68], [69]. Electrostatic interactions are pH-sensitive way [70]. Therefore, electrostatic stabilization is limited to use.

2.3.2. Stability enhancement procedures

Various methods are used for obtaining stable nanofluids, including physical methods (e.g., mechanical agitation, stirring, and ultrasonic vibration) or chemical treatment (e.g., the addition of agents, pH control). Nanofluid stability is directly related to the electrokinetic properties. Consequently, pH control can increase stability due to strong repulsive forces. The pH can control the van der Waals and electrostatic forces. For instance, acid treatment can improve the dispersibility of graphene in BF and enhance the thermal conductivity of graphene nanofluids [71]. Yarmand et al. [72], [73] studied the functionalized graphene-based nanofluids from a simple acid treatment reaction procedure, and the nanofluids were stable for many days without sedimentation. Zhang et al. [74] performed a study on the effects of pH on the stability of TiO_2/water nanofluids. They found that the nanofluids were more stable when pH was far from the isoelectric point, and pH = 12 gave the optimal stability of the nanofluids. Vallejo et al. [75]

investigated the effect of various pH values of graphene nanofluids in a propylene glycol–water mixture and observed that the absolute values of zeta potential (ZP) were higher than 30 mV for samples with pH values above 6, such as at pH = 8 ZP was lower than -40 mV. With the same method, Alberola et al. [50] showed that the suitable pH value for halloysite nanofluids of water is 12. It was found that ZP reached a zero value at pH = 3.5 and -39 mV at pH = 12 because the silica was located on outer surface and its isoelectric point was 2.

Utilizing stabilizing agents in the two-phase systems is an economical and easy way to make the nanofluids in a steady state. Stabilizing agents are able to decrease the surface tension of BFs and raise particle immersion. In the case of surfactant, stabilizing agents could consist of a hydrophobic tail portion, e.g., a hydrophilic polar head group and a long-chain hydrocarbon, which could help to modify hydrophobic materials to enable dispersion in an aqueous solution. Based on the composition of the surfactants, they can be divided into four types: anionic (negatively charged groups: alkyl sulfates, phosphates, and sulfonates), cationic (positively charged groups: quaternary ammonium compounds and protonated long-chain amines), nonionic (neutral charge groups: alcohols, polyethylene oxide) and amphoteric surfactants (pH dependent charged groups). In literature, for various kinds of nanofluids, some types of stabilizing agents were utilized, such as sodium carboxymethyl celluloses (SCMC) [49], oleylamine [56], sodium dodecyl sulfate (SDS), sodium dodecyl benzene sulfonate (SDBS) [76], Tween 80 (T80), acumer terpolymer [77], sodium deoxycholate (NaDC) [78], Triton X-100 (TX) [79], GA, cetyltrimethylammonium bromide (CTAB) [76]. Nevertheless, using stabilizing agents also affects the thermophysical characteristics of the nanofluids in many ways due to the fact that stabilizing agents are cross-linked in solvents and molecules of solvent [80]. It should be noted that this technique cannot be useful for nanofluids acting at high temperatures, typically above 100 ^{o}C, as a result of damage to the bonding between the nanoparticle and stabilizing agents. Stabilizing agents may produce foams while heating. Furthermore, stabilizing agents can extend the thermal resistance of the nanofluids because the stabilizing agents attach to the nanoparticle surfaces [81]. These restrictions are able to limit the enhancement of the effective thermal conductivity.

The surface modification technique is an agent-free technique that can deliver better nanofluid stability for more than one day. A lot of researchers utilized such modification techniques. Myekhlai et al. [82] presented work on the production of graphene and silver nanoparticles composite by adding silver to the surface of graphene. It was noted that the combination of silver and graphene in the composite material considerably improved the thermal conductivity of BF, and the specific surface area was enhanced. Sen et al. [83] modified the surface of TiO_2 nanoparticles with monolayer coverage of propyl sulfonate functional groups. They found that the modified TiO_2 nanofluids were more stable with TiO_2 loadings up to 50 wt%. Similarly, Hosseini et al. [84] modified the surface of TiO_2 nanoparticles with N-(2-aminoethyl)-3-aminopropyltrimethoxysilane as a coupling agent and then dispersed in a 10 wt% salt concentration to obtain the stable nanofluids. Fahad et al. [85] used oleic acid to modify the surface of TiO_2 and Al_2O_3 nanoparticles and, from the obtained nanoparticles, prepared the hybrid nanofluids with base oil. Yarmand et al. [72], [73] increased the stability of nanofluids by introducing the hydroxyl and carboxyl function groups onto the graphene surface. With the same purpose, Mehrali et al. [86] prepared nitrogen-doped graphene by a hydrothermal process with graphene oxide as a raw material in an ammonia solution. Grinding can be utilized to significantly enhance the dispersibility property in BF water [71].

After the nanofluid preparation, agglomeration can occur over time, which causes rapid sedimentation of the particles as a result of the enhancement of downward body force. The physical techniques used to promote the stability of nanofluids are stirring, mechanical agitation, and ultrasonic vibration. Several researchers have used mechanical stirring techniques, where the working BF was water [87], [88], [89]. Many authors have studied the use of ultrasonic vibration to disperse and suspend in many BFs. For instance, Amin et al. [90] studied the importance of sonication time on the stability of nanofluids. It was found that the ultrasonication time of 60 min gave the best stability of MWCNT nanofluids.

The stability of nanofluids has been a main and challenging problem so far. This limits the utilization of nanofluids in heat transfer applications. Thus, further investigation is required to obtain optimum methods to enhance the thermal and chemical stability of graphene nanofluids on the optimum basis, surface modification techniques of nanoparticles, and the use of various stabilizing agents.

2.3.3. Stability evaluation methods for nanofluids

Stabilization of nanofluid can be estimated through measurement of the exact amount of the settled and suspended nanoparticles in BF over time. There are eight different methods to study the stabilization of nanofluids as follows: UV–Vis spectrophotometry, ZP, sedimentation photograph capturing, scanning electron microscopy (SEM) and transmission electron microscopy (TEM), sedimentation balance method, 3ω method, centrifugal dispersion analysis, and thermal conductivity.

In a nanofluid, ZP is the difference of potential between the stationary sheet of BF grafted to the nanoparticle and BF, shown in Figure 4. The electrical potential is considered as ZP that is associated with the repulsive force between neighboring, analogously charged nanoparticles in the suspension system. Therefore, nanofluids having low ZP will gradually coagulate, while nanofluids with high ZP (positive or negative) are known as electrically stabilized.

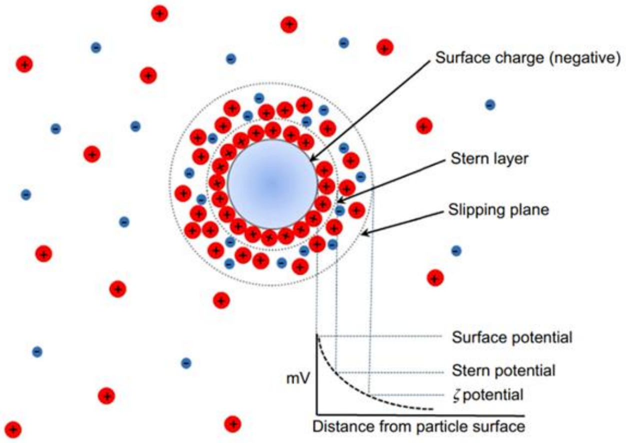

Figure 4. Definition diagram of ZP [91]

Nanofluids are believed to have good stabilization with ZP between 30 and 60 mV (see Figure 5). Nanofluids with ZP higher than 60 mV are known to have excellent stabilization [92]. Many researchers, such as those in studies [49], [93], have utilized ZP to study the stability of nanofluids, partly because it allows for quick and easy determination of the electrostatic repulsion between particles, which is crucial for preventing agglomeration. For example, Vakili et al. [94] utilized this method for graphene nanofluids, and Zainon et al. [95] also utilized it for SiO_2-TiO_2 hybrid nanofluids. With this method, Alberola et al. [50] determined the optimal pH, which was 12, for halloysite nanofluids.

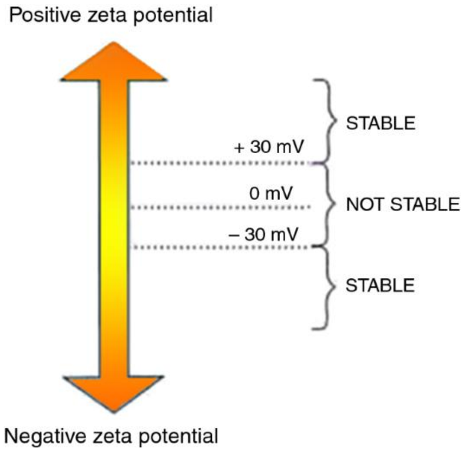

Figure 5. Scheme for ZP of stable and unstable dispersions [96]

Sedimentation method is the most elementary and simplest technique to evaluate the stability of nanofluids [97]. The sediment amount is an expression of the stabilization of the characterized nanofluids under an external force field to start the sedimentation of nanoparticles. When the concentration or particle size of the supernatant particles remains constant over time (the time frame is often day), the nanofluids are generally considered to be stable. Wang et al. [98] used the principle of this technique in their own experimental setup for measuring the stabilization of the graphene nanofluids. With the use of a camera, Wei et al. [99] took pictures of the nanofluids within 24h after preparation.

TEM is used to discover particle size distribution and particle agglomeration of nanofluid, while surface structures can be studied effectively by using SEM. The effect of surfactant and polymer addition on the dispersion of Cu-Zn-Al LDH nanofluid was studied by Chakraborty et al. [100]. They reported stability based on TEM and SEM that were highly correlated with ZP and sedimentation measurement.

Another technique known as sedimentation balance can also be used to measure the stability of the nanofluid. The balance tray is immersed in the fresh nanofluid, then the mass of sediment nanoparticles is measured over a given period. This method was used by Zhu et al. for the stability of suspensions of graphite nanoparticles [101].

The three-omega technique can be used to determine the colloidal stability of nanofluid. The thermal conductivity improvement caused by nanoparticle sedimentation over a broad nanoparticle volume fraction range can be used to evaluate it. Oh et al. [102] used this method for the stability measurement of Al_2O_3 nanofluids based on water and EG.

Spectral absorbance analysis via UV–Vis spectrophotometer is another efficient way to the evaluation of the stability of the nanofluids. Generally, there is a linear relationship between the concentration of nanoparticles in fluid and the absorbance intensity. In some cases, the sample must be diluted before measurement [103]. The advantage of this method compared to other methods is that UV–Vis spectroscopy can give a concentration of nanofluids. Many researchers analyzed the stability of nanofluids by measuring the UV–Vis absorption after different sediment intervals (see Figure 6) [76], [104], [105]. This approach involves monitoring how the absorbance changes over time as particles settle out of suspension. A decrease in absorbance over time indicates that the nanoparticles are aggregating or settling, which suggests instability in the nanofluid. Conversely, stable nanofluids show little to no change in absorbance, indicating that the nanoparticles remain well-dispersed. By comparing absorbance readings at different time intervals, researchers can determine the stability of the nanofluid and conclude whether it maintains its dispersion properties or if sedimentation occurs, which would reduce its effectiveness in applications.

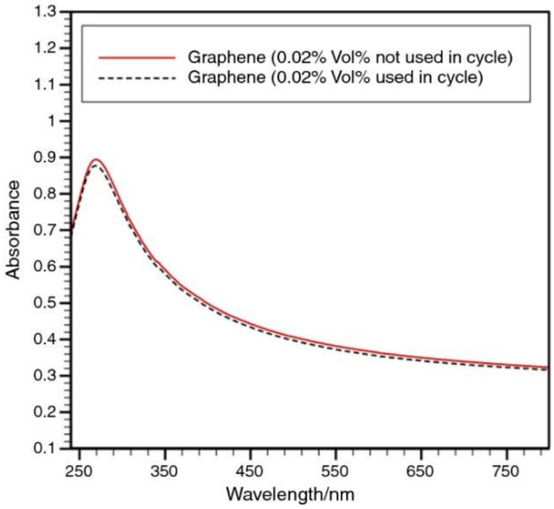

Figure 6. UV–Vis spectra of graphene nanofluids before and after using the nanofluid in the testing cycle duration of 1 week [106]

There are other methods, such as applying centrifugation, observing the amount of sedimentation after a period of time, and investigating the change in thermal conductivity of the nanofluid after a certain time.

2.4. Applications for nanofluids

Different types of nanofluids have been used for a large range of engineering applications, such as heat pipes, sensors, micro-mini-channels, clean energy devices, heat sinks, composite materials, automobiles, medicine, cosmetic, air-conditioning, refrigeration, solar energy device, lubricants, and coolants as shown in Figure 7.

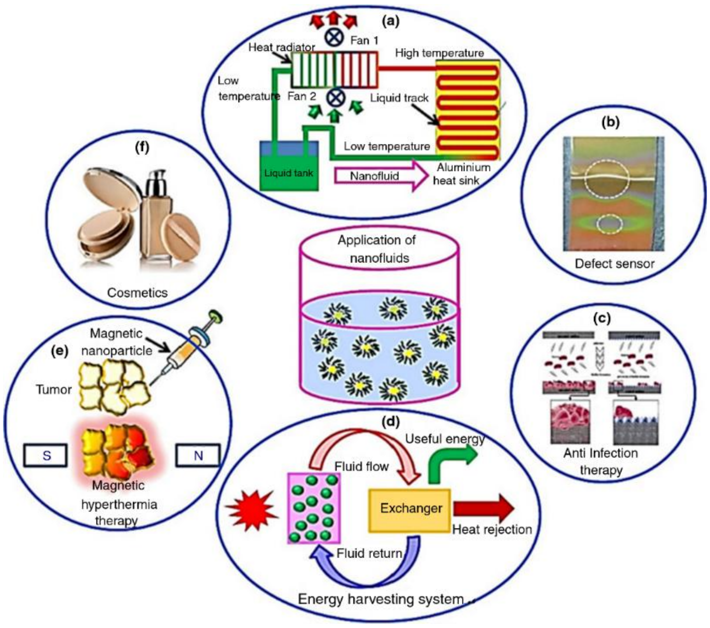

Figure 7. Application of nanofluids [107]

Due to the rapid development of modern technology, recent electronic devices with more compact dimensions generate a tremendous amount of heat. This reduces the normal efficiency of advanced electronic devices and reduces expected life and reliability. Thus, reliable thermal management is essential for the good working of electronic devices. Generally, heat removal can be improved with two approaches: finding an optimum geometry of cooling devices and increasing the heat transfer capacity. Ali and Arshad [108] used graphene nanofluids with pin–fin heat sinks. This contributed to a striking advancement in active cooling technology with graphene/water nanofluid. The integral fin heat sink with graphene nanofluid is appropriate for electronic devices that dissipate the maximum heat flux around 50 kW/m^2. Xia et al. [109] used TiO_2/water and Al_2O_3/water nanofluids to perform the comparison of the heat transfer performance of a fan-shaped micro-channel heat sink with the rectangular micro-channel one. Al_2O_3/water nanofluids gave higher heat transfer enhancement than TiO_2/water nanofluids, although TiO_2 nanofluids have better thermal conductivity.

The heat pipe, a two-phase thermal transfer device, is explored with different coolant mediums as an active and passive cooling technology. The different nanomaterials such as silver, graphene oxide, and TiO_2 in a miniature loop heat pipe, oscillating heat pipe, wick, and grooved heat pipe have been studied and have obtained remarkable improvement in thermal transfer efficiency [79], [110], [111], [112]. Additionally, it is believed that the functionalization of graphene nanoparticles may present various impacts on the heat efficiency of the heat pipe.

Heat management of automotive engines has an impact on the efficiency of vehicles both indirectly and directly as it influences motor efficiency, fuel utilization, human comfort, emissions, component life, maintenance, and vehicle quality. The effective cooling of motors utilizing nanofluids has been investigated by different researchers. Amiri et al. [113] used crumpled nitrogen-doped graphene with water–EG mixture, and Sahoo et al. [114] utilized Ag, Cu, SiC, CuO, and TiO_2 in 0-1 % volume fraction of Al_2O_3/EG nanofluids as a coolant through an automobile radiator. It was found that with higher loading of nanoparticles, a higher HTC is obtained. The authors suggested more investigations for various BF, loading, and inlet temperature across the car radiator.

The use of mini channels with nanoparticles has been reported for thermal system applications by some researchers. Ahammed et al. [115] performed an experimental study for entropy generation analysis in a multiport mini-channel heat exchanger coupled with a thermoelectric cooler. It was observed that the thermal efficiency of graphene nanofluid is better than Al_2O_3 nanofluid and hybrid nanofluid containing Al_2O_3 and graphene. Yilmaz et al. [116]

studied the effects of Al_2O_3 nanofluids on the tube side of the mini-channel shell and tube heat exchanger. They found that the HTC was higher in turbulent and transition areas.

The heat exchanger is utilized broadly in industry and particularly in processing plants, for example, power plants, cooling towers, refineries, etc. The key challenge is the powerful heating and cooling of processing liquids inside the heat exchangers. To improve the heat exchange rate, the conventional technique is to increase the surface area; however, the cost becomes the main parameter. Some studies are accessible on the effective cooling of heat exchangers with nanofluids on flow arrangement [117], flow regime [118], and construction [119]. From the studies, at a fixed Re number, the rise of loading graphene to water enhances the convective HTC. Furthermore, a higher Re number and higher concentration of nanoparticles cause an increment in friction factor, which results in increasing PD and pumping power.

Some studies have been presented on boiling heat transfer under various regimes and boiling parameters with nanofluids [120]. PBHT is still being investigated to decrease or increase the rate of heat transfer. Several researchers [121], [122] used nanoparticles with water reporting the improvement in critical heat flux and boiling HTC by modifying heater size, shape, material, diameter and orientation, the heat of channel surface condition, the degree of surface wetting, etc.

Researchers [88], [123], [124], [125] have investigated nanofluids in direct absorption solar collectors and flat plate solar collectors, focusing on the enhancement of the absorption of solar irradiation. An increase of up to 16.74 % was found by Choudhary et al. [126] using MgO nanofluids compared to EG/water. Saffariana et al. [127] used CuO/water nanofluids in flat pipe solar collectors and found that the HTC increased to 78.25 %. Due to the water disinfection of silver particles, silver nanofluids were studied by Parsa et al. [128] in a solar desalination system. It was stated that the nanofluids had a better heat transfer rate compared to the BF.

2.5. Halloysite nanofluids

In the aggregation mechanism, thermal conductivity occurs along with large particles or aggregates. This means that the size and shape of particles and clusters play an important role in thermal conductivity enhancement [129], [130], [131]. It has been observed that materials with elongated or chain-like structures, such as nanofibers or nanotubes, tend to exhibit higher thermal conductivity due to the more efficient heat transfer along their extended structures. As a result, significant research has focused on the applications of CNT nanofluids [30], [132], titanium dioxide nanotubes [133], titanate nanotubes [134], boron nitride nanotubes [135], etc.

Halloysite, belonging to the kaolin group, is a low-cost nanotubular clay with the chemical formula $Al_2Si_2O_5(OH)_4 \cdot nH_2O$, where n = 0–2 [136]. The length of the halloysite is from 0.02 to 30 µm, the inner diameter is from 10 to 100 nm, and the outer diameter is approximately 30 to 190 nm [137], [138]. The inner surface includes Al–OH groups, while the outer surface comprises inert Si–O–Si groups. Therefore, the reactivity of the outer and inner surfaces are different [139]. Because of these properties, there are many different applications of halloysite, such as solvent-free nanofluids [140], [141], nanoreactors [142], drug delivery [143], energy storage devices, etc. [144]. Although halloysite has been studied extensively for various applications, its use in preparing water-based nanofluids has been relatively underexplored. Few studies, such as that by Alberola et al. [50] have focused on this area, highlighting the need for further research. They prepared a halloysite nanofluid and improved its stability by adjusting the pH to 12. Their findings showed an 8 % enhancement in thermal conductivity at a 5 % volume concentration and a temperature of 80 °C, indicating the potential of halloysite nanofluids for thermal management applications. In contrast to Alberola's approach, which relied on pH adjustment for stabilization, my work compares pH-based stabilization with the use of a stabilizing agent. The aim is to evaluate the stability and performance of halloysite nanofluids under both conditions, while assessing the potential of stabilizing agent to reduce the need for extreme pH environments.

2.6. Halloysite nanofluids in PBHT

With the quick increase in the global population and the development of industries, the demand for resources has grown significantly [145]. Energy is recognized as one of the most important issue people are facing now and in the future. Therefore, more efficacious and beneficial energy usage and administration are needed [146]. Another reason comes from the ever-increasing rates of heat emission at both macro- (e.g., car engines) and micro-level (e.g., chips in computers and mobile phones). At the present time, cooling by using two-phase pool boiling processes is an essential matter in the industrial sector due to the urgent need for miniaturization of electronics on the one hand and increasing the performance improvement of such heat exchange systems on the other hand [147]. The latent heat of vaporization during this process could play an important role in removing large amounts of heat from high heat flux devices. Heat transfer requires an appropriate cooling system for effective heat dissipation with a competent working fluid. The conventional heat transfer fluids currently used, like EG, water, air, and oil, have very low thermophysical properties and low thermal conductivity compared to solids. The investigation of new fluids with higher energy efficiency for heat transfer is necessary to solve the heat transfer challenges in heat exchange systems. Moreover, all methods for the improvement of heat transfer, such as turbulence generation and area expansion, are limited by the low thermal conductivity of the fluids. Consequently, it makes sense that the improvement of the thermal conductivity behavior of fluids will be studied.

The PBHT process is an important method in heat exchange systems and the industry in general. Based on the up-to-date research and published works, the PBHT process in the nucleate boiling regime is a complicated phenomenon. PBHT from tubes has been under consideration by heat transfer professionals as it is used in many industrial fields such as reactor cooling, evaporators, boiler tubes, etc., [148]. The use of nanofluids in PBHT has shown conflicting results in previous studies regarding pool boiling heat transfer coefficient (PBHTC). It has been widely reported in the literature that PBHT performance is affected by numerous parameters and conditions, i.e., BF, nanoparticle type, nanoparticle shape and size, volume concentration, thermo-physical properties of BF, nanomaterial morphology, nanofluid stability, heating surface characteristics, and many more.

In 1986, experimental research with Al_2O_3 nanofluids (0.1–0.5 wt%) was first performed by Yang et al. [149] to study the behavior of PBHT. It was presented that the PBHT of nanofluids was improved in comparison to the BF. Das et al. [150] did an experimental study using the alumina nanoparticles to see their performance and effect on the HTC and pool boiling curve with the aid of using a narrow heated pipe. The result revealed that the system for boiling bubbles differed from small to standard industrial tubes because the bubbles were sliding from the ground part to the upper region. Research on PBHT of MWCNT nanofluids was conducted by Sarafraz et al. [151] for modified heating surfaces. In their study, by investigating some properties of diamond-shaped micro-finned surfaces, the results stated that the PBHTC decreased on smooth surfaces, and with modified surfaces, it was enhanced to 77 % for 0.3 wt%. Nevertheless, a continual layer was formed, and it caused a considerable decrease in HTC.

The PBHTC of ZnO nanofluid with the BF of EG and water in a cylindrical vessel under barometric pressure was studied by He et al. [152]. It was found that the increase in heat flux significantly increased the HTC of the nanofluid. Xing et al. investigated the effects of surface modification with covalent and non-covalent functionalization groups on the PBHT of MWCNT nanofluids (0.1–1 wt%). It was seen that the PBHTC enhancements were 34.2 % and 53.4 % for carboxyl and hydroxyl-modified MWCNT nanofluids, respectively. This happened because the surface modification reduced the deposition of MWCNT. The impact of depositing Ag nanomaterials in reentrant inclined mini-channels for PBHT was investigated experimentally by Akbari et al. [153]. It was found that with the rising concentration of the nanofluids to get a nanocoated polished surface, the PBHTC was higher. Moreover, the PBHT was improved by inclination and reentrancy compared with polished copper. The PBHTC of water and Al_2O_3-based nanofluids with low concentrations (0.0007 and 0.007 %) were studied by Manetti et al. [154]. The results showed an enhancement of HTC up to 15 % for rough surfaces and 75 % for smooth surfaces compared to water.

The PBHT performance of Fe_3O_4/water nanofluid was investigated by Salimpour et al. [155] under atmospheric pressure on a flat copper surface in order to investigate the impacts of concentration and type of the nanofluids, sedimentation thickness, roughness of the surface, and heat flux on the surface roughness after boiling experiments. It was seen that after the boiling test on the rough surface, the nanofluids' PBHT decreased at low heat fluxes and increased at high heat fluxes, while on the smooth surface, the PBHT increased at low heat fluxes and did not change at high heat fluxes. The influence of surface roughness and nanoparticle deposition on surface wettability, contact angle, and PBHTC was determined. The higher concentration of Fe_2O_3 nanofluids increases the surface roughness. They acquired the greatest HTC for the smooth surface with the deposition of nanoparticles at low-weight concentrations.

The PBHT of two kinds of distilled water-based nanofluids (CuO nanofluids and TiO_2 nanofluids) on a flat heater plate was studied by Karimzadehkhouei et al. [156]. It was shown that the TiO_2 nanofluids had the greatest improvement (around 15 %) at the lowest concentration (0.001 wt%), while the enhancement of the CuO nanofluids was 35 % for 0.2 wt% concentration. ZnO-EG nanofluids were used by Kole and Dey [157] for the experimental investigation of PBHT performance. The PBHT performance of ZnO nanofluids was studied for different concentrations at atmospheric pressure. The PBHTC of the nanofluid at 1.6 % was enhanced to 22 % in comparison to that value of the BF. Kamel et al. [158] investigated the improvement of PBHTC using Al_2O_3 and CeO_2/water hybrid nanofluids at atmospheric condition. Their heater geometry was a horizontal typical copper tube which was fixed inside a pool of working fluids that were tested for this purpose. They found that the PBHTC of the hybrid nanofluids was improved by about 1.37 times higher than that of water. However, they concluded that using hybrid nanofluids with the range of dilute concentrations utilized in this study could improve the heat transfer compared with mono fluids (alumina nanofluid or ceria nanofluid) with the initial surface roughness used in their study. In literature, there have been no studies on halloysite nanofluids in PBHT application. This identifies a significant knowledge gap that my research aims to address.

2.7. Hybrid nanofluids

Nabil et al. [159] and Ganvir et al. [160] presented some reviews about the thermo-physical properties of hybrid nanofluids. Hybrid nanofluids with CNTs grafted to alumina/iron oxide spheres dispersed in poly-alpha-olefin were studied by Han et al. [161]. A thermal conductivity enhancement of 21 % for a volume concentration of 0.2 % was obtained. The CNTs played an important role in the augmentation of thermal conductivity. The Al_2O_3–Cu/water hybrid nanofluids with volume concentrations from 0.1 to 2 % were investigated by Suresh et al. [162]. A maximum thermal conductivity enhancement of 12.11 % compared to a single Al_2O_3 was shown at a volume concentration of 2 %. Madhesd et al. [163] investigated Cu-TiO_2 hybrid nanofluids in the application of water-based coolant. The thermal conductivity of the fluid increased by 48.4 % compared to the BF of water up to 0.7 % of the hybrid nanocomposite. It was found that the functionalized surface and the high crystallinity of the nanocomposite improved the enhancement of thermal conductivity. In recent years, further investigations on the viscosity of hybrid nanofluids have been performed [164], [165], [166]. A numerical study on a hybrid nanocomposite of TiO_2, Al_2O_3, and SiO_2 nanoparticles dispersed in water was performed [167]. Al_2O_3 (25 %) was mixed with TiO_2 (75 %) or SiO_2 (75 %) to prepare hybrid nanofluids at concentrations of 0.5, 1.0, and 1.5 %. An experimental investigation on the rheological behavior of Fe–CuO hybrid nanofluids was performed in water–EG at a proportion of 20:80. The concentration range of hybrid nanofluids was 0.04–1.5 %. They found that at low concentrations, the rheology of hybrid nanofluids was Newtonian, whereas, at high concentrations, hybrid nanofluids exhibited non-Newtonian behavior (shear-thinning) [168]. The heat transfer of non-Newtonian nanofluid has different behaviors, for example, in the presence of suction and injection [169]. Sundar et al. and Zakaria et al. [170], [171] investigated the thermal conductivity of nanofluids with the BF of DW and EG mixture. They found that the enhancement of thermal conductivity was affected by volume concentration and temperature. Additionally, the particle size and stability of nanofluids contributed to the improvement of thermal conductivity [172], [173]. It was found that the combination of nanofluids had higher thermal conductivity and lower dynamic viscosity [174]. Some works have been performed to evaluate the thermal conductivity of SiO_2–TiO_2 hybrid nanofluids. Nabil et al. used TiO_2 (50 nm) and SiO_2 (22 nm) nanoparticles for investigating the heat transfer enhancement of hybrid nanofluids with different volume concentrations (0.5–3 %), temperatures (30–80 °C), BF ratios, nanoparticle ratios, and forced convection mode [13], [174], [175]. They found that the thermal conductivity enhancement of hybrid nanofluids was 22.1 % at 3.0 % volume concentration and

70 °C compared to the BF. Meanwhile, a 62.5 % increment of relative viscosity was observed for 3.0 % volume concentration.

2.8. Carbon nanofluids

Carbon-based nanomaterials have emerged as cutting-edge materials, offering a unique combination of lightweight properties, superior strength, and diverse functionality across numerous fields [176]. Among them, carbon nanospheres (CNS) have garnered significant attention due to their unique spherical structures including high surface area, porous structure and hydrodynamic properties [177]. These properties make them highly suitable for a wide range of applications, such as lubricants, catalyst supports [178], photoluminescence [179], multiphoton bioimaging [180], anode materials in batteries, nanofluids [178], etc.

Generally, carbon spheres can be prepared with three methods. First, carbon spheres may be produced directly via pyrolysis [181], [182], chemical vapor deposition [183], and hydrothermal treatment [184]. The second method uses rigid templates such as 3D macro-porous silica [185] and zeolite Beta beads [186]. Finally, carbon spheres can be obtained from the synthesized polymer spheres with thermal treatment [187]. Each method has distinct advantages in controlling the properties of the final material, with hydrothermal synthesis generally preferred due to its cost-effectiveness and high efficiency [188].

In literature, no study has been performed on the comparison of thermal conductivity and viscosity of the nanofluids containing CNS from the hydrothermal method and carbon nanopowder (CNP) from a manufacturer with different sizes. This represents another critical knowledge gap that this research intends to address by comparing these two types of carbon nanomaterials.

2.9. CFD study of nanofluids on heat transfer

The definition of CFD is “the analysis of systems involving fluid flow, heat transfer, and associated phenomena such as chemical reactions by a means of computer-based simulation” [189]. CFD is a technique generating discretized forms of partial differential equations for fluid flow issues to solve the governing equations of liquid movement [189]. CFD helps us to save resources and time in engineering plans and is very suitable for issues where areas are inaccessible to measurement instruments, such as coolant flow in twist drill machining.

The heat transfer research was conducted in at least two directions. The first was to perform experiments and then find and construct empirical and semi-empirical formulae (correlations) for solving engineering problems. The second was to analyze the heat transfer phenomenon, investigating its physics, discovering the effects of working fluid properties, the wall–fluid interaction, and the validity of the known equations applied to describe the process. The results that yield the solutions for heat transfer problems are based on a combination of experimental data and theoretical analysis. Earlier, physical experiments were the only way to determine heat transfer subprocesses. Recently, sophisticated CFD software has offered reasonable alternatives, the so-called numerical experiments, for investigating heat transfer problems related to determining the velocity and temperature fields in different arrangements. Independent of the type of experiment, the dimensionless numbers or groups resulting from the similarity theories (Buckingham pi theorem or differential similarity) prove crucial in heat transfer calculations. Boussinesq assumptions [190] are generally applied in solving the governing equations of the heat transfer (mass, energy, momentum conservation). The material properties variations are indirectly set up, usually by the proportion of the Prandtl numbers (Pr) at two characteristic temperatures (average fluid and wall). Neither the differential similarity nor the pi theorem applies if the variation in properties is included in the fundamental equations.

The most investigated and basic arrangement is the horizontal tube with an isothermal wall or steady wall heat flux. One can also use these configurations in engineering formulae for heat transfer calculation. It should be mentioned that the isothermal wall temperature, in most cases, can be maintained only in strict experimental conditions, and in practice, this assumption rarely exists. Nevertheless, the difference between the two basic approaches is nearly negligible for the Nusselt (Nu) number in a turbulent flow. Promoting the numerical experiments (making CFD calculation), the boundary conditions can easily be established, and the results of the calculations are according to the desired conditions. That is one possible explanation for the observed variance compared with the real experimental results.

Hussein et al. investigated the impact of the cross area on heat transfer and friction [191]. They found that, compared with circular and elliptical pipes, flat pipes had a notable increment of heat transfer and PD. Additionally, they studied the augmentation of forced convection heat transfer in an automotive cooling system [192].

Suresh et al. [26] presented a laminar convective heat transfer under full development (FD) and PD through a heated flat pipe using Cu-Al_2O_3 hybrid nanofluids. They observed that the enhancement of the HTC under laminar flow was 13.56 % at Re = 1730, compared with water. Mosayebidorcheh et al. [193] studied the heat transfer under a magnetic field and turbulent flow. The heat transfer was proportional to the concentration and Re number but inverse to the Hartmann number (its definition is the ratio of electromagnetic force to the viscous force) and turbulent parameter. Abbasi et al. [194] investigated the effect of the functionalization technique on thermal conductivity and the stability of CNT/Al_2O_3 hybrid nanofluids. The functional groups significantly affected the thermal conductivity of hybrid nanofluids. The thermal conductivity enhancement was 20.68 % for 0.1 % volume concentration.

Labib et al. [195] chose the two-phase mixture model to research the convective heat transfer of hybrid nanofluids. Two kinds of BFs and Al_2O_3 nanoparticles were used to determine the impact of BF on heat transfer. The computational model was validated using CNTs with water nanofluids and compared with the data presented in literature. It was found that EG had better heat transfer increments than water.

Sundar et al. [196] studied the heat transfer of Fe_3O_4-MWCNT/water hybrid nanofluids under turbulent flow in a circular tube. Their experiment presented a heat transfer increment of 31.10 % with a cost of 1.18 times increase in pumping energy at 0.3 % volume concentration and $Re = 22000$ in comparison with water. The proposed correlations fitted the experimental results. Using ultrasonication, Baby and Ramaprabhu [33] prepared Fe_3O_4/MWCNT and $Fe_3O_4@SiO_2$/MWCNT nanofluids, which had thermal conductivity enhancements of 20 % and 24.5 %, respectively.

2.9.1. Forced flow in circular tubes

Forced flow occurs in multiple configurations, and one of the important engineering arrangements is the forced flow in the duct. The duct's cross-section may appear in various shapes, and in the engineering calculation, it is maintained through an equivalent circular diameter. Therefore, investigations generally deal with only circular tubes.

Although the experiments in my work were carried out on a circular duct, it is advisable to recall that, in practice, the non-circular ducts cases can be handled well using the hydraulic (D_{eqH}) and thermal (D_{eqT}) equivalent diameter even in complex permanent cross-sectional structures. The definitions are as follows:

$$D_{eqH} = 4\frac{Area\ of\ duct}{Wetted\ perimeter}, \tag{1}$$

$$D_{eqT} = 4\frac{Area\ of\ duct}{Working\ perimeter\ in\ heat\ transfer}, \tag{2}$$

The hydraulic equivalent diameter should be used in Re number and the thermal in the Nusselt number [197].

According to the Re number, the flows in a tube are characterized as laminar flow ($Re < 2300$), transitional flow ($2300 < Re < 4000$), and turbulent flow ($4000 < Re$). However, transitional flow is often considered part of turbulent flow in engineering practice. Moreover, depending on the distance from the entrance, there are different flow formations, such as developing and (fully) developed flow regimes, as shown in Figure 8. Therefore, the local heat transfer varies alongside the tube length, and some correlation formulae count this phenomenon. As both the velocity and the temperature vary from those of the entrance, there are hydraulically developing, thermally developing, and simultaneously developing flows.

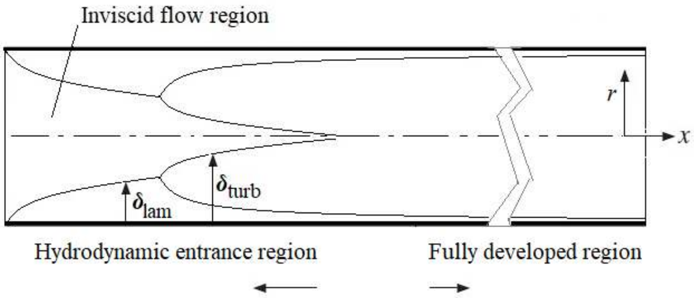

Figure 8. Hydraulically developing turbulent flow in the tube.

2.9.2. Turbulent flow

The inner perturbation of fluid causes a turbulent flow. Different perturbations always exist in the fluid. When velocity is low, the viscous forces stabilize the flow pattern, but this stabilization is not effective when the velocity increases and the local vortex formations result in a turbulent flow pattern. The laminar-turbulent transition never means a sharp borderline. There is always a particular transition zone. This phenomenon explains why the HTC (Nu number) calculations perform less when the Re number is not much larger than the laminar Re number limit. There is always a particular length after the fully developed flow pattern is generated.

In the Handbook of Heat Transfer [198], there are 12 formulae for calculating the Nu number in the smooth tube for turbulent flow. The wide variation of the starting range for the Re numbers shows that generating a formula that accounts for the transition and the fully developed regime is not a simple task. The formulae can be characterized in two groups-either (a) the ξ friction factor is not included in the formulae or (b) it is, as shown in Table 1 and Table 2. Analyzing all the formulae is beyond the scope of this study; therefore, I selected only three formulae to validate my numerical experiments, for which the application range should fit $5000 \leq Re$ and $3 \leq Pr$ for my experiments. The Dittus–Boelter (1) is generally used, while Sieder–Tate (6) accounts for the property variation, and Gnielinski (13) is based on the friction factor and also counts the tube length diameter ratio. The arrangements of the experiments should follow the limitations stated in the application ranges of the correlations considering flow development (hydraulic, thermal, and simultaneous). The other listed correlations might be useful for readers in further investigation or application of Nu number calculations.

Table 1. Correlations for Nu number based only on Re and Pr numbers [198].

Correlations (a)	**Application Range**
Dittus–Boelter (1) [199] $Nu = \begin{cases} 0.023\,Re^{0.8}Pr^{0.4}\ for\ heating \\ 0.026\,Re^{0.8}Pr^{0.3}\ for\ cooling \end{cases}$	$0.7 \leq Pr \leq 120$ $2500 \leq Re \leq 1.24 \cdot 10^5$ $L/d > 60$
Colburn (2) [200] $Nu = 0.023\,Re^{0.8}Pr^{1/3}$	$0.5 \leq Pr \leq 3$ $10^4 \leq Re \leq 10^5$
Drexel–McAdams (3) [201] $Nu = 0.021\,Re^{0.8}Pr^{0.4}$	$Pr \leq 0.7$ $10^4 \leq Re \leq 5 \cdot 10^5$
Gnielinski (4, 5) [202] $Nu = 0.0214\,(Re^{0.8} - 100)Pr^{0.4}$ $Nu = 0.012\,(Re^{0.87} - 280)Pr^{0.4}$	$0.5 \leq Pr \leq 1.5$ $10^4 \leq Re \leq 5 \cdot 10^6$ $1.5 \leq Pr \leq 500$ $3 \cdot 10^3 \leq Re \leq 10^6$
Sieder–Tate (6) [203] $Nu = 0.027\,Re^{4/5}Pr^{1/3}\left(\frac{\mu}{\mu_w}\right)^{0.14}$	$0.7 \leq Pr \leq 16$ $700 \leq Re \leq 10^4$
Hausen (7) [204] $Nu = 0.037\,(Re^{0.75} - 180)Pr^{0.42}\left[1 + \left(\frac{x}{D}\right)^{-\frac{2}{3}}\right]$	$0.7 \leq Pr \leq 3$ $10^4 \leq Re \leq 10^5$

Table 2. Correlations for Nu number containing the friction factor [198]

Correlations (b)	**Application Range**
von Kármán (8) [205] $Nu = \frac{(\xi/8)RePr}{1 + 5\sqrt{\xi/8}\left[\mathrm{Pr} - 1 + ln\left(\frac{5Pr + 1}{6}\right)\right]}$	$0.7 \leq Pr \leq 10$ $10^4 \leq Re \leq 5 \cdot 10^6$
Prandtl (9) [206] $Nu = \frac{(\xi/8)RePr}{1 + 8.7\sqrt{\xi/8}\,(Pr - 1)}$	$0.5 \leq Pr \leq 5$ $10^4 \leq Re \leq 5 \cdot 10^6$
Friend–Metzner (10) [207] $Nu = \frac{(\xi/8)RePr}{1.2 + 11.87\sqrt{\xi/8}\,(Pr - 1)Pr^{-1/3}}$	$50 \leq Pr \leq 600$ $5 \cdot 10^4 \leq Re \leq 5 \cdot 10^6$
Pethukov–Kirillov–Popov (11) [208] $Nu = \frac{(\xi/8)RePr}{C + 12.7\sqrt{\xi/8}\,(Pr^{2/3} - 1)}$ $C = 1.07 + \frac{900}{Re} - \frac{0.63}{1 + 10Pr}$	$0.5 \leq Pr \leq 10^6$ $4000 \leq Re \leq 5 \cdot 10^6$
Webb (12) [209] $Nu = \frac{(\xi/8)RePr}{1.07 + 9\sqrt{\xi/8}\,(Pr - 1)Pr^{1/4}}$	$0.5 \leq Pr \leq 100$ $10^4 \leq Re \leq 5 \cdot 10^6$
Gnielinski (13) [202] $Nu = \frac{(\xi/8)(Re - 1000)Pr}{1 + 12.7\sqrt{\xi/8}\,(Pr^{2/3} - 1)}\left[1 + \left(\frac{D}{L}\right)^{2/3}\right]\phi_T$	$0.5 \leq Pr \leq 2000$ $2300 \leq Re \leq 5 \cdot 10^6$ $\xi = (1.82log_{10}Re - 1.64)^{-2}$

Correlations (b)	Application Range
	$\phi_T = \left(\frac{Pr\ (Tmean)}{Pr\ (Twall)}\right)^{0.14}$ In the case of constant fluid properties: D/L=0, and Φ_T= 1.
Sandall et al. (14) [210] $\frac{(\xi/8)RePr}{12.48Pr^{2/3} - 7.853Pr^{\frac{1}{3}} + 3.613\ln(Pr) + 5.8 + C}$ $C = 2.78ln\left(\frac{Re\sqrt{\xi/8}}{45}\right)$	$0.5 \leq Pr \leq 2000$ $10^4 \leq Re \leq 5\cdot10^6$

According to the second law of thermodynamics, any methods or efforts made to intensify the heat transfer result in an entropy generation, which manifests in the increased amount of work that must be performed to maintain flow configuration. The calculation of that increased work – practically the pumping work – is based on the determination of the friction factor of the flow arrangement, smoothness of the tube, and viscosity of the working fluid. When the working fluid property changes and increases the heat transfer, this phenomenon – namely, the increased friction, always appears. The increased viscosity is the cost for the increased heat transfer, as the second law of thermodynamics states. The friction factor calculation might also be carried out according to several formulae. As the Prandtl–Kármán–Nikuradse friction factor definition is implicit, several value calculations are recommended and listed in Table 3 to overcome that difficulty.

Table 3. Correlations for friction factor. [198]

Correlations	Application Range
Blasius [211] (1) $\xi/4 = 0.0791Re^{-0.25}$	$4 \times 10^3 \leq Re \leq 10^5$
Drew et al. [212] (2) $\xi/4 = 0.00128 + 0.1143Re^{-0.311}$ (3) $\xi/4 = 0.0014 + 0.125Re^{-0.32}$	$4 \times 10^3 \leq Re \leq 5\cdot10^6$ $4 \times 10^3 \leq Re \leq 10^7$
Bhatti and Shah [213] (4) $\xi/4 = 0.00128 + 0.1143Re^{-0.311}$	$4 \times 10^3 \leq Re \leq 10^7$
Prandtl–Kármán–Nikuradse [214] (5) $\frac{2}{\sqrt{\xi}} = 1.7272\ln\left(\frac{Re\sqrt{\xi}}{2}\right) - 0.3946$	$4 \times 10^3 \leq Re \leq 10^7$
Colebrook [215] (6) $\frac{2}{\sqrt{\xi}} = 1.5635\ln(\frac{Re}{7})$	$4 \times 10^3 \leq Re \leq 10^7$
Filonenko [216] (7) $\frac{2}{\sqrt{\xi}} = 1.58\ln Re - 3.28$	$10^4 \leq Re \leq 10^7$
Techo et al. [217] (8) $\frac{2}{\sqrt{\xi}} = 1.7372\ln\ (\frac{Re}{1.964\ln Re - 3.8215})$	$10^4 \leq Re \leq 10^7$

2.9.3. Foundational concepts in CFD simulations

CFD simulations involve a three-step workflow:

- **Pre-Processing**: This stage focuses on defining the problem for the CFD code. It involves geometry definition and mesh generation. In the first one, a digital representation of the physical domain where the fluid flow will be analyzed. In the latter one, the computational domain is then discretized into a mesh of small elements, such as cells, triangles, or tetrahedrons. This mesh is essential for the numerical calculations.
- **Solving**: In this phase, the governing fluid flow equations are solved numerically. This involves discretizing the equations, which essentially breaks them down into smaller, more manageable pieces. A series of iterations is then performed to solve the discretized equations. This process also requires defining the properties of the fluid and selecting an appropriate flow model. Convergence is achieved when the change in solution variables between iterations becomes minimal. It's important to note that the accuracy of the final solution depends on several factors, including the initial problem setup, the resolution of the computational grid, and the accuracy of the chosen physical model.
- **Post-Processing**: This phase focuses on analyzing the data generated by the solver. It involves extracting key insights from the data and potentially refining the model based on these findings. Post-processing tools offer a variety of techniques for data exploration, including vector plots, 2D/3D surface plots, contour plots, interactive view manipulation, particle tracking, and color-coded postscript output. These visualizations are used for understanding patterns in pressure, velocity, kinetic energy, and other flow properties. A crucial aspect of post-processing is the ability to effectively visualize complex flows. Additionally, modern tools might incorporate animation for a dynamic presentation of results. Beyond graphical representations, most codes also provide reliable numerical output and data export capabilities, allowing for further analysis outside the original software.

ANSYS Workbench 16 (ANSYS Inc., Canonsburg, PA, USA) is an integrated platform that allows users to perform a wide range of engineering simulations. It provides tools for creating 3D geometry, meshing, and applying various types of finite element analysis. ANSYS Workbench integrates with other ANSYS simulation tools to provide a comprehensive simulation environment. Then, ANSYS Fluent is a part of the ANSYS suite that specializes in CFD. It is used to solve the governing equations for fluid flow, heat transfer, and related phenomena. These governing equations indicate the mathematical models of the conservation laws of physics, which are a balance of mass, momentum, and energy. The following equations were used for calculating the mass, energy, and momentum conservation with variable properties [218]:

$$\frac{\partial(\overline{u}_i)}{\partial x_i} = 0, \tag{3}$$

$$\left(\frac{\partial \rho \overline{u}_i}{\partial x_j} + \overline{u}_j \frac{\partial \rho \overline{u}_i}{\partial x_j}\right) = -\frac{\partial \overline{P}}{\partial x_i} + \frac{\partial}{\partial x_j}\left(\mu \frac{\partial \overline{u}_i}{\partial x_j} + \rho u_i' \overline{u'}_j\right), \tag{4}$$

$$\frac{\partial(\mathrm{c_p} \rho \overline{T})}{\partial \mathrm{x_i}} + \frac{\partial(\mathrm{c_p} \rho \overline{\mathrm{u}}_i \overline{T})}{\partial \mathrm{x_i}} = \frac{\partial}{\partial x_i}\left(k \frac{\partial(\overline{T})}{\partial x_i}\right), \tag{5}$$

where u is velocity component, u' is velocity disturbance, while ρ, P, T, c_p are density, pressure, temperature, and specific heat, respectively.

2.10. Knowledge gap

Based on the literature review, several significant knowledge gaps have been identified that limit the widespread application and optimization of nanofluids in heat transfer systems.

First, despite the growing interest in HNT-based nanofluids, existing studies primarily rely on extreme pH adjustment (e.g., pH = 12) to achieve dispersion stability. However, such methods may limit practical applicability due to corrosion risks and system incompatibility. Moreover, there is a lack of systematic investigation into alternative stabilizing agent, such as SCMC, particularly in terms of their comparative effectiveness on thermal conductivity over varying temperatures and volume fractions. Therefore, the development and evaluation of non-pH-based stabilization methods for HNT nanofluids remain insufficiently explored.

Second, while nanofluids have been widely studied for convective heat transfer, their application in PBHT systems remains limited, especially for HNT-based nanofluids. Existing literature lacks detailed analysis of how HNT nanofluids influence as superheat reduction and enhancement of the HTC. In particular, the performance of HNT nanofluids under PBHT conditions and their potential for heat transfer enhancement have not been comprehensively quantified.

Third, although individual SiO_2 and TiO_2 nanofluids have been studied, there is a significant knowledge gap regarding the synergistic enhancement of thermal conductivity in SiO_2-P25 TiO_2 hybrid nanofluids synthesized without stabilizing agents in mixed BFs (e.g., water-EG 5:1). A direct comparative analysis of the thermal conductivity and viscosity performance of such hybrid nanofluids against their single nanofluids across varying volume fractions and temperatures is needed to fully understand their unique advantages.

Fourth, current CFD models for nanofluids often rely on simplified assumptions and fail to accurately capture the complex behavior of hybrid nanofluids under turbulent flow conditions. In particular, there is limited validation of whether constant thermophysical property models can reliably approximate temperature-dependent models within specific Reynolds number ranges for SiO_2-P25 TiO_2 hybrid nanofluids. This creates uncertainty in selecting appropriate modelling approaches for engineering applications, highlighting the need for validated, computationally efficient CFD frameworks for hybrid nanofluids.

Fifth, carbon-based nanomaterials have demonstrated potential for thermal conductivity enhancement; however, comparative studies between different carbon nanoparticle morphologies and sizes remain scarce. Specifically, there is a lack of direct comparison between hydrothermally synthesized CNS (500 nm) and commercially available CNP (60 nm) within nanofluids. The influence of particle size, morphology, BF (e.g., ethanol vs. EG), and surfactants (e.g., T80) on both thermal conductivity and viscosity has not been systematically investigated, limiting the understanding of their relative performance in heat transfer applications.

3. Experimental section

3.1. Aim of the experiments

The halloysite nanotube/water nanofluids were prepared with SCMC stabilizing agent in comparison to pH = 12. I studied the viscosity and the thermal conductivity of nanofluids for several volume fractions (0.5, 1.0, and 1.5 %) and a temperature range of 20-60 °C. Then, I investigated the halloysite nanotube/water nanofluids with pH = 12 in PBHT.

I prepared the SiO_2, TiO_2, and SiO_2-TiO_2 nanofluids with a mixture of water and EG as BF by a two-step method using no agents. Then, I studied the viscosity and the thermal conductivity of nanofluids for several volume fractions (0.5, 1.0, and 1.5 %) and a temperature range of 20-60 °C. Then, I investigated the heat transfer performance of SiO_2-TiO_2 nanofluids with a mixture of water and EG as BF passing through a circular tube by CFD with a constant heat flux of 7955 W/m^2 and constant wall temperature of 67 °C.

I prepared the nanofluids from CNS/ethanol and CNP/EG with T80 stabilizing agent. I compared the viscosity and the thermal conductivity of nanofluids between two types for several volume fractions (0.5, 1.0, and 1.5 %) and a temperature range of 20-60 °C.

3.2. Preparation and stabilization of nanofluids

3.2.1. SiO_2-TiO_2 nanofluids

Silicon dioxide (SiO_2) nano-powder (99.5 %, 10–20 nm, 637238-50G), TiO_2 nano-powder (≥ 99.5 %, 21 nm, 718467-100G), and EG (≥ 99 %, 102466-1L) were purchased from Sigma-Aldrich, Hungary. The materials were analytical reagent grades and utilized as original, without modification. Deionized water and EG were used as BFs. Water was produced at the Department of Inorganic and Analytical Chemistry, Budapest University of Technology and Economics (Hungary). Table 4 and Table 5 show the properties of TiO_2, SiO_2 nanoparticles, EG, and water from the manufacturer.

Table 4. Properties of TiO_2 and SiO_2 nanoparticles

Properties	**SiO_2**	**TiO_2**
Color	White	White
Molecular mass/g mol^{-1}	60.08	79.87
Average particle diameter/nm	10–20	21
Density/kg m^{-3}	2220	4260
Melting point/°C	2230	1850

Table 5. Properties of EG and water

Properties	**EG**	**Water**
Formula	$C_2H_6O_2$	H_2O
Molecular mass/g mol^{-1}	62.07	18.02
Freezing point/K	260	273
Boiling point, at 101.3 kPa/°C	198	100
Viscosity at 20 °C/mPas	20.9	1
Density/kg m^{-3}	1113	997
Thermal conductivity/ W/(mK)	0.258	0.609
Specific heat at 20 °C/J kg^{-1} K^{-1}	2347	4186

SiO_2, TiO_2 nanofluids, and SiO_2–TiO_2 hybrid nanofluids were prepared by dispersing different amounts of SiO_2, TiO_2 nanoparticles, and SiO_2–TiO_2 mixture (1:1 volume ratio) in water and EG mixture (5:1 volume ratio). SiO_2–TiO_2 in amounts of 0.5, 1.0, and 1.5 % was dispersed in an appropriate mass of water and EG. Then, SiO_2–TiO_2 colloidal solutions were sonicated at 130 W and 45 kHz using an ultrasonication instrument for 1 h. Table 6 shows pure SiO_2, TiO_2 nanofluid, and SiO_2–TiO_2 hybrid nanofluid sample specifications.

Table 6. Specification of SiO_2, TiO_2 nanofluids and SiO_2–TiO_2 hybrid nanofluid samples

Sample names	**SiO_2/%**	**TiO_2/%**	**Water and EG mixture (5:1)/%**
SiO_2-0.5	0.5	-	99.5
SiO_2-1.0	1	-	99
SiO_2-1.5	1.5	-	98.5
TiO_2-0.5	-	0.5	99.5
TiO_2-1.0	-	1	99
TiO_2-1.5	-	1.5	98.5
SiO_2-TiO_2-0.5	0.25	0.25	99.5
SiO_2-TiO_2-1.0	0.5	0.5	99
SiO_2-TiO_2-1.5	0.75	0.75	98.5

3.2.2. Halloysite nanofluids

Halloysite originated from Turplu/Balıkesir, Turkey and was supplied by University of Pannonia. The stabilizing agents, including T80, oleylamine, GA, CTAB, SDS, SCMC and 1M sodium hydroxide (NaOH) were bought from Sigma-Aldrich (Saint Louis, MO, USA). Deionized water was used as BF.

Halloysite nanofluids were prepared by dispersing different amounts of halloysite nanoparticles in water. The volume fractions of halloysite content were 0.5, 1.0, and 1.5 %. Then, either stabilizing agents or 1 M NaOH solution were added to the nanofluids in the appropriate amounts to serve as stabilizing agents. The concentration of surfactant was kept at a minimum to primarily enhance nanoparticle dispersion while minimizing its impact on the thermophysical properties of the nanofluids. Halloysite nanofluids were sonicated at 130 W and

45 kHz using an ultrasonication instrument for 1 h. Table 7 shows halloysite nanofluid sample specifications.

Table 7. Specification of halloysite nanofluid samples in volume fraction

Sample names	Halloysite/%	Water/%	1M NaOH solution/%	SCMC/%
HNT-0.5	0.5	99.45	-	0.05
HNT-1.0	1	98.95	-	0.05
HNT-1.5	1.5	98.45	-	0.05
HNT-pH-0.5	0.5	98.5	1	-
HNT-pH-1.0	1	98	1	-
HNT-pH-1.5	1.5	97.5	1	-

3.2.3. Carbon nanofluids

CNS were prepared using the hydrothermal method [219]. Sucrose was put in an autoclave; then, the pH was set to 12 with NaOH solution. Under autogenous pressure at 180 °C, the mixture was treated for 12 h. The reaction's product was washed three times with distilled water then suspended in a 45 % ethanol-water solution. The suspension was centrifuged at 4000 rpm for 20 min. The settled material was filtered and dried at 70 °C after washing with warm distilled water overnight. The product was a brown powder [220]. The product was then studied with analytical methods.

CNP, BFs (EG and ethyl alcohol), and stabilizing agents (GA, TX, and T80) were purchased from Sigma Aldrich (Saint Louis, MO, USA).

The stability of nanofluids was investigated by using different kinds of solvents and stabilizing agents. Various ratios of the solvent mixture were considered as well, and in the following, I reported only those configurations that were observed as stable nanofluids. The nanofluids were obtained by adding CNS and CNP into the BF of water/ethanol and water/EG, respectively. The ratio of water and ethanol was 5:1. In the case of water and EG, the ratio was 1:1, and T80 was used as a stabilizing agent with a volume fraction of 3.3 %. For CNP, the different BFs were investigated; however, the nanofluids without stabilizing agent were not stable. To ensure stability, T80 was added in minimal necessary concentrations to improve nanoparticle dispersion while limiting its impact on the thermophysical properties of the nanofluids. The volume fraction of nanoparticle content was 0.5, 1.0, and 1.5 % (see Table 8). The CNS and CNP nanofluids were sonicated using an ultrasonication instrument for 1 h at 130 W and 45 kHz. The prepared nanofluids were stable over 3 days.

Table 8. Specification of CNS and CNP nanofluid samples in volume fraction.

Sample names	CNS or CNP/%	Water/%	Ethanol/%	EG/%	T80/%
CNS-0.5	0.5	82.9	16.6	-	-
CNS-1.0	1	82.5	16.5	-	-
CNS-1.5	1.5	82.1	16.4	-	-
CNP-0.5	0.5	48.1	-	48.1	3.3
CNP-1.0	1	47.85	-	47.85	3.3
CNP-1.5	1.5	47.6	-	47.6	3.3

3.2.4. Halloysite nanofluids in PBHT

Halloysite was used in PBHT as described above. In the preparation of nanofluid, the two-step method was used in this experimental work to make the halloysite nanofluids with different volume fractions (0.01, 0.05, 0.1, and 0.5 %) and by adding the halloysite to BF with pH = 12 medium, then homogenizing the nanofluids with ultrasonication process.

3.3. Nanomaterial characterization

3.3.1. SEM and energy dispersive X-ray analysis (SEM-EDX)

The nanomaterial samples were used, so the morphological characterization of nanomaterials was performed by an LEO 1440 XB scanning electron microscope (LEOGmbH, Oberkochen, Germany) at 5 kV with a secondary electron detector in a high vacuum mode. The nanomaterials' elemental composition was investigated by using energy-dispersive X-ray analysis (EDX) with a JEOL JSM-5500LV electron microscope (Tokyo, Japan).

3.3.2. Fourier transform infrared spectroscopy (FTIR)

FTIR spectra of nanomaterials were investigated by an Excalibur FTS 3000 BioRad FT-IR (Bio-Rad, Digilab, UK) in the 400–4000 cm^{-1} domain in transmittance mode, with a resolution of 4 cm^{-1} and a TGS detector, and the number of scans was 64. Approximately 1 mg of the sample was added to 300 mg of dried potassium bromide, and the mixture was pelleted for measurement.

3.3.3. Thermogravimetry/differential thermal analysis (TG/DTA)

The thermal properties of the nanomaterials were investigated using an STD 2960 thermogravimetry/differential thermal analysis (TA Instruments Inc., New Castle, DE, USA) device in platinum sample pans. The heating rate was 10 °C/min, and the temperature range was from room temperature to 800 °C in air and nitrogen, which has a velocity of 130 cm^3/min.

3.3.4. X-ray diffraction (XRD)

The crystal structure of the nanomaterials was studied by utilizing an X'PERT PRO MPD X-ray diffractometer (PANalytical, Almelo, Netherlands), with Cu K_α irradiation. The measurement results were recorded at a resolution of 3 degrees/min for the 2θ range of 5° to 65° with a step size of 0.025° for 25 mins with a divergent slit. Before the measurement, approximately 1 mg of the sample was uniformly distributed on the sample holder.

3.3.5. Raman spectroscopy

Raman spectrum was obtained utilizing a Jobin Yvon Labram Raman spectrometer (Horiba, Kyoto, Japan) containing an Olympus BX41 microscope (Olympus, Tokyo, Japan) equipped with a 532 nm green Nd-YAG laser, which was focused by 20x objective. To avoid the sample's thermal degradation, D0.3 intensity filter was utilized to lower the laser power. The measurement range was 72–1560 cm^{-1} with 3 cm^{-1} resolution. The exposure time was 15 seconds in order to produce intensive peaks.

3.3.6. Specific surface area analysis

According to the multipoint Brunauer–Emmett–Teller technique, the surface area analysis of CNS and CNP and nanoparticles was determined by utilizing nitrogen adsorption isotherms from an automated volumetric nitrogen gas adsorption device (NOVA 2000e) at −196 °C after outgassing the samples 25 °C.

3.3.7. X-ray photon electron spectroscopy (XPS)

The XPS measurements of the CNP and CNS were performed using a SPECS PHOIBOS 150 MCD XPS instrument. For the measurements, a 150 W (14 kV) X-ray source was applied with Al Kα radiation, a pass energy of 40 eV, and a dwell time of 0.3 s. Before the measurements, the samples were kept in a vacuum during the night. The curves were deconvoluted using CasaXPS software.

3.4. Nanofluid characterization

3.4.1. Ultraviolet-visible spectroscopy (UV-Vis)

The stability of carbon nanomaterial nanofluids was tested by using an Avantes AvaSpec-2048 Fiber Optic spectrometer (Avantes BV, Apeldoorn, Netherlands). After a period, 20 µL of each sample was diluted with 2 mL of water in a quartz cuvette, and their maximum absorbance was recorded. The detector was CCD. Deuterium and halogen lights were used as the light source, and the measurement range was from 250 to 800 nm. The resolution was 2.4 nm.

3.4.2. Viscosity measurement

The viscosity of the prepared nanofluids was investigated with three replicas using an Anton Paar Physica MCR 301 (Anton Paar, Ashland, VA, USA) rotation viscometer at 15 different shear rates and five temperatures. The amplitude was 5 %. The range of angular frequency was 100 to 2000 s^{-1}.

3.4.3. Thermal conductivity measurement

Based on the modified transient plane source approach, an SKZ1061C TPS Thermal Conductivity Tester (SKZ Industrial, Shandong, China) was used to measure the thermal conductivity of CNS and CNP nanofluids. All nanofluids were measured three times at five temperatures (20, 30, 40, 50, and 60 °C). The mean value and standard error were calculated for use in the figures. In order to increase the temperature of the nanofluids at the defined setpoint, a temperature-controlled oven was used.

3.4.4. PBHT measurement

In PBHT experiments, the sleeve is constructed of a solid copper shaft with three holes designed at various radial angles and positions across the axial width, as shown in Figure 9. I measured the bulk and surface temperatures around the heating medium by using four K-Type thermocouples that had been previously tuned [221]. Figure 10 shows the complete apparatus parts. Another heating element was placed inside the chamber to provide more heating sources. The dimensions of this cylindrical tube are 22 mm external diameter and 1 mm thickness. The tube is filled with copper sleeves manufactured in the laboratory. The chamber pool is made of stainless steel metal with the following dimensions (length = 155 mm, width = 120 mm, and height = 310 mm). The type of reflux condenser used (Allihn type NS29/32) has a 400 mm long jacket.

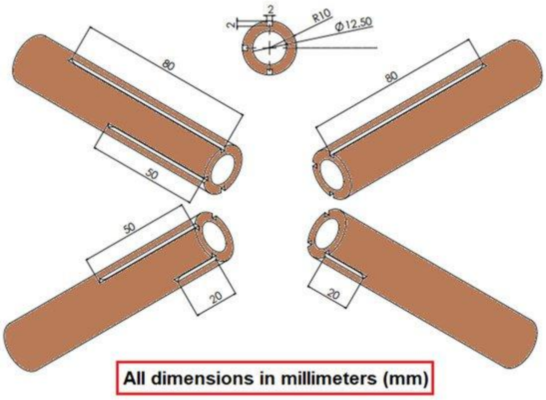

Figure 9. The isometric view of the copper sleeve

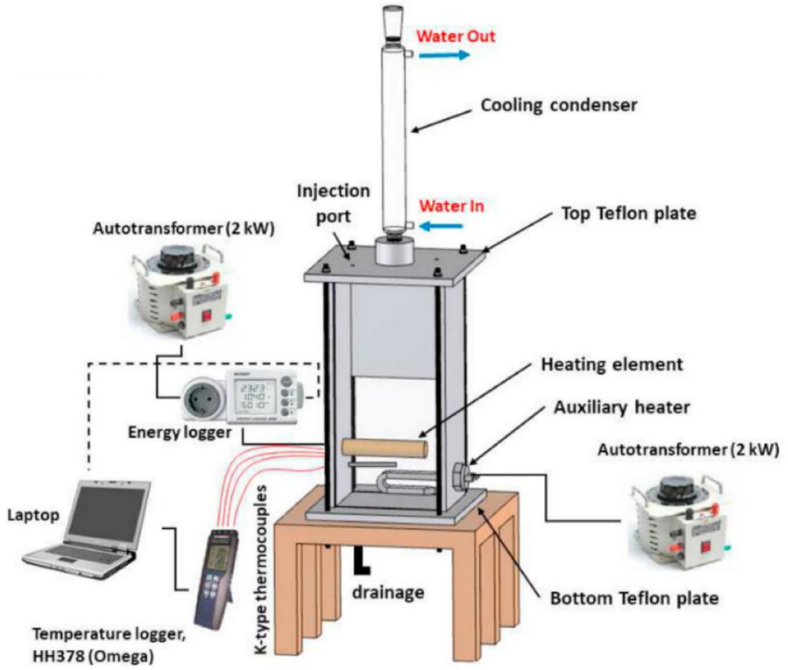

Figure 10. Schematic picture of the pool boiling device [158]

3.4.5. Digital optical microscopy (DOM)

The measurements of the DOM were carried out with the Keyence VHX-5000 digital optical microscope (Keyence, Itasca, IL, USA). There are the DOM measurement pictures for the four-volume fractions (0.01, 0.05, 0.1, and 0.5 %) with 500× and 5000× magnifications.

3.5. CFD study

3.5.1. Pre-processing

This section details the meshing process for the pipe and the geometric model used. The preprocessing phase can generally be divided into two main steps: the creation of the geometric model and the generation of the mesh for the flow domain.

The two-dimensional geometry of the pipe was created numerically with $L = 1.5$ m length, $d = 16$ mm hydraulic diameter, and $wt = 2$ mm wall thickness. Figure 11 represents the arrangement and flow in a pipe.

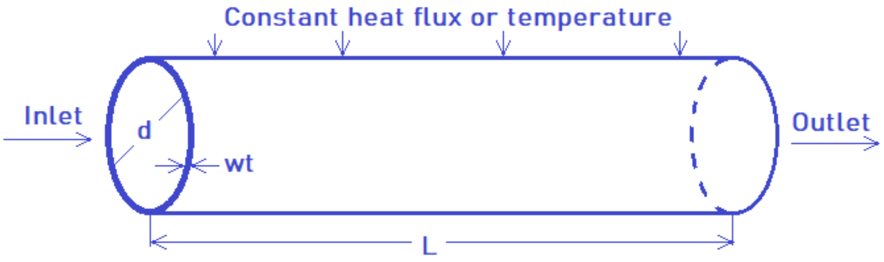

Figure 11. Scheme of the model.

For the purpose of this study, the flow inside the tube was assumed to be symmetrical and steady. The flow domain was meshed using quadrilateral elements, chosen for their simplicity and efficiency in capturing the flow characteristics. The meshing within the flow domain is depicted in Figure 12. The cross-section includes two inflation layers near the wall, designed to accurately capture boundary layer effects. These layers have a growth rate of 20 %, a transition ratio of 10^{-4}, and a bias factor of 50 applied to edge sizing, ensuring smooth gradation and effective resolution near the pipe walls.

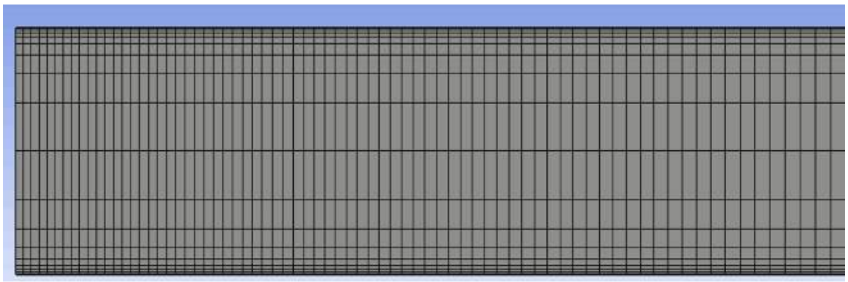

Figure 12. Meshing of the flow domain

Table 9 presents the mesh quality metrics for the computational domain. The results demonstrate exceptionally high mesh quality, with skewness values ranging from 0.0013 to 0.0027, indicating near-perfect cell shapes. Orthogonal quality was also outstanding, ranging from 0.999 to 1, ensuring highly accurate flux calculations. While the maximum aspect ratio reached 16.98, this was localized and did not compromise overall element regularity, as evidenced by the ideal Jacobian ratio values between 1 and 1.01. These robust metrics collectively confirm that the mesh is of sufficient quality to provide reliable and accurate simulation outcomes.

Table 9. Indicators of mesh quality

Indicators	Minimum quality	Maximum quality
Skewness	0.0013	0.0027
Aspect ratio	1.003	16.98
Orthogonal quality	0.999	1
Jacobian ratio	1	1.01

3.5.2. Solver settings

Turbulence modelling

A range of turbulence models are available, each with specific strengths for predicting turbulent flow characteristics under different conditions. For the analysis of nanofluids within pipelines in this study, the standard $k - \varepsilon$ turbulence model was chosen due to its robustness and proven effectiveness in simulating turbulent flows. This model, which solves transport equations for the turbulence kinetic energy (k) and its dissipation rate (ε), is particularly wellsuited for capturing the key dynamics of turbulent flow in pipelines, making it an appropriate choice for the current investigation.

Solution initialization

Selecting an appropriate time step size is crucial for balancing numerical accuracy and computational efficiency. Smaller time steps can enhance the quality of the simulation by preventing issues such as negative cell volumes, but they also increase the computational cost. Conversely, larger time steps can reduce the simulation time, but they carry a higher risk of numerical instability. However, in my study, the simulation was conducted under steady-state (stationary) conditions, which assumes that the flow properties do not change over time. Therefore, the options for setting the number of time steps and the time step size were not applicable, as the solver directly computes the final equilibrium state without the need to simulate the temporal evolution of the flow.

Explicit relaxation factors were applied as solution controls, with pressure set to 0.3, momentum to 0.7, turbulent kinetic energy to 0.8, and turbulent dissipation rate also to 0.8. Additionally, under-relaxation factors were used to control variable updates within the pressure-based solver. Other variables, including density, body forces, turbulent viscosity, and energy, were set to 1. Initial calculations employed default under-relaxation parameters, which are optimized for a wide range of cases, as detailed in Table 10.

Table 10. Under-relaxation factors

Equation	Under-relaxation factors
Pressure	0.3
Density	1
Body forces	1
Momentum	0.7
Turbulent kinetic energy	0.8
Turbulent Dissipation rate	0.8
Turbulent viscosity	1
Energy	1

Material properties

SiO_2-TiO_2 nanoparticles and water/EG mixture as BF were considered hybrid nanofluids, and these properties were investigated. The hybrid nanofluids in point were considered incompressible, Newtonian, and single-phase fluids. Table 11 illustrates the density (ρ), k, dynamic viscosity (μ), and specific heat (c_p) of hybrid nanofluids.

Table 11. The basic properties of SiO_2-TiO_2 hybrid nanofluids for different volume fractions.

Temperature **°C**	ρ **g/cm³**	k **W/(mK)**	**μ** **mPas**	c_p **J/gK**
0.50 % SiO_2-TiO_2				
20	1.033	0.510	1.789	3848
30	1.030	0.535	1.470	3863
40	1.026	0.549	1.152	3888
50	1.022	0.561	0.978	3903
60	1.017	0.568	0.815	3926
1.00 % SiO_2-TiO_2				
20	1.044	0.522	2.054	3799
30	1.041	0.546	1.594	3814
40	1.037	0.56	1.313	3838
50	1.033	0.571	1.079	3853
60	1.028	0.578	0.885	3875
1.50 % SiO_2-TiO_2				
20	1.055	0.531	2.281	3734
30	1.052	0.553	1.825	3766
40	1.048	0.568	1.445	3789
50	1.045	0.579	1.212	3804
60	1.039	0.587	1.008	3825

The experimental measurements were conducted at the temperature range from 20 °C to 60 °C. Some empirical formulae in Table 1 and Table 2 use the Pr numbers ratio as temperature correction. Therefore, the prediction was applied for the hybrid nanofluid's Pr numbers extension to 100 °C, as Table 12 reports. The prediction method can be summarized as follows: The ratio of the nanofluid's Pr number against the water's Pr number in the measurement range was calculated and extended by linear regression. Figure 13 visualizes the measured and extended values. As shown, the extended Pr numbers are the natural continuity of the measured data, as the third-order polynomial curve R^2 values confirm. If needed, this prediction method works for other properties as well. This is called regression analysis and is used in a lot of research [222], [223].

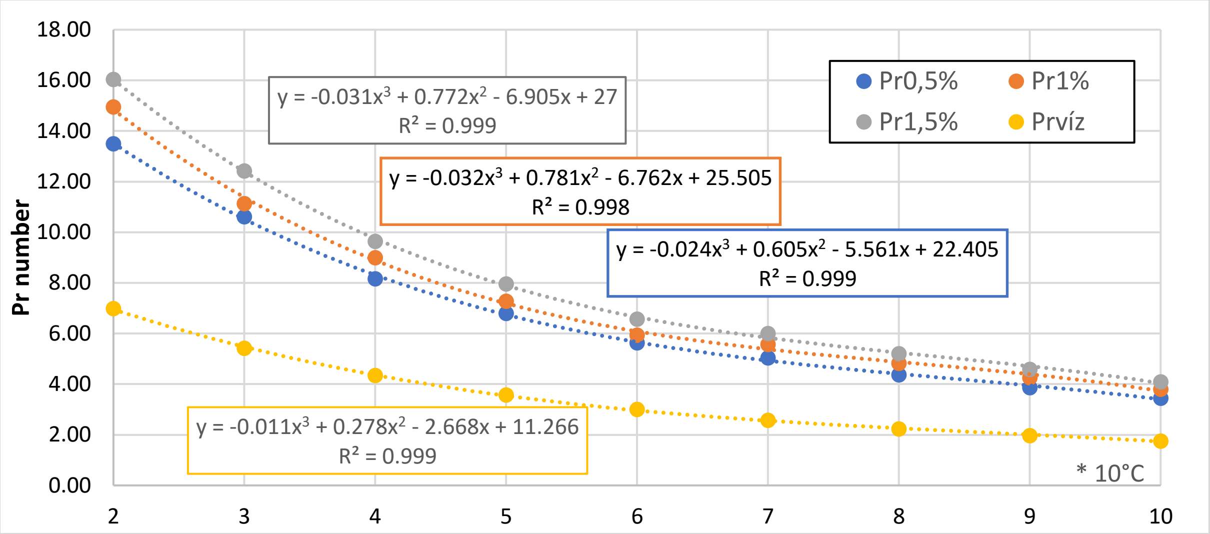

Figure 13. The measured and the predicted values of the Pr numbers over temperatures for different volume fractions.

Table 12. The Pr numbers of SiO_2-TiO_2 hybrid nanofluids for different volume fractions. (Gray background shows the predicted values.)

	Fractions	**0.50 %**	**1.00 %**	**1.50 %**
		Pr numbers		
Temperature, ºC	20	13.50	14.95	16.04
	30	10.62	11.14	12.43
	40	8.16	9.00	9.64
	50	6.80	7.28	7.96
	60	5.63	5.93	6.57
	70	5.05	5.57	6.00
	80	4.37	4.83	5.20
	90	3.86	4.26	4.59
	100	3.45	3.80	4.10

The empirical formulae should always follow the specific order related to the formulae. Generally, the characteristic length is specified, and the characteristic temperature is defined so that one should use it to determine fluid properties. When the formula has an extended application range, the *Re* and *Pr* numbers appear, and specific corrections may also count the specialties of the arrangement. A such correction could be the length-to-diameter ratio or the Pr numbers ratio. Figure 14 illustrates the effect that the properties variation may mean.

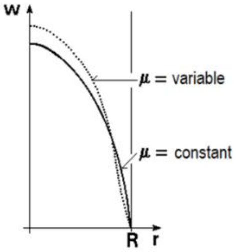

Figure 14. Velocity profiles for constant and variable viscosity [224]

Since the mean fluid temperature plays a central role in the HTC calculation, Equation (6) shows its calculation.

$$T_{mean,f} = \frac{\int_0^R u(r)\cdot\rho(T(r))\cdot C_p(T(r))\cdot T(r)\cdot dr}{\int_0^R u(r)\cdot\rho(T(r))\cdot C_p(T(r))\cdot dr}, \quad (6)$$

where u is velocity, $T_{mean,f}$ practically is the so-called completely stirred temperature.

Boundary conditions

In numerical experiments, the inlet temperature of the flow was 30 °C. Water was used for validating the CFD analysis. The inlet velocity was uniform. Static pressure conditions at the entrance and stagnation pressure conditions at the outlet were applied. Since the subject of my study was turbulent forced flow, the Re number was greater than 5000 in all investigated cases. The fluid's velocity and temperature were varied so that the Re number remains in the range of 5000 - 17000.

The inner pipe wall was assumed to be hydraulically smooth, showing a negligible roughness coefficient. Furthermore, no-slip boundary conditions were applied to all domain walls, implying that the fluid velocity at the wall surfaces was identical to the wall velocity, which was zero. The CFD study applied (a) a constant heat flux of 7955 W/m^2 and (b) a constant tube wall temperature of 67 °C.

3.5.3. Simulation convergence

Residuals for variables such as velocity, continuity, and turbulent kinetic energy were used as indicators of convergence. Figure 15 graphically depicts the convergence behavior, showing residuals plotted for $Re = 5000$. The figure demonstrates the gradual stabilization of the continuity residuals. Convergence criteria were set, requiring residuals to fall below 10^{-8} for the continuity equation and below 10^{-6} for other equations. Simulations conducted at $Re = 8000$, 11000, 14000, and 17000 adhered to these criteria, confirming the stability and convergence of the simulation results.

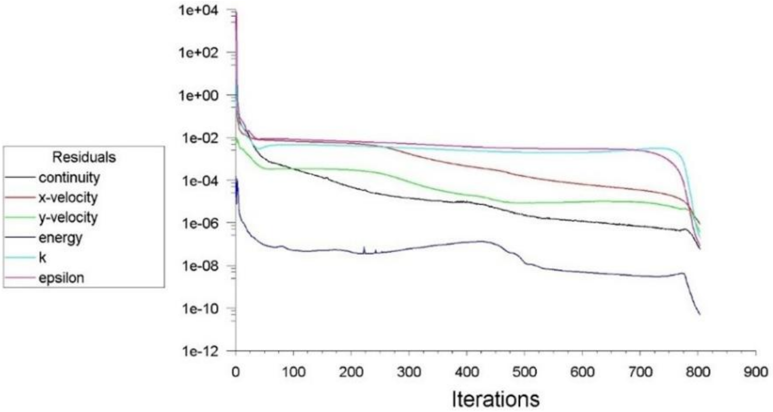

Figure 15. Residuals convergence for Re = 5000

3.6. Measurement performed by the doctoral candidate and those together with the help of collaborators

I carried out my research work under the guidance of my supervisor, associate professor Dr. Imre Miklós Szilágyi. I performed the measurements at the BME Department of Inorganic and Analytical Chemistry: FTIR, XRD, TG/DTA, SEM-EDX, and UV-Vis. My students Marcel Bohus (BSc and MSc), Zalán István Várady (BSc and MSc), Ahmed Qani Alkurdi (MSc), and Ahmed Baqer (MSc) also participated in the preparation of the samples and the execution of the measurements.

I received help from György Bosznai and Dr. Krisztina László at the Surface Chemistry Group of the Department of Physical Chemistry and Materials Science of BME in the specific surface area measurements and the result evaluation. The Raman spectra were taken by Tamás Igricz at the Department of Organic Chemistry and Technology of BME. The high-resolution SEM images were taken by Dr. István Lukács at the Institute of Technical Physics and Materials Science of the Hungarian Academy of Sciences. I evaluated the measurement results of SEM and Raman. The TEM images were taken by Dr. Klára Hernádi and Anna Szabó at the Applied & Environmental Chemistry Department of SZTE.

The XPS measurements and result evaluation were carried out by Samu Gergely Ferenc and Dr. Zoltán Kónya at the Department of Applied and Environmental Chemistry of SZTE. The thermal conductivity of the prepared nanofluids was measured at the Department of Energy Engineering of BME with the help of Dr. Gyula Gróf. János Molnár helped to measure the viscosity of the nanofluids at the Department of Physical Chemistry and Materials Science of BME. I evaluated the thermal conductivity and viscosity results.

Dr. Mohammed Saad Kamel and Dr. Lezsovits Ferenc performed the PBHT measurements and the result evaluation at the Department of Energy Engineering of BME. The DOM images of the surface of the heating tube were taken, and the DOM results were evaluated by Dr. Alfréd Menyhárd at the Department of Physical Chemistry and Materials Science of BME. Dr. Gyula Gróf at the Department of Energy Engineering of BME guided and advised me throughout the entire process of performing the CFD simulation. With his expertise and valuable advice, he assisted me in the formulation of simulation methodology, background research, and evaluation of simulation results.

4. Results and analysis

4.1. Characterization of halloysite nanofluid

Figure 16 shows the XRD pattern of the halloysite, where distinct diffraction peaks are explained by the crystalline property of the halloysite. The primary aim of the XRD measurement was to confirm the crystalline nature of the halloysite and to identify any other mineral phases present in the sample. This XRD pattern was indexed to ICDD (International Centre for Diffraction Data) 00-029-1487. The pattern had peaks corresponding to the aluminum silicate hydroxide. The diffraction peaks at 2θ = 12.0, 20.1, 24.6, 35.0, 37.9, 54.5, and 62.6 corresponded to (001), (100), (002), (110), (003), (210), and (300) planes, respectively [225]. The diffraction peak at 35.0° is more visible than at 37.9°. The presence of the (001) peak at 2θ of 12.0° corresponded to a layer spacing of 0.73 nm. The dehydrated state was also confirmed by the (100) diffraction peak at 2θ of 20.1° (0.44 nm). The reflection at 2θ of 26.6° was also observed, which indicated the presence of quartz, which is a very common mineral constituent. The material was characteristic of tubular halloysite [226], [227]. Through this XRD analysis, the crystalline nature of the halloysite, validated the expected tubular structure, and identified the presence of quartz was confirmed. With these characteristics it can contribute to improving the thermal conductivity of nanofluids.

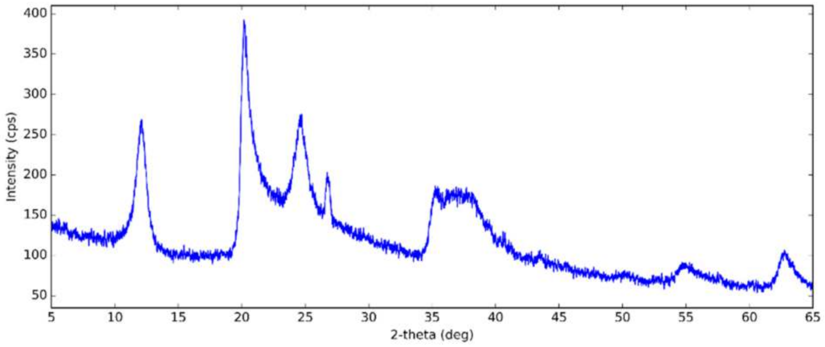

Figure 16. X-ray diffraction (XRD) pattern of halloysite

Figure 17 shows the SEM image of the morphological structure of the halloysite. From SEM studies, it can be seen that the sample used was uniform in content, containing nanotubes with infrequent particle agglomerates. Between the halloysite, some platy particles were presented due to residual kaolinite. By measuring the diameter at five points of the SEM images, the mean outer diameter and the mean length were determined. The diameter and length were 58 and 436 nm, respectively. The aspect ratio was calculated as ca. 7.5. Compared to the halloysite used by Alberola et al. [50], the halloysite in this study was smaller. This could give the advantage of higher thermal conductivity and greater stability.

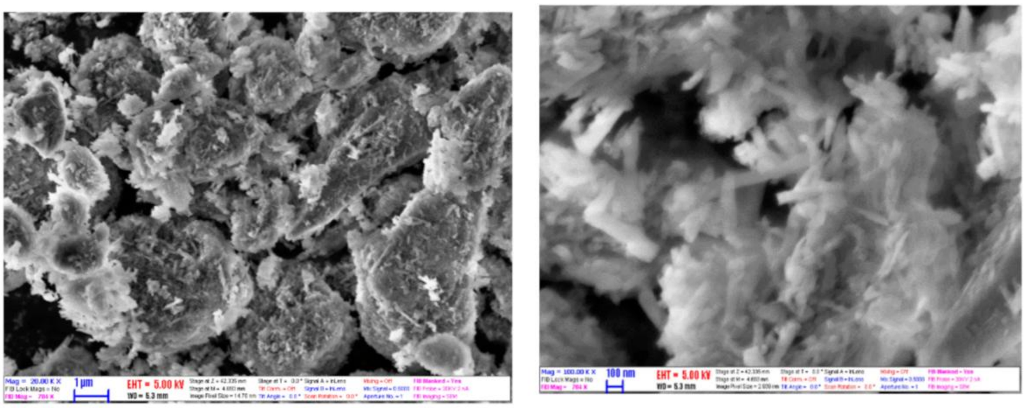

Figure 17. SEM images of halloysite with magnification ×20000 (left) and ×100000 (right).

In addition to the above results, TEM images were also recorded, as shown in Figure 18. The dimensions of the halloysite were as follows: the length and the diameter of the halloysite were harmonized with SEM results. The TEM images confirmed the tubular morphology of the used halloysite.

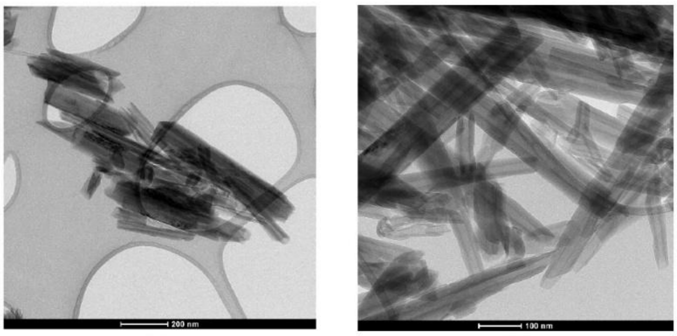

(a) (b)

Figure 18. TEM images of halloysite (a) scale bar, 200 nm (b) scale bar, 100nm.

The examination of functional groups of the used nanomaterials helps the effort to understand the structure of the nanomaterials. Figure 19 shows the FTIR spectrum of the halloysite. The two infrared active modes centered at around 3694 and 3617 cm^{-1} were assigned to the stretching vibration (O–H) bonds of halloysite [228]. The peak at around 1630 cm^{-1} and broadband around 3000-3600 cm^{-1} confirmed the typical bending vibration of absorbed water. This peak in halloysite was more intense and broader than in kaolinite [229]. The peak at 1110 cm^{-1} was caused by the stretching mode of apical Si–O bonds. The peaks at 1029 and 477 cm^{-1} were attributed to the Si–O–Si asymmetric stretching and bending vibrations. There was another minor peak around 935-940 cm^{-1} attributed to the inner surface O-H. The peaks at 911 and 540 cm^{-1} referred to the bending vibration of Al–O–H and Si–O–Al bonds, respectively. The peaks at 789 and 754 cm^{-1} were assigned to OH translation vibrations of halloysite [50].

The 694 cm^{-1} band could be characteristic of crystalline quartz (in harmony with the XRD results) or Si-O.

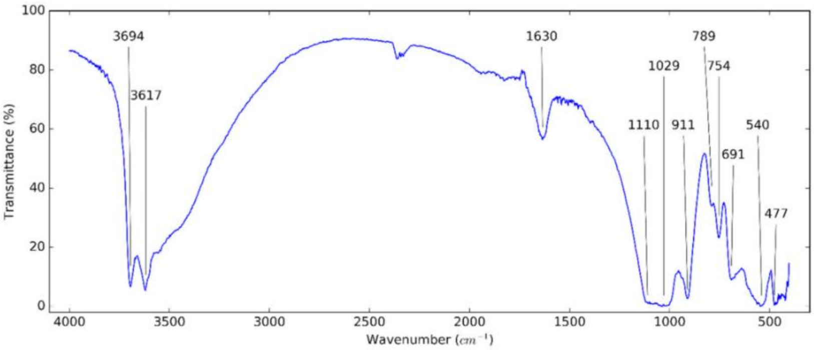

Figure 19. FTIR spectrum of halloysite.

In Figure 20, the Raman spectrum of the halloysite can be observed. The peak centered at 205 cm^{-1} referred to AlO_6 octahedron (A_{1g}). The peaks at 247 (A_1) and 277 cm^{-1} (B_2) were attributed to the internal vibrations of the O–H–O triangle. The three vibrational modes of the SiO_4 tetrahedra were presented at 334, 428, and 469 cm^{-1}. The peaks at 647, 710, and 747 cm^{-1} were caused by Si–O–Al translation. The peaks at 793 and 910 were assigned to the OH translation and liberation, respectively [230]. The peak at 1113 cm^{-1} (A_1) confirmed the stretching vibrations of the Si–O bond [231].

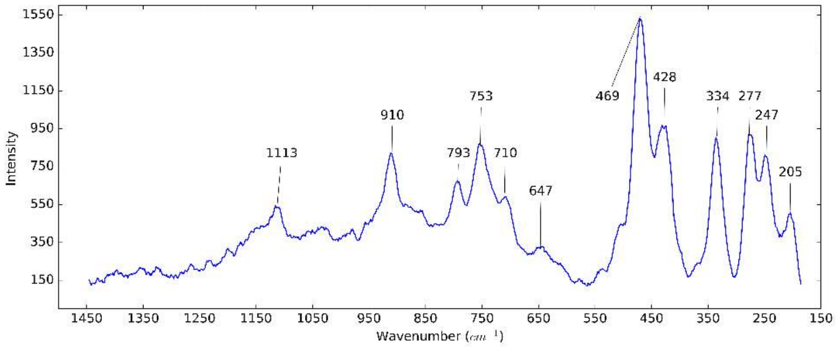

Figure 20. Raman spectrum of halloysite.

EDX provided the qualitative composition of the used material. The main components of the halloysite included Al, Si, and O (H can not be seen). Table 13 contains the EDX results of the halloysite (Appendix A). The values in the table were the average of the results obtained at five measurement points in the atomic percentage. These values (Al:Si:O = 1:1.03:4.38) were similar to the EDX results (Al:Si:O = 1:1.13:5.42) obtained from Tayser et al. [232]. The oxygen content indicated that the used halloysite did not have H_2O molecule.

Table 13. Energy-dispersive X-ray (EDX) analysis results of halloysite.

Nanoparticles	**Atomic%**		
	Al	**Si**	**O**
Present work	15.6	16.1	68.3
Tayser et al. [232]	13.2	15.0	71.8

Figure 21 shows the TG/DTG/DTA curves of halloysite samples in air (Appendix B). At around 150 °C and below, mass losses referred to the loss of absorbed water (2 %) on the surface and interlayer [233]. From 150 °C to 400 °C, the interlayer water was removed completely [234], while at 400–700 °C, the Al–OH groups of halloysite were dehydroxylated with a loss of approximately 9 % and the "meta-halloysite" ($Al_2O_3{\cdot}2SiO_2$) was formed [233]. In the differential thermal analysis curve, because of the removal of water, the process was endothermic, and then the structural rearrangement of the material – above 800 °C – was exothermic [235].

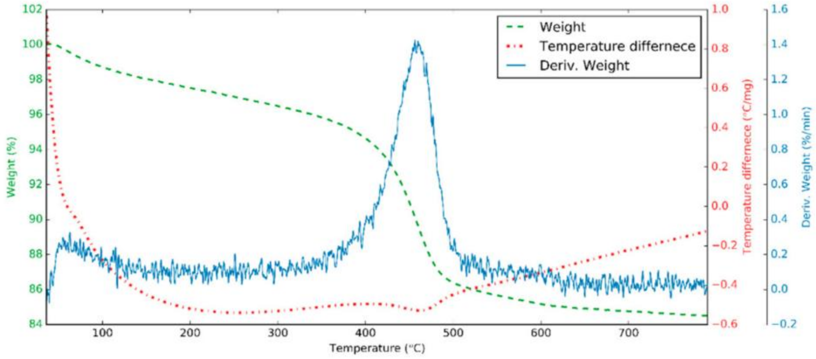

Figure 21. TG/DTG/DTA curve for halloysite in air.

The ZP of 0.5 % halloysite nanofluids with different stabilizing agents is shown in Table 14. To improve the stability of halloysite nanofluids, different stabilizing agents were utilized, each at a concentration of 0.05 %, including CTAB, SDBS, GA, SCMC, oleylamine, and TX. Among these, SCMC exhibited the best performance, yielding a ZP of -30.5 mV, which is indicative of a relatively stable colloidal system. The concentration of the surfactants was optimized by gradually increasing the concentration until stable nanofluids were achieved. Preliminary tests were conducted to determine the optimal concentrations used in the final experiments.

The effectiveness of SCMC as a stabilizing agent can be understood by considering the nature of the surfactants used. Among the surfactants, T80, GA, and oleylamine are non-ionic, CTAB is cationic, while SDBS and SCMC are anionic. The halloysite surface, which carries a positive charge due to the presence of aluminum oxide, as presented in the FTIR and Raman spectrum, interacts more effectively with anionic surfactants like SCMC and SDBS. SCMC, being a thickener, not only provides strong electrostatic repulsion due to its anionic nature but also induces steric repulsion, which enhances the stability of the nanoparticles by preventing agglomeration. This dual mechanism of stabilization – electrostatic and steric – makes SCMC particularly effective in maintaining a stable dispersion of halloysite nanoparticles in the nanofluid. Consequently, SCMC was found to be the best-stabilizing agent for halloysite nanofluids, as evidenced by the ZP values and visual observation of sedimentation behavior.

Table 14. ZP of 0.5 % halloysite nanofluids with different stabilizing agents.

Stabilizing agents	*Without stabilizing agents*	T80	CTAB	Oleylamine	GA	SDBS	SCMC
ZP of 0.5% halloysite nanofluid (mV)	-11.8	7.9	20.4	24.2	-17	-26.8	-30.5

Colloidal solutions with ZPs as low as –30 mV have acceptable stability. Table 15 shows the ZP values of halloysite nanofluids with different volume fractions. In these experiments, the concentration of the SCMC stabilizing agent was kept constant at 0.05 % across all tested nanofluid samples, regardless of the volume fraction of halloysite. With SCMC stabilizing agent, the ZP of 0.5, 1.0, and 1.5 % halloysite nanofluids was −30.5, −32.2, and −31.2 mV, respectively, while adjusting the pH of the colloidal solutions to 12, the ZPs were −33.4, −39.7 and −32.4 mV for 0.5, 1.0 and 1.5 %, respectively. These values indicated the stability of nanofluids. Also, visual observation verified that these nanofluids were stable over 3 days. Compared to Alberola's result [50], the ZP in my study was lower.

Table 15. ZP of halloysite nanofluids with different volume fractions.

Nanofluids	SCMC-0.5	SCMC-1.0	SCMC-1.5	pH-12-0.5	pH-12-1.0	pH-12-1.5
ZP (mV)	−30.5	−32.2	−31.2	−33.4	−39.7	−32.4

The viscosity of the nanofluids is important parameters determining the heat transfer. The viscosity of the BF and halloysite nanofluids at different shear rates was measured for three volume fractions of 0.5, 1.0, and 1.5 % at five temperatures: 20, 30, 40, 50, and 60 °C. Figure 22 shows the shear rate–shear stress diagram of 0.5 % halloysite nanofluids with SCMC stabilizing agent at different temperatures. The shear stress of halloysite nanofluids fell with increasing temperature and increased with increasing fractions of nanofluids. The increase in temperature caused the Brownian movement and thermal motion of molecules to be higher; thus, the viscosity of nanofluids decreased [166]. The shear rate of halloysite nanofluid was almost linearly dependent on the shear rate. It was concluded that the nanofluids were Newtonian.

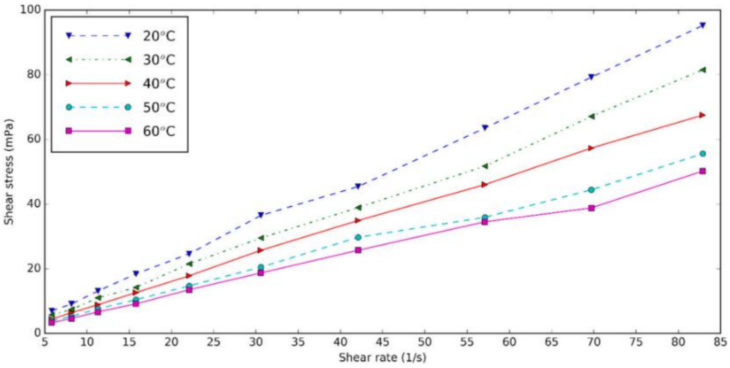

Figure 22. Shear stress–shear rates diagram of nanofluids for volume fraction of 0.5 %.

Figure 23 shows the relative viscosity of prepared halloysite nanofluids at different temperatures. Relative viscosity was obtained by dividing the viscosity of nanofluids by that of the BF. It could be seen that the viscosity was higher with nanoparticle content due to the clusters formed from nanoparticles. Temperature played an essential role in the relative viscosity. This meant that with the increasing temperature, the viscosity of the BF decreased more than that of the nanofluids. Compared to the halloysite nanofluids used at pH = 12 without stabilizing agent, the relative viscosity of nanofluids containing the stabilizing agent did not have a significant difference. With stabilizing agent, the halloysite nanofluids had the lowest relative viscosity of 1.09 for 0.5 % volume fraction at 20 ºC and the highest relative viscosity of 1.31 for 1.5 % at 60 ºC. The relative viscosities of halloysite nanofluids at pH = 12 were 1.09 for 0.5 % at 20 ºC and 1.27 for 1.5 % and 60 ºC.

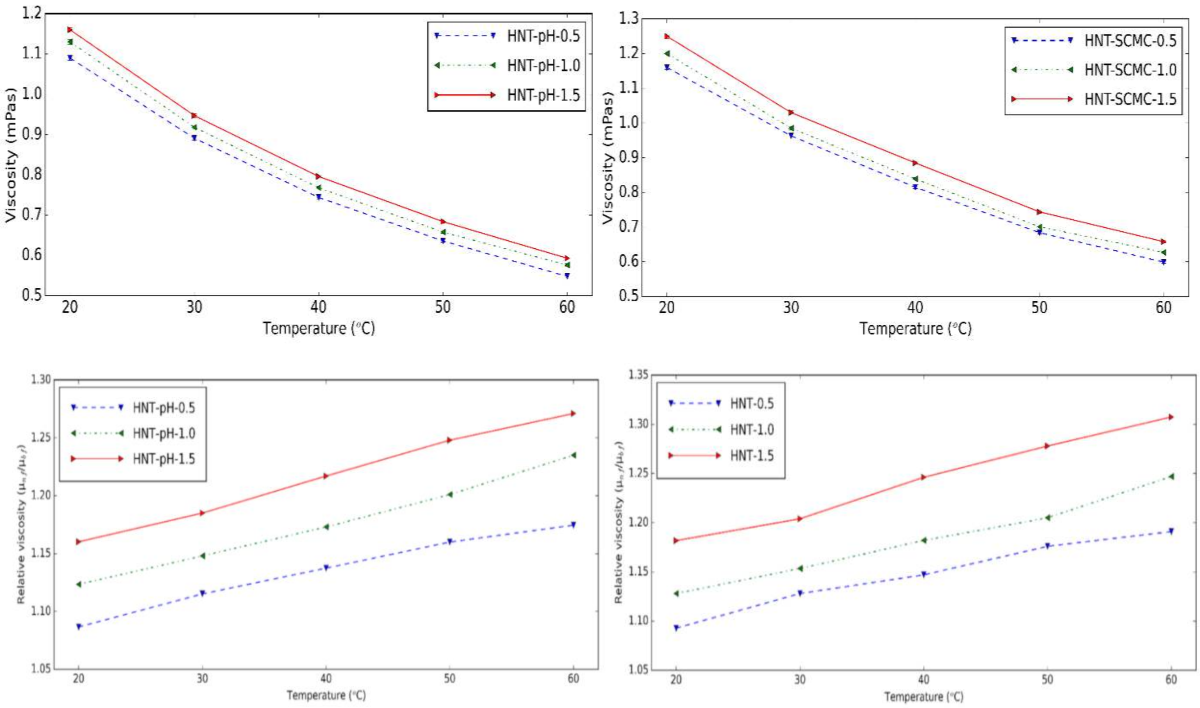

Figure 23. Viscosity and relative viscosity of halloysite nanofluids for different volume fraction at different temperatures (left: pH = 12, right: using SCMC stabilizing agent).

The thermal conductivity of halloysite nanofluids at different temperatures is presented in Figure 24. The device was reliable within 0.6 % error when the calibration measurement was verified for water. The nanofluids showed greater thermal conductivity than the BF at experimental temperatures. Halloysite nanofluids with SCMC stabilizing agent gave 4.48 %, 6.03 %, and 7.93 % thermal conductivity increments at 0.5, 1.0, and 1.5 % in comparison with the BF at 20 °C, respectively. The thermal conductivity increments of halloysite nanofluids at pH = 12 were 2.64 % and 6.90 % at 20 ºC for 0.5 and 1.5 %, respectively. By increasing the temperature, the thermal conductivity of nanofluids increased due to the augmentation in the Brownian motion of the solid.

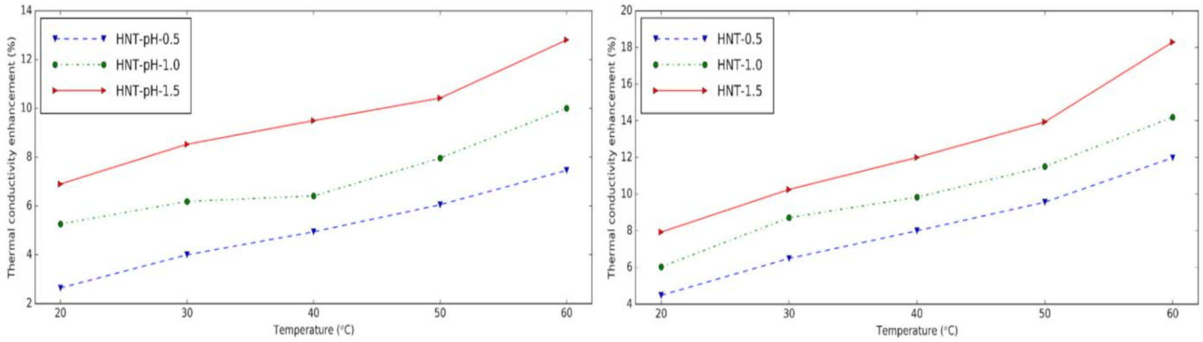

Figure 24. Thermal conductivity and enhancement of thermal conductivity of halloysite nanofluids for different volume fractions at different temperatures (left: pH = 12, right: using SCMC stabilizing agent).

It could be seen that when the nanoparticle content in nanofluids increased, the thermal conductivity also increased because of the higher number of nanoparticles presented in the nanofluid. The thermal conductivity enhancement of nanofluids containing stabilizing agent was slightly higher than nanofluids with pH = 12. It was concluded that similar to changing pH, applying the stabilizing agent also supported using halloysite in the preparation of nanofluids. Compared to the results from Alberola et al. [50], the thermal conductivity of the nanofluids in this study was greater. This may be due to the smaller length and diameter of halloysite used in this research. Smaller halloysite nanotubes have a higher surface area-to-volume ratio, which can enhance their interaction with the BF and improve heat transfer efficiency. As a result, the nanofluids in this study exhibited higher thermal conductivity compared to those using larger halloysite nanotubes.

4.2. Halloysite nanofluids in PBHT

This was the first applied research of halloysite nanofluids in PBHT. This might open a way to using halloysite nanofluids in a variety of engineering applications. In the preparation of nanofluid, the two-step method was used in this experimental work to make the halloysite nanofluids with different volume fractions (0.01, 0.05, 0.1, and 0.5 %) and by adding the halloysite to BF at pH = 12, then homogenizing the nanofluids with ultrasonication process. The pH = 12 was chosen instead of the stabilizing agents to avoid the effect of heat on them.

In Figure 25, there are the DOM pictures of the heating tube surface for the solutions of 0.01, 0.05, 0.1, and 0.5 volume fractions with 500× and 5000× magnification. These pictures were taken after each PBHT experiment. From the pictures, it was clearly seen what the difference was between the clean sample (free of deposition) and the samples with the nano-powder deposited on the external layer of the heating tube. Also, it could be noticed that the deposition ratio varied from one sample to another depending on the volume fraction. This deposition caused a negative effect on the heat transfer process as it made a nano-porous layer which led to the deactivation of the nucleation site of the bubble formation.

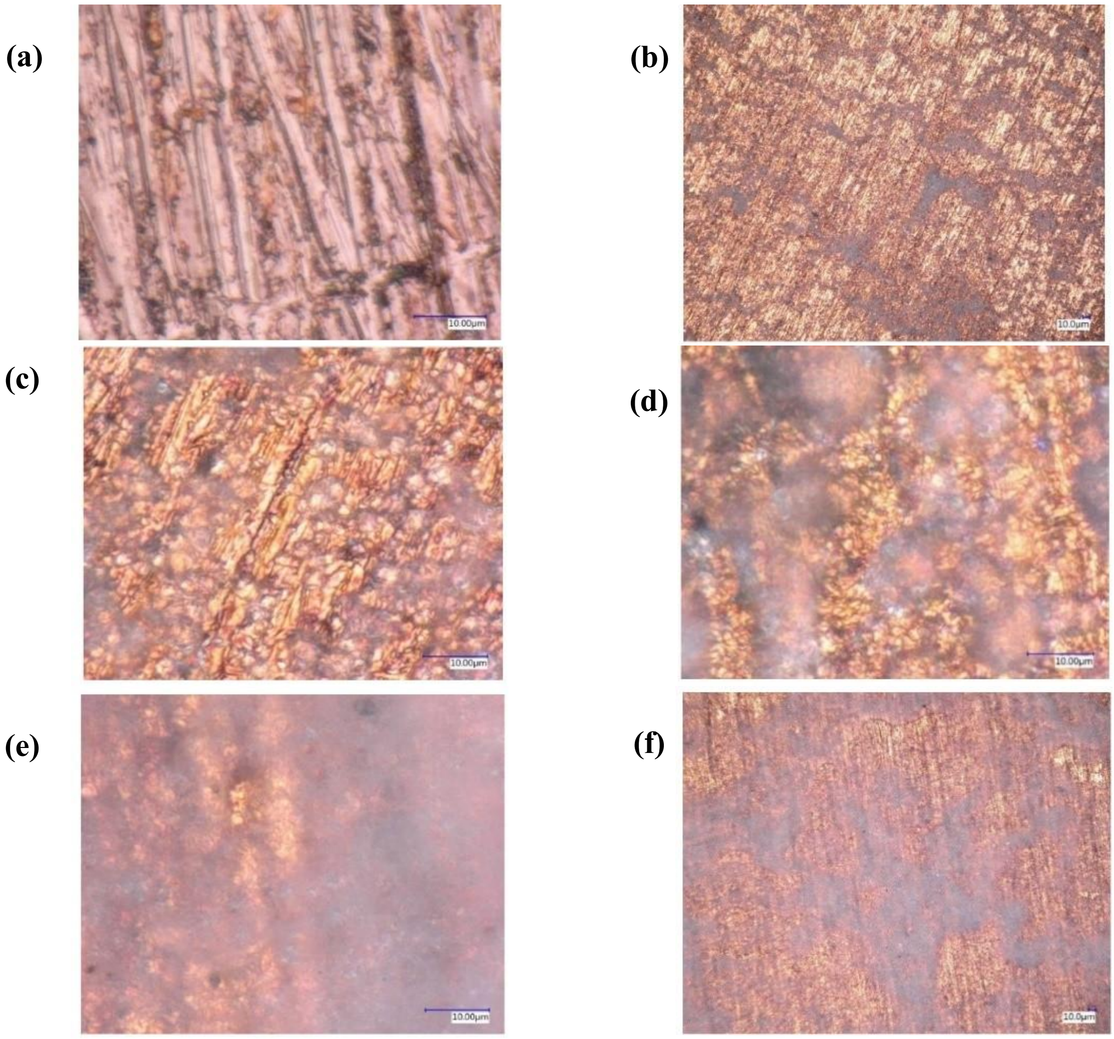

Figure 25. Deposition of the nanoparticles (a) 5000× Clean sample (without deposition), (b) 500× for 0.01 %, (c) 5000× for 0.05 %, (d) 5000× for 0.1 %, (e) 5000× for 0.5 %, and (f) 500× for 0.5 %.

In order to confirm the reliability of the boiling chamber, water was used for the investigation of PBHT. Then, our results of the pool boiling cure for water were compared with the previous studies [236], [237], [238], [239], as shown in Figure 26. From the results, it was seen that the experimental results in the present study could be accepted.

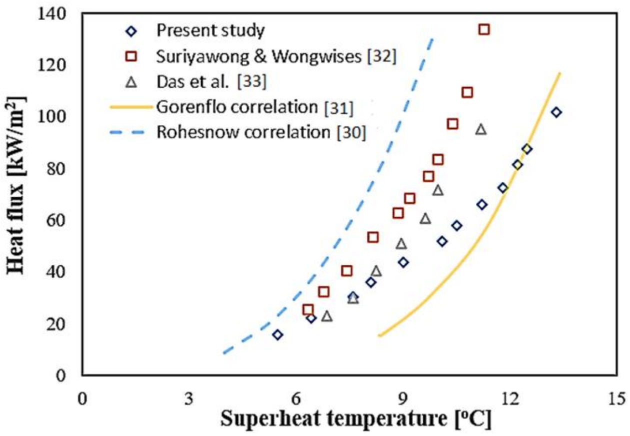

Figure 26. Validation of pool boiling curves of water with Suriyawong and Wongwises [238], *Das et al.* [239], *Gorenflo et al.* [237], *and Rohesnow et al.* [236].

Figure 27 shows the relationship between heat flux against the superheat temperature, which is the difference between the wall temperature and the saturation temperature of the fluid heated by that wall (ΔTsup = Tw − Tsat). This figure is defined as the pool boiling curve for the BF and halloysite nanofluids. Because of the power restriction of the cartridge heater utilized in this study, the maximum applied heat flux employed for all experiments did not exceed 118 kW/m^2, which indicated that all experiments were performed below the critical heat flux value. As the applied heat flux was raised, the superheat temperature rose slightly for both the halloysite nanofluid and water because of the nucleate mechanism of pool boiling. Moreover, it could be noticed that at the 0.05 % volume fraction, the curve moved to the left side of the graph as compared to water at heat flux values ranging from 36.3 to 58.8 kW/m^2 with superheat temperatures values 7.6 to 9.6 K. At 0.1 % fraction curve, there was a very slight enhancement, as it could be seen from the minor left shift of the curve at heat flux values from 30 to 60.3 kW/m^2 with superheat temperatures values 7.4 to 10.5 K. However, increasing the fraction of the nanofluid significantly changed the boiling curve toward the right. Exceptionally, at high heat flux values, the shift was remarkable. Moreover, as the process was running forward, heat flux and superheat temperature kept rising, and at the same time, the pool's boiling performance worsened. This might be linked to the nanoflakes accumulating on the surface of the heating tube under the boiling phase. The result was that the thermal insulation layer which was formed prevented the heat transfer between the heating tube and the working fluids. This explanation was used by several researchers [157], [238], [239].

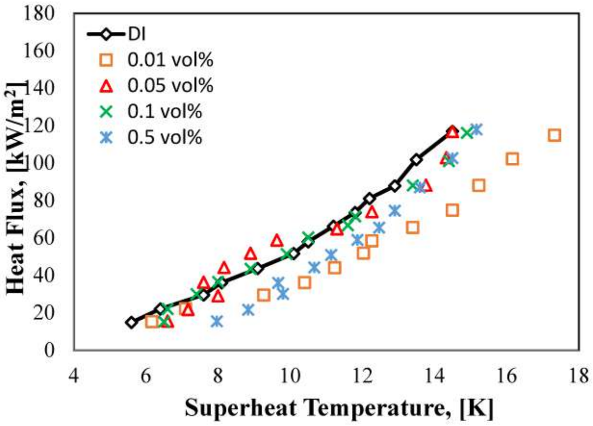

Figure 27. Pool boiling curves of water and halloysite nanofluids at different volume fractions.

Figure 28 shows the proportional relationship between the a heat flux and PBHTC. From the graph, it could be seen that there was an improvement in the PBHTC for the volume fractions of (0.1 % and 0.05 %). The 0.1 % curve had a better PBHTC than water starting from heat flux of 30 kW/m^2 with PBHTC of 4.05 kW/m^{2}K and reaching the maximum PBHTC of 5.74 kW/m^{2}K at the heat flux of 60.3 kW/m^2. While the 0.05 % curve had the best heat transfer process among all the other fractions, as it increased by moving to the left side of the graph when the heat flux value reached 36.27 kW/m^2 with 4.77 kW/m^{2}K of PBHTC and continued rising until the highest value of the PBHTC at 6.10 kW/m^{2}K with 58.8 kW/m^2 heat flux. However, after reaching the peak, the curves for both the above-mentioned fractions started to deteriorate as the boiling process moved forward with time. The reason behind this was related to the good thermal conductivity of the halloysite nanofluid.

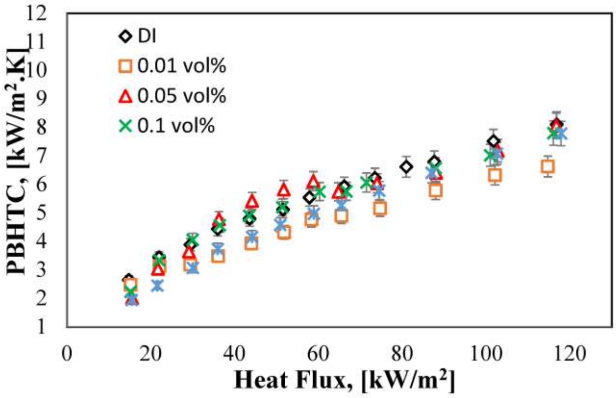

Figure 28. PBHTC against the applied heat fluxes for water and halloysite nanofluid of four-volume fractions.

Figure 29 shows the graph between the applied heat flux and the ratio of PBHTC of halloysite nanofluid with respect to water ($PBHTC_{nf}/PBHTC_{water}$) for four volume fractions. It could be clearly seen that the ratio of 0.05 % halloysite nanofluid had the best enhancement of 13.8 % at moderate heat flux (51.74 kW/m^2). Moreover, there was another improved ratio (about 4.6 %) for the 0.1 % volume fraction at low heat flux (30 kW/m^2). Furthermore, the behavior of the PBHTC of the nanofluid at moderate and low heat was discovered to be superior to that of water, particularly when it came to volume fractions (0.05 % and 0.01 %), and that was because the bulk effect prevails in the free convection area.

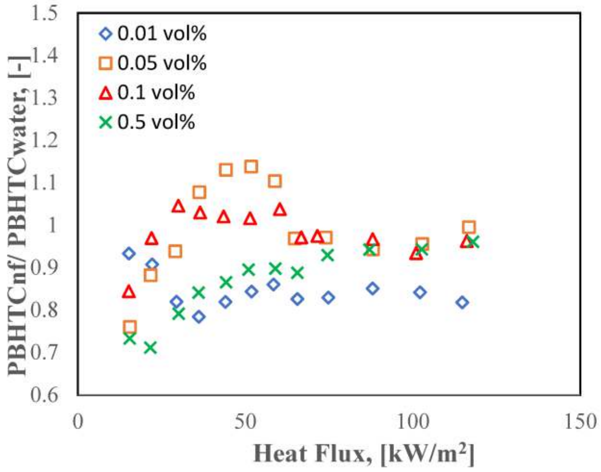

Figure 29. PBHTC ratio of halloysite nanofluid and water at different volume fractions and applied heat fluxes.

Another notable piece of information from Figure 29 is that at heat flux > 60 kW/m^2 for most fractions, the PBHT ratio decreased. The reason for this deterioration was the deposition of the solid material (dry powder nanoparticle) on the heating element surface, where the cavities were filled with the nanotubes of the halloysite, which deactivated the nucleation sites, as could be seen from Figure 25 at the DOM pictures. Kim et al. [240] explained the deposition of the suspended solid material on the external surface of the heater inside the chamber by showing that this deposition formed an insulation layer (nano-porous) and hindered the heat transfer process, which resulted in making the heating tube hydrophilic. Because of the cohesion of the nano-powder to the heating surface, it was postulated in this research that the accumulation of nanotubes negatively alters the surface properties.

4.3. SiO_2-TiO_2 nanofluids

According to the specifications described by the manufacturer, the sizes of SiO_2 and TiO_2 nanoparticles were 10-20 nm and 21 nm, respectively. SiO_2 and TiO_2 (1:1 volume ratio) were dispersed into a mixture of EG and water (5:1 volume ratio).

Figure 30 shows the XRD pattern of SiO_2 and TiO_2. For the XRD pattern of SiO_2 (Figure 30a), the broad diffraction peak confirmed a completely amorphous structure. Except for a broad band centered at $2\theta = 22.5°$, no diffraction peak was observed [47]. It also revealed no impurity peaks for SiO_2 nanoparticles. Based on the XRD patterns of TiO_2 (Figure 30b), TiO_2 consisted of rutile and anatase phases. The anatase form was the main component with peaks at 2θ values of 25.4°, 37.9°, 48.1°, 54°, 55.1° and 62.8°. The rutile phase was an adjunct at 2θ values of 27.6°, 36.2°, 41.4° and 54.4° [48]. There were not any reflections corresponding to any impurity phases, so the high purity of the TiO_2 sample was indicated. The TiO_2 used in this analysis contains a significant anatase component, which is expected to result in improved thermal conductivity. This is because anatase can enhance the thermal conductivity of nanofluids more effectively than rutile, due to its more efficient phonon transport and reduced scattering [241].

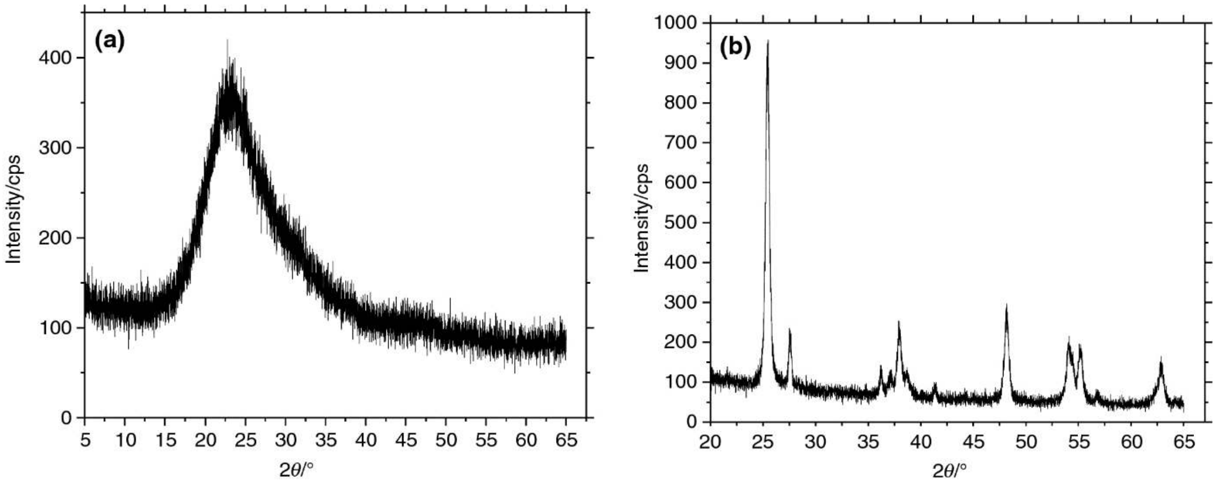

*Figure 30. XRD pattern of (**a**) SiO_2, (**b**) TiO_2*

Figure 31 and Figure 32 show the SEM and TEM images of the morphological structure of nano-SiO_2. It could be observed that nano-SiO_2 had a size of ca. 15 nm in accordance with the manufacturer's specifications. The SEM image of nano-TiO_2 is shown in Figure 33. It could be found that the particle size was 23 nm.

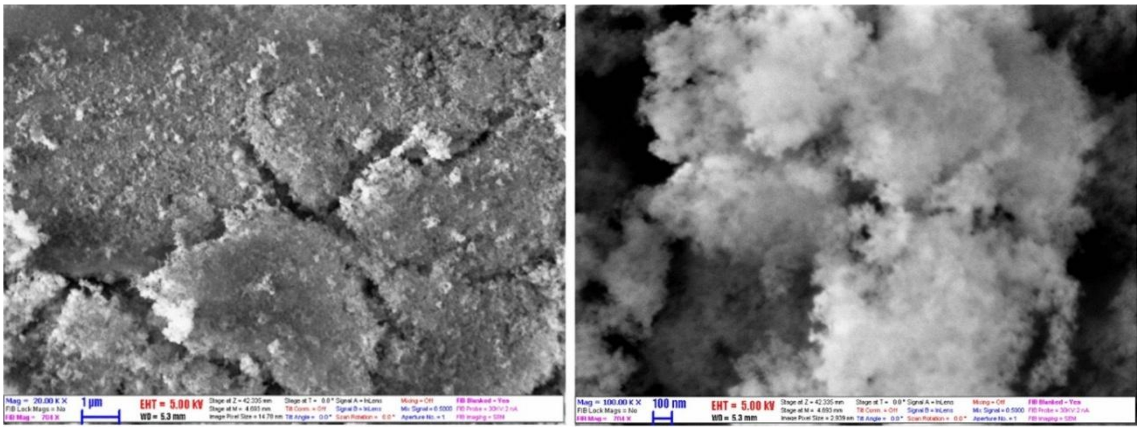

Figure 31. SEM images of SiO_2 nanoparticles with magnification ×20000 (left) and ×100000 (right)

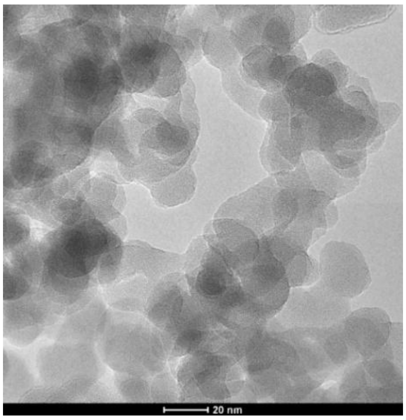

Figure 32. TEM images of SiO_2 nanoparticles [242]

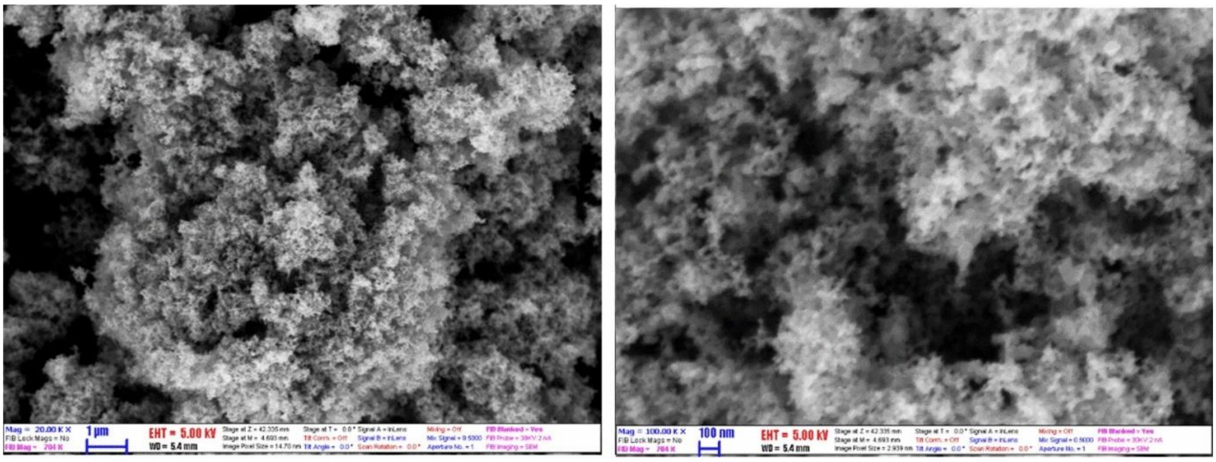

Figure 33. SEM images of TiO_2 nanoparticles with magnification ×20000 (left) and ×100000 (right).

The FTIR spectrum of TiO_2 nanoparticles is shown in Figure 34a. The broadband centered at around 600 cm^{-1} was assigned to the bending vibration (Ti–O-Ti) bonds in the TiO_2 lattice. The broadband centered at around 3420 cm^{-1} was attributed to the intermolecular interaction of the hydroxyl group (–OH) with the H_2O molecule absorbed on the TiO_2 surface. The peak at around 1650 cm^{-1} confirmed the typical bending vibration of the –OH group [243]. Figure 34b shows the FTIR spectrum of SiO_2 nanoparticles. The peaks around 3420 cm^{-1} and 1630 cm^{-1} could be ascribed to the –OH stretching and bending vibrations of absorbed water molecules on the SiO_2 nanoparticles, respectively. The peaks at 1101 and 475 cm^{-1} referred to the Si–O-Si asymmetric stretching and bending vibrations, similar to the peak of halloysite. The peaks at 961 cm^{-1} and 801 cm^{-1} were attributed to the Si–O-(H-H_2O) stretching vibrations and the symmetric vibrations of Si-O-Si, respectively [244]. The FTIR spectra of the TiO_2 and SiO_2 nanoparticles showed clear, well-defined peaks with no signs of impurities, indicating high purity of the nanoparticles. The presence of functional groups suggests that these nanoparticles are likely compatible with polar solvents, such as a water and EG mixture, which could promote stable dispersion in such BFs.

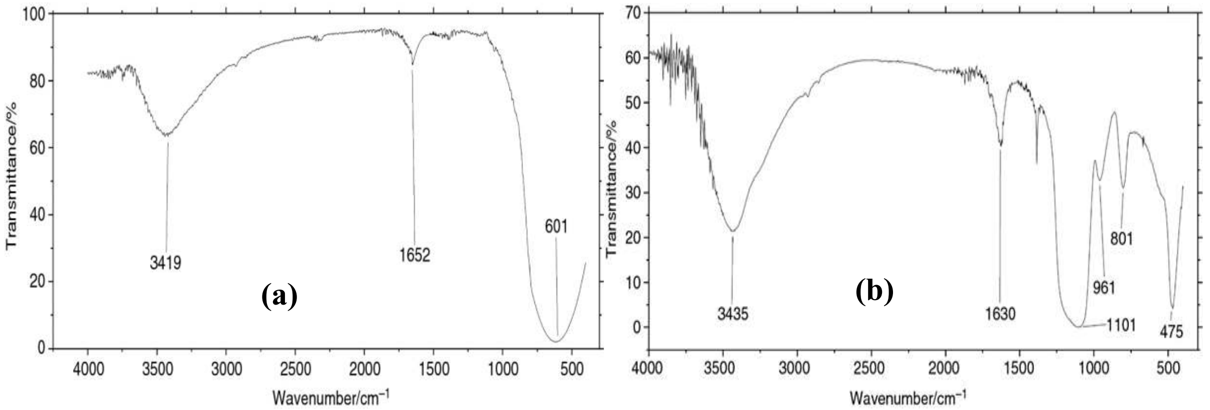

Figure 34. FTIR spectrum of nanoparticles: (a) TiO_2 (b) SiO_2

Table 16 contains the EDX results of TiO_2 and SiO_2 nanoparticles (Appendix C). The results were the average values of five measurement points in the atomic percentage. These results confirmed the chemical composition of the used nanoparticles.

Table 16. EDX results of TiO_2 and SiO_2 nanoparticles

SiO_2/atom%		**TiO_2/atom%**	
Si	**O**	**Ti**	**O**
33.68	66.32	30.57	69.43

For improving the stability of SiO_2–TiO_2 hybrid nanofluids, different stabilizing agents were used, such as CTAB, SDBS, SCMC, and TX. Table 17 shows the ZP of 0.5 % SiO_2–TiO_2 hybrid nanofluids with different stabilizing agents. Among the used stabilizing agents, the CTAB gave the best result with − 19.1 mV. According to the ZP values, the SiO_2–TiO_2 hybrid nanofluids had the best stability without any stabilizing agents. The visual observation gave the same result.

Table 17 ZP of 0.5 % SiO_2–TiO_2 nanofluids with different stabilizing agents

Stabilizing agents	Without stabilizing agents	CTAB	SDBS	SCMC	TX
ZP of 0.5 % SiO_2–TiO_2 hybrid nanofluid/mV	− 30.4	− 19.1	− 10.5	− 10.1	− 17.3

Colloidal solutions with ZP's lower than −30 mV have acceptable stability [92]. Table 18 shows ZP values of SiO_2, TiO_2 pure nanofluids, and SiO_2–TiO_2 hybrid nanofluids without stabilizing agent for different volume fractions. The ZP of 0.5, 1.0, and 1.5 % SiO_2–TiO_2 hybrid nanofluids was − 30.4 mV, − 33.0 mV, and − 43.3 mV, respectively. This showed the stability of nanofluids. These ZP values indicated the slower aggregation behavior of SiO_2–TiO_2 nanoparticles by increasing the fractions. It meant that by increasing the fractions of nanofluids, the negative electrical surface charge of SiO_2–TiO_2 increased; thus, the -OH groups were ionized. TiO_2 nanofluids provided good stability with high ZP. ZP results showed that SiO_2

nanofluids had moderate stability. By visual observation, it was confirmed that these nanofluids were stable over 3 days.

Table 18. ZP of SiO_2, TiO_2 nanofluids and SiO_2–TiO_2 hybrid nanofluids for different volume fractions

Nanofluids	SiO_2-TiO_2-0.5	SiO_2-TiO_2-1.0	SiO_2-TiO_2-1.5	SiO_2-0.5	SiO_2-1.0	SiO_2-1.5	TiO_2-0.5	TiO_2-1.0	TiO_2-1.5
ZP, mV	− 30.4	− 33.0	− 43.3	− 23.0	− 24.2	− 25.2	34.5	33.3	30.9

For determining the rheological behaviors of SiO_2–TiO_2 hybrid nanofluids, the viscosities at different shear rates were investigated for three volume fractions of 0.5, 1.0, and 1.5 at five temperatures: 20, 30, 40, 50, and 60 °C as shown in Figure 35. The viscosities of all SiO_2–TiO_2 hybrid nanofluid samples decreased with increasing temperature and increased with increasing fraction of nanofluids.

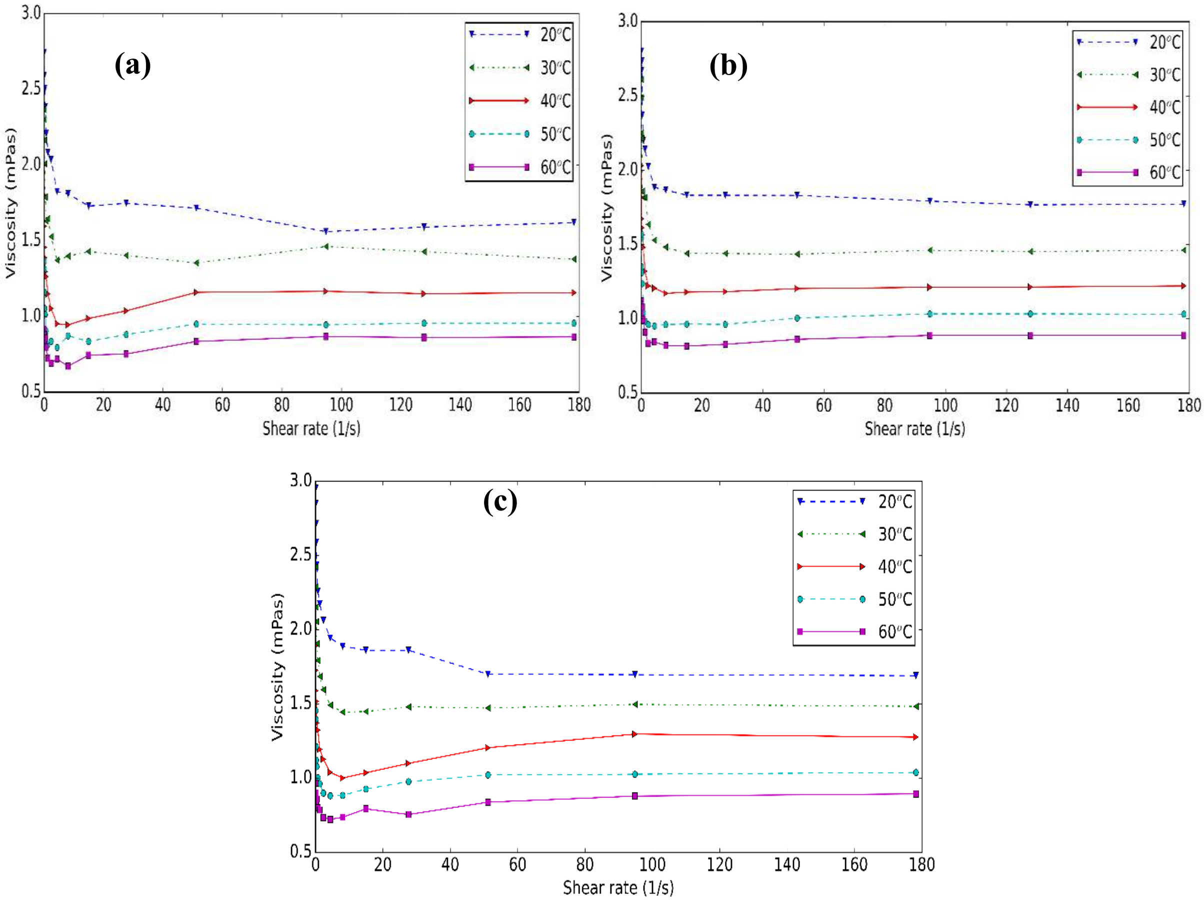

Figure 35. Viscosity–shear rates diagram of SiO_2, (b) TiO_2 and (c) SiO_2–TiO_2 hybrid nanofluids for 0.5 % volume fraction

This reduction behavior of viscosity might be caused because the higher temperature increased the Brownian and thermal motion of molecules and their average velocity, leading to weakened intermolecular interaction and adhesion forces between molecules [166], [245]. For low shear rates (less than 5 s^{-1}), the nanofluid behaved as a non-Newtonian fluid or shear-thinning fluid. It meant the viscosity of all hybrid nanofluids decreased with the increase of the shear rate. In the case of high shear rates, the viscosity of SiO_2–TiO_2 hybrid nanofluids was almost independent of the applied shear rate. This meant that the hybrid nanofluid was Newtonian (see Figure 35). Bahrami et al. [168] and Nabil et al. [15] found that the Fe–CuO nanofluids and TiO_2-SiO_2 nanofluids owned Newtonian rheological behavior for different temperatures and fractions. These results indicated that the properties of nanoparticles and temperature were important factors in the rheological properties of nanofluids. The rheological behavior generally depended on particle size and morphology, nanoparticle fraction, BF, electro-viscous effects, and solution chemistry-related surface layer [246]. Mehrali et al. showed that at low shear rates, the structure of fluid changed temporarily when the spindle rotated in the fluid, and molecules were gradually arranged in the direction of increasing shear, causing less reduction in viscosity. However, when the shear rate is high enough, the fluid undergoes maximum shear ordering, causing larger aggregates to break down into smaller, more dispersed particles. This breakdown reduces the effective size of the particles in suspension, decreasing the internal resistance to flow and thus leading to a lower viscosity [18]. With the presence of nanoparticles in hybrid nanofluids, it could be explained that the viscosity of SiO_2–TiO_2 hybrid nanofluids was higher than the BF.

Figure 36 shows the relative viscosity of SiO_2–TiO_2 hybrid nanofluids. The relative viscosity increased with the increase in the volume fraction, while temperature did not play an important role. The relative viscosity increased from 24 % for a 0.5 % volume fraction of SiO_2–TiO_2 hybrid nanofluids to 58 % for a 1.5 % fraction.

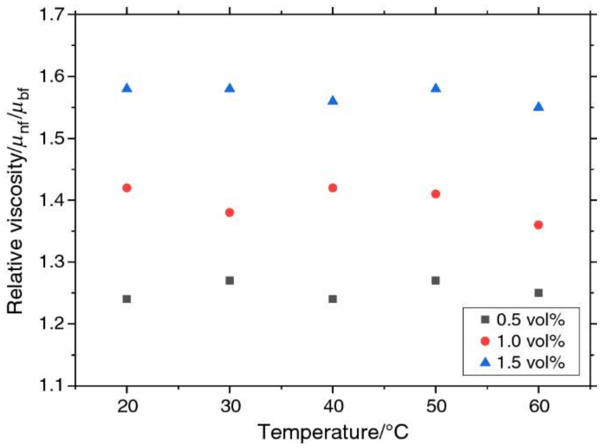

Figure 36. Relative viscosity of SiO_2–TiO_2 hybrid nanofluids at different temperatures

Figure 37 shows a comparison of the relative viscosity between the present work (0.5 %) with the data from Nabil et al. [15]. The results from the present research showed little higher relative viscosity than the literature data between 20 and 60 °C. The SiO_2 nanofluids still had the lowest relative viscosity, while the TiO_2 nanofluids had the highest viscosity. The viscosity strongly depended on nanoparticles, BFs, and fractions.

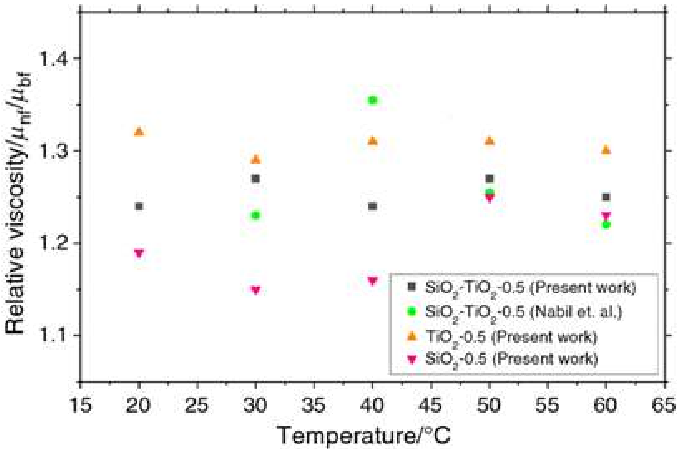

Figure 37. Comparison of the relative viscosity between the present work and the result of Nabil et al. [15]

The thermal conductivity of all SiO_2–TiO_2 hybrid nanofluids at various temperatures is shown in Figure 38. The calibration tests for water were verified before the measurement of samples, and the results were obtained within a 0.5 % error. All SiO_2–TiO_2 hybrid nanofluids showed higher thermal conductivity compared to the water/EG mixture at all temperatures. SiO_2–TiO_2 hybrid nanofluids at 0.5, 1.0, and 1.5 % showed 4.72 %, 7.19 %, and 9.03 % thermal conductivity enhancement compared to the EG/water mixture at 20 °C, respectively. The thermal conductivity of SiO_2–TiO_2 hybrid nanofluids increased with increasing temperature. Nevertheless, the effect of temperature and fraction on the enhancement of thermal conductivity was different. On the one hand, the temperature caused the thermal conductivity of nanofluids to be higher because of the reduction of viscosity and the augmentation in the Brownian motion of nanoparticles [18]. On the other hand, the relationship between thermal conductivity enhancement and a fraction of SiO_2–TiO_2 nanoparticles was not completely linear. This was understandable; as the number of nanoparticles in the solution increased, the thermal conductivity of the solution also increased. In addition to the fraction and temperature, the extent of thermal conductivity enhancement of nanofluids depended on the type of used nanomaterials, pH, stabilizing agents, and the type of BF, which influenced the motion of particles in suspension.

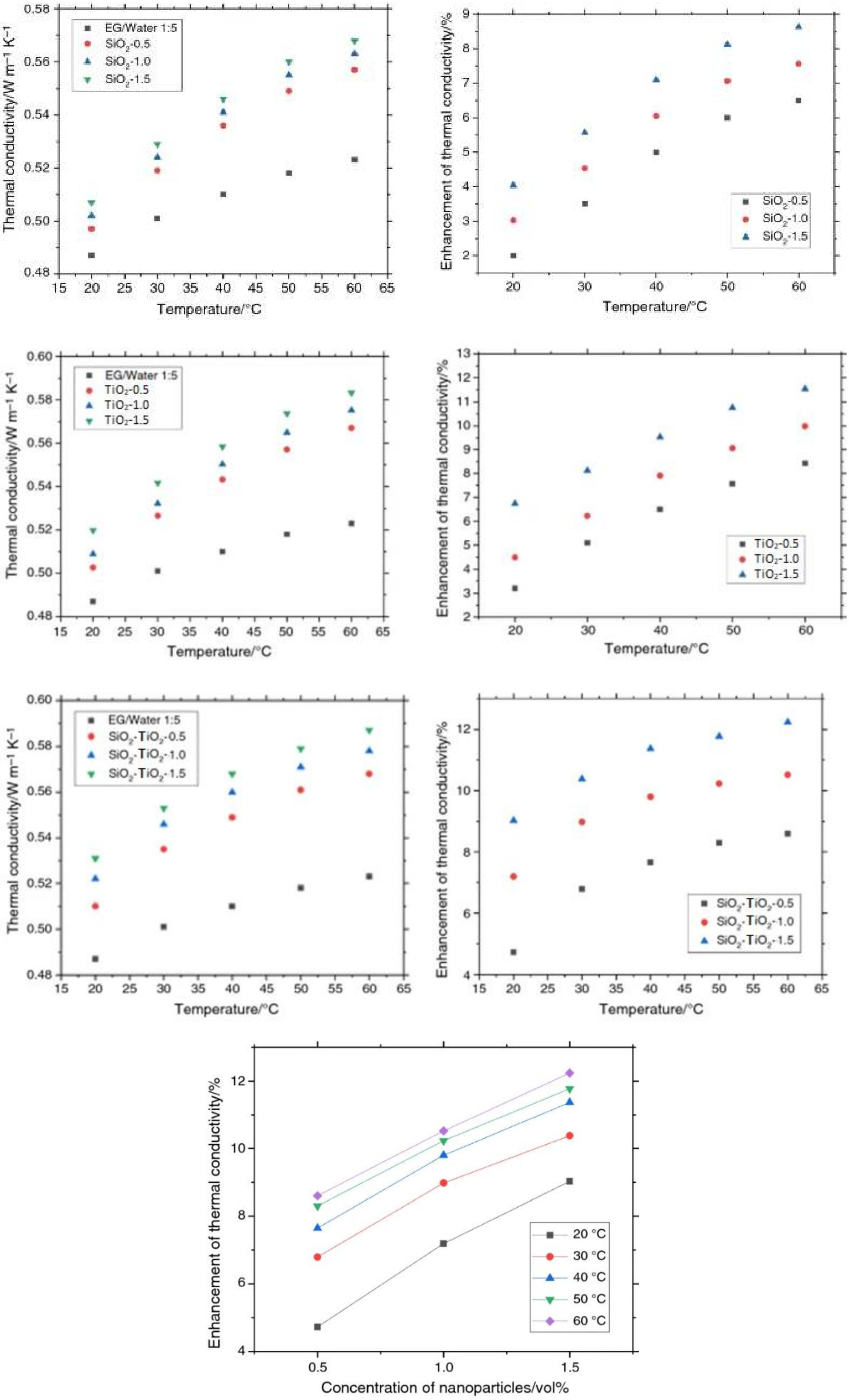

Figure 38. Thermal conductivity and enhancement of thermal conductivity of pure SiO_2, TiO_2 and SiO_2–TiO_2 hybrid nanofluids at different temperatures

Figure 39 shows the enhancement of thermal conductivity obtained from the present work and previous studies. It could be seen that the thermal conductivity of the hybrid nanofluids in the present research was higher than the thermal conductivity of pure SiO_2, TiO_2 nanofluids, and even SiO_2–TiO_2 hybrid nanofluids. This could be explained by the fact that TiO_2 contributed greatly to increasing the thermal conductivity of the hybrid nanofluids due to the size and anatase content of TiO_2 nanoparticles.

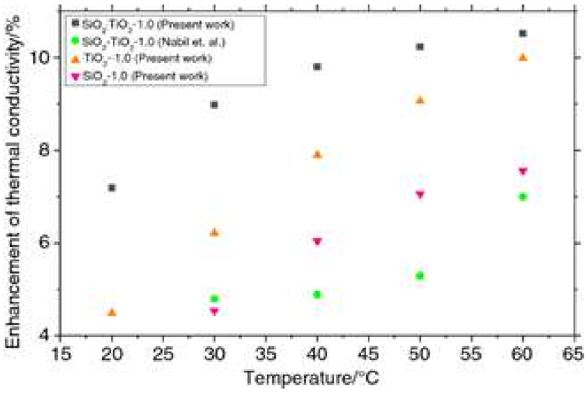

Figure 39. Comparison of the enhancement of thermal conductivity between the present work and the result of Nabil et al. [15]

4.4. CFD study on heat transfer performance

4.4.1. Mesh independency test

To ensure the reliability of the numerical solutions and minimize the effects of mesh changes, a mesh independence study was performed. Six separate mesh configurations were used to evaluate the impact of mesh selection on the simulation results.

The investigated Re range was from 5000 to 17000. The Nu numbers by the ANSYS calculation were determined for the $Re = 5000$ and $Re = 17000$, with the mesh sizes of 7.0×10^5, 8.0×10^5, 9.0×10^5, 1.0×10^6, 1.1×10^6, and 1.2×10^6 unit. Figure 40 shows the calculated ratio (Nu divided by Nu of the highest mesh) variation against the mesh size. I assumed that if mesh independence was proved at the end of the investigated range, the same mesh used was validated inside the Re range.

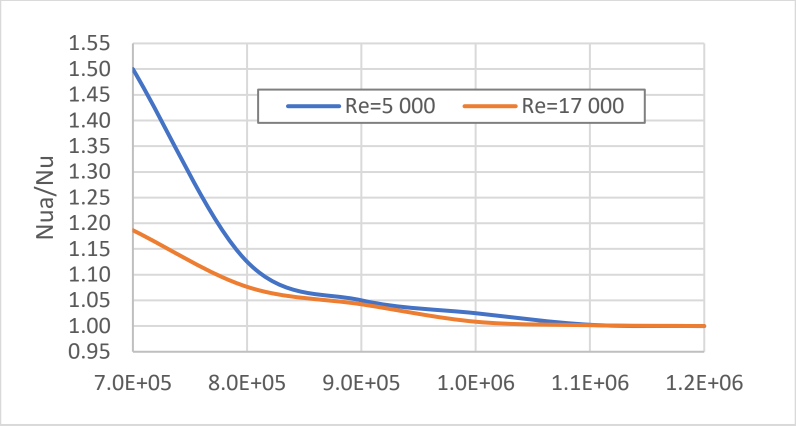

Figure 40. Nu number ratios against the mesh size.

4.4.2. Fully developed flow

In the formulae that account for the fully developed flow heat transfer, the diameter-to-length ratio did not appear, except for in (7) and (13), but (7) was not applicable due to its validity for low Pr numbers. The numerical experiment had to be performed for a long tube to obtain the fully developed flow. The local heat transfer variation was localized for a shorter length in turbulent flow configuration than the laminar flow; for calculating the entry length (L_e), Equation (7) was used from [247]. However, in planning the experiment, the tube should be long enough to neglect that part. Figure 41 represents the local Nu number variation decrease from [198]. According to the investigated nanofluids, the $Pr = 5$ curve was assumed to determine that part of the length where the local Nu number varied. Practically, this means that the investigated zone started at $L = \sim 23 \cdot D = 0.37$ m from the tube entrance, as shown in Table 19, which lists the calculation results based on [247]. It was also worth mentioning that in [248], the proposed equation for hydrodynamic entry length – from the point of entry to the point where the velocity profile is fully developed - was $Le = D \cdot 1.359 \cdot Re^{0.25}$ and in [249], $Le = \sim 10 \cdot D$. The smallest approximation for entry length in [247], [248], [249] offered the largest one. This latter value was accepted.

$$\frac{L_e}{D} = 4.4 \cdot Re^{(1/6)} \tag{7}$$

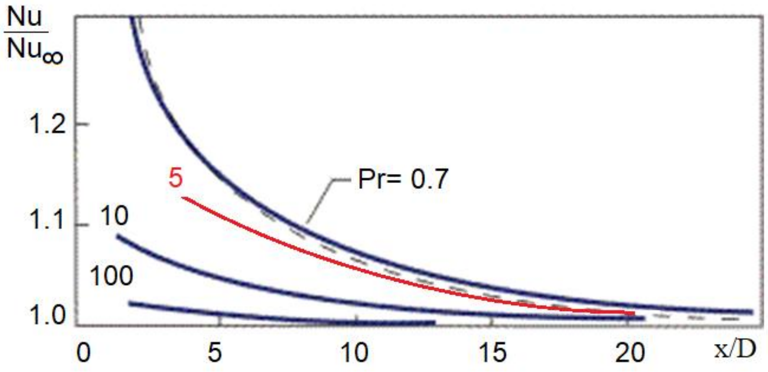

Figure 41. Effect of the Pr number on the development of heat transfer in a tube [198].

Table 19. The entry length variation D = 0.016 m.

R_e	L_e/D, [247]	L_e, m [249]	L_e/D, [248]
5000	18.2	0.29	11.4
8000	19.7	0.31	12.9
11000	20.8	0.33	13.9
14000	21.6	0.35	14.8
17000	22.3	0.36	15.5

4.4.3. Velocity and temperature profiles

The velocity and temperature profiles of the hybrid nanofluids at the fully developed flow regime are represented in Figure 42 as an example for $Re = 10000$. Part (a) shows wall subjects of constant heat flux, while part (b) shows wall subjects of constant temperature. According to sources in the literature, for example [198], in turbulent flow, there were no countable differences between part (a) and part (b) regarding the velocity profiles, but the temperature values were different; meanwhile, the shapes of the temperature profiles were also very similar.

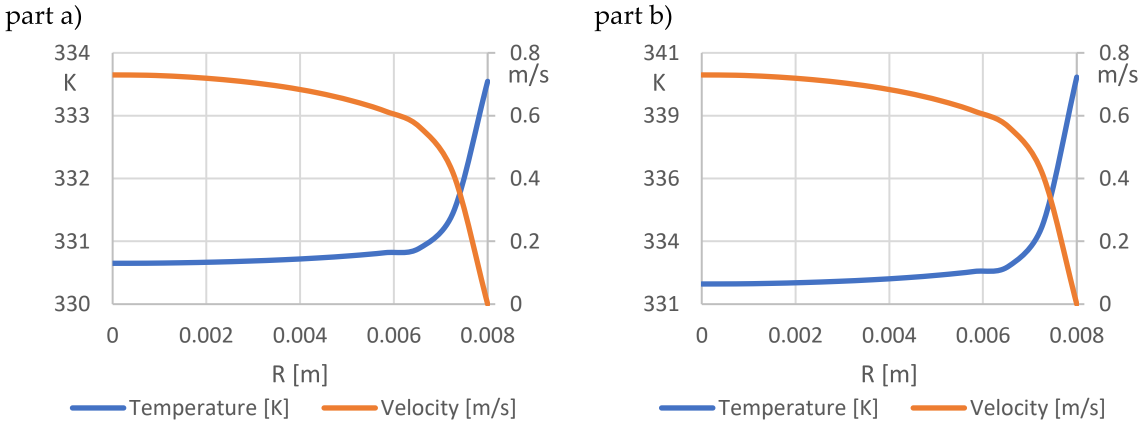

Figure 42. Velocity and temperature profiles in fully developed flow (a) constant heat flux (b) constant temperature of the wall.

4.4.4. Simulation results

The results were valid according to the limitations of the previous sections' reports. Here, it was mentioned that the developing flow was not included in the results, compared with the correlations, because most are valid only for infinite-length tubes.

Constant heat flux with Non-Variable Properties, Developed Flow:

Figure 43a represents the numerical simulation results for a constant wall heat flux of $Re =$ 5000-17000. In agreement with sources in the literature, the hybrid nanofluid of 1.5 % volume fraction had the highest Nu numbers.

Constant Wall Temperature with Non-Variable Properties and Developed Flow:

Figure 43b represents the numerical simulation results for a constant wall temperature of $Re = 5000 - 17000$. In line with sources in the literature, the hybrid nanofluid of 1.5 % volume fraction had the highest Nu numbers.

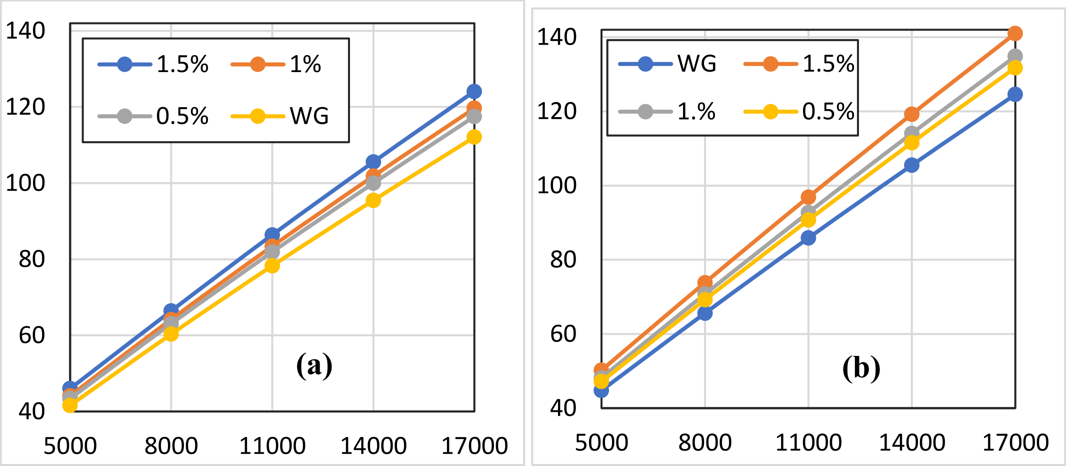

Figure 43. Nusselt numbers against Reynolds numbers for (a) constant heat flux (b) constant wall temperature.

Figure 44 introduces the comparison of the constant wall temperature and heat flux for (a) $Re = 5000$ and (b) $Re = 17000$. It shows the Nusselt numbers calculated by (1) Dittus–Boelter (DB), (6) Sieder–Tate (ST), (8) von Kármán (vonK), and (13) Gnielinski (Gn) correlations. The $\mathrm{T}_{\mathrm{wall}}$ curve represents Nu numbers for a constant wall temperature, and heat flux represents Nu numbers for a constant wall heat flux arrangement. The ST and DB correlations do not contain the friction factor, while the vonK and Gn include the friction factor. Since the tendencies are the same for all Re numbers in the investigated range, only the $Re =$ 5000 and $Re = 17000$ results are shown. The major observation can be summarized as follows:

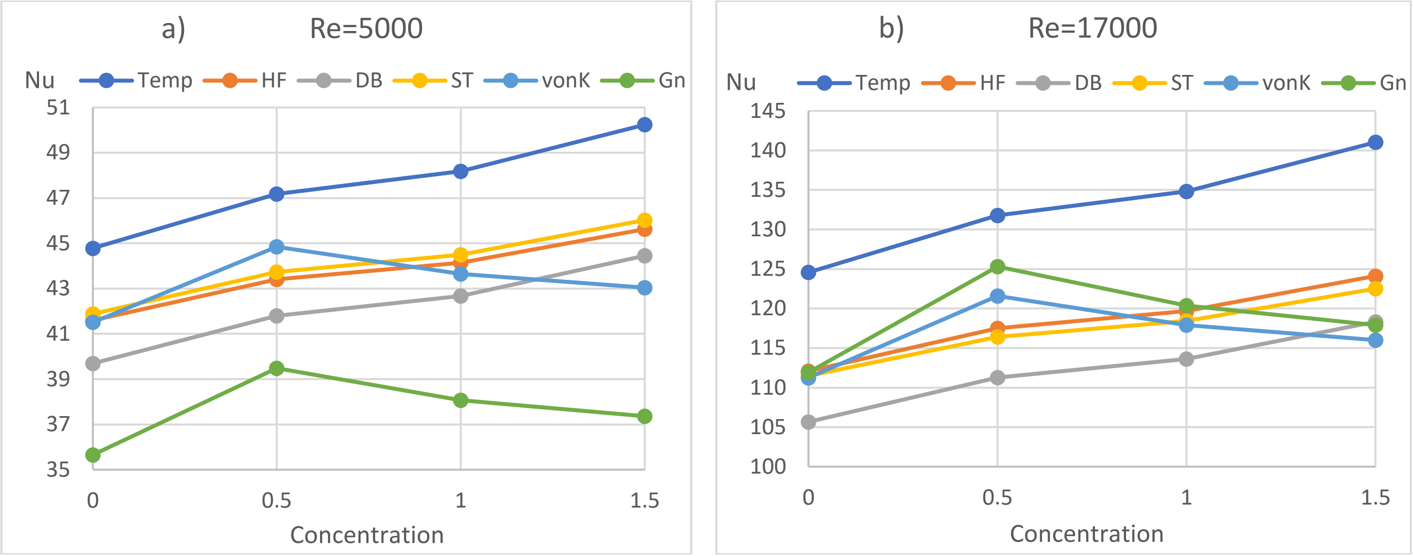

Figure 44. Comparison of the simulation results and correlations with (a) Re = 5000 (b) Re = 17000.

- The Nu numbers in the case of constant wall temperature were 7–10 % higher than in the case of the constant heat flux, and the difference increased as the Re number increased. The difference between constant heat flux and constant wall temperature was considered small in the literature, for example, in [198], but due to the greater temperature difference alongside the tube length, the heat transfer was more intensive in the case of constant wall temperature. Moreover, the observed differences in the context of the accuracy of heat transfer measurements were satisfactory;
- The DB correlation underestimated Nu numbers, while the ST correlation gave practically the same Nu numbers for constant heat flux;
- The ST correlation values were less than the numerical simulation result up to Re = 14000 and were above the simulation result only at $Re = 17000$. It should also be mentioned that the ST correlation by [198] was valid only to $Re = 10000$, but according to our results, it could be used at least to $Re = 17000$;
- The correlation that contained the friction factor performed better at higher Re numbers. It should be mentioned that the application range for vonK started from $Re = 10000$, and for Gn, from $Re = 2300$, but vonK performed well below $Re = 10000$ as well.

<u>*Constant heat flux with Variable Properties:*</u>

The properties of the fluids varied by temperature, but when the difference between the mean fluid temperature and the tube wall temperature was not high, the differences that the variations of the properties such as thermal conductivity and viscosity may cause are nearly negligible. Table 20 illustrates the calculation results with CFD simulations using constant and variable properties. By considering the variable properties, the Nu number was generally higher by 1 % in the investigated cases.

Table 20. Nu numbers for constant and variable properties of constant heat flux.

	0.5 %		**1 %**		**1.5 %**	
Re	**Const.**	**Variable**	**Const.**	**Variable**	**Const.**	**Variable**
5000	43.4	43.7	44.1	44.5	45.6	45.5
8000	63.1	64.2	64.2	65.3	66.4	66.9
11000	81.9	83.3	83.4	84.8	86.4	86.9
14000	100.0	101.5	101.8	103.4	105.5	105.9
17000	117.5	119.0	119.7	121.2	124.1	124.2

Constant Wall Temperature with Variable Properties:

Table 21 illustrates the calculation results with constant and variable property CFD simulations. By considering the variable properties, the Nu number was generally higher by 2 % in the cases investigated. The higher differences were due to the higher differences between the wall and mean fluid temperatures.

Table 21. Nu numbers for constant and variable properties for constant wall temperature.

	0.5 %		**1 %**		**1.5 %**	
Re	**Const.**	**Variable**	**Const.**	**Variable**	**Const.**	**Variable**
5000	47.2	47.2	48.2	48.6	50.2	50.0
8000	69.2	70.1	70.7	72.6	73.8	74.8
11000	90.7	91.6	92.7	95.2	96.9	98.3
14000	111.6	112.1	114.1	117.0	119.3	120.8
17000	131.8	132.0	134.8	138.1	141.0	142.7

HT in Flow Development:

Comparing the constant heat flux and constant wall temperature, one might find only limited differences according to the practical approach, as reported in [249]. Figure 45 shows the relative local Nusselt number variations (Nu/Nu_{∞}) at constant heat flux for Re = 5000 and Re = 17000 for a 1.5 % volume fraction. These results were in agreement with those shown in Figure 42 and Figure 43, based on [249]. The decrease in the Nu number was instant, and the development of the flow ended around $Le = 10 \cdot D$ when the Re number was above 10^4, but for smaller Re numbers, the flow development occurred at a somewhat greater distance. The use of short tubes was advised in the practical engineering application, considering flow development. A more intensive heat transfer would occur than expected in the case of constant wall temperature. Generally, this was not considered a problem and could be ignored.

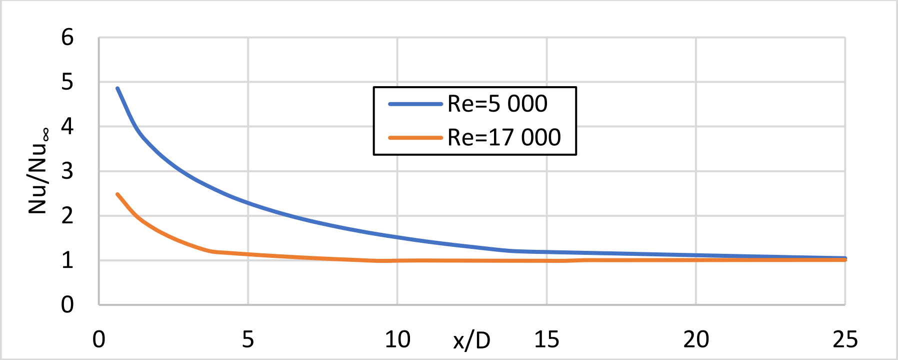

Figure 45. Local Nu number variation for 1.5 % nanofluid.

As previously mentioned, the friction factor has a significant role in determining the pumping power of the working fluids, and its value also appears in correlations for calculating the HTC. Several formulae were worked out to find the implicit Prandtl–Kármán–Nikuradse correlation (Appendix E). Table 22 shows all friction factor results I made using the formulae in Table 3 and the CFD calculation PDs in different cases.

Table 22. The friction factors by different correlations and the CFD simulation

Case identification		No.	Friction factors	
			Re = 5000	**Re = 17000**
Numbers of Table 3 correlations	1	1	0.0376	0.0277
	2	2	0.0375	0.0272
	3	3	0.0384	0.0277
	4	4	0.0375	0.0272
	5	5	0.0378	0.0272
	6	6	0.0379	0.0269
	7	7	0.0386	0.0272
	8	8	0.0373	0.0270
Constant heat flux non-variable properties	0 %	9	0.0367	0.0279
	0.5 %	10	0.0370	0.0279
	1 %	11	0.0370	0.0279
	1.5 %	12	0.0370	0.0279
Constant wall temperature non-variable properties	0 %	13	0.0370	0.0279
	0.5 %	14	0.0370	0.0279
	1 %	15	0.0370	0.0279
	1.5 %	16	0.0370	0.0279
Constant heat flux variable properties	0 %	17	0.0372	0.0280
	0.5 %	18	0.0373	0.0280
	1 %	19	0.0374	0.0280
	1.5%	20	0.0368	0.0280
Constant wall temperature variable properties	0 %	21	0.0370	0.0280
	0.5 %	22	0.0368	0.0280
	1 %	23	0.0369	0.0280
	1.5 %	24	0.0363	0.0277

The friction factor is more general than the PD; Figure 46 shows the PD of hybrid nanofluids obtained from simulation for non-variable properties. The results presented that the

PD increased with higher Re numbers. If one substitutes the $\xi(Re)$ friction factor function into the PD calculation formula, the result is as follows:

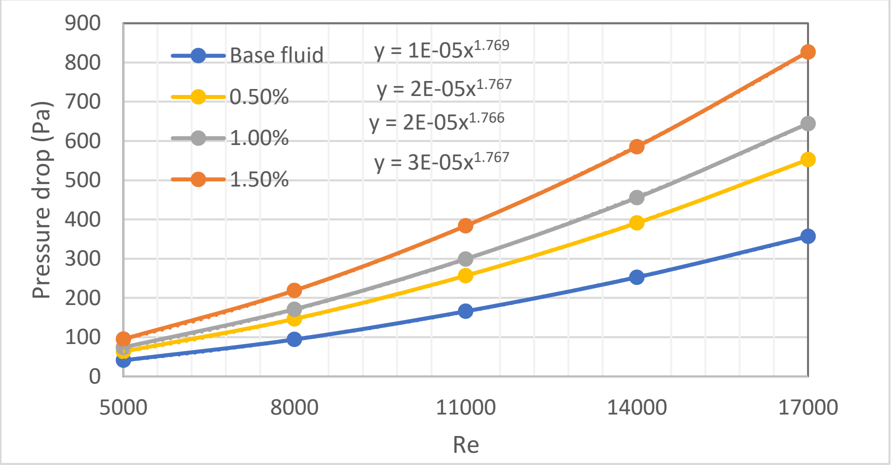

Figure 46. PDs for SiO_2-TiO_2 hybrid nanofluids by CFD calculation.

$$\Delta p = \frac{L}{d}\frac{1}{d^2}\frac{\rho}{2}\left(\frac{\mu}{\rho}\right)^2 Re^2 \xi(Re) \tag{8}$$

where L: length of pipe, d: pipe diameter, ρ: fluid density, μ: fluid viscosity, the $\xi(Re)$ is considered as CRe^m where C is constant, according to our results, and the exponent parameter of the trendlines was 1.76, then $m = 1.76 - 2 = -0.24$, which was close to the Blasius correlation exponent (−0.25), as shown in Table 3.

The PDs relatively increased by 56 % and 137 % at 0.5 and 1.5 %, respectively, because of the rise in viscosity.

4.5. Characterization of carbon nanoparticle nanofluids

The XRD patterns of CNS and CNP are shown in Figure 47. The structure of CNS was amorphous, indicated by the single broad diffraction peak centered at 20°. For CNP, it could be seen that there were two broad peaks at 2θ = 25° and 2θ = 43.8°. The diffraction peaks corresponded to the (002) and (101) planes of graphite because of the higher degree of graphitization [250]. Identifying the structural characteristics through XRD is essential for understanding their impact on the thermal properties of the nanofluids. The amorphous structure of CNS, as indicated by the broad peak, suggests increased phonon scattering, which may reduce thermal conductivity. In contrast, the higher degree of graphitization in CNP, as evidenced by the distinct peaks, implies a more ordered structure that can enhance thermal conductivity [251].

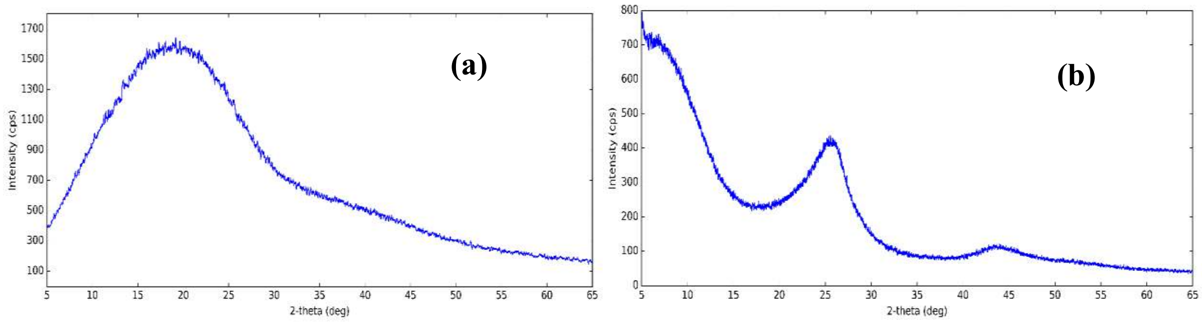

Figure 47. XRD pattern of (a) CNS and (b) CNP

Figure 48 shows the SEM photographs of CNS (a, b) and CNP (c, d). From the figure, it could be seen that the CNS had uniformed well-shaped spheres with smooth surfaces, while the CNP particles were irregular. By measuring the diameter at five points of the SEM images, the average diameter of the particles was obtained. The diameter of CNS and CNP was 500 and 60 nm, respectively. The size of the CNP was in agreement with the data given by the manufacturer (<100 nm). The smaller size of CNP compared to the size of CNS indicated that CNP nanofluids might have higher thermal conductivity. The particles of both types tended to aggregate. However, CNP particles aggregated more than CNS. This may be attributed to stronger attractive forces in CNP than in CNS, which made the CNP nanofluid challenging to stabilize [92].

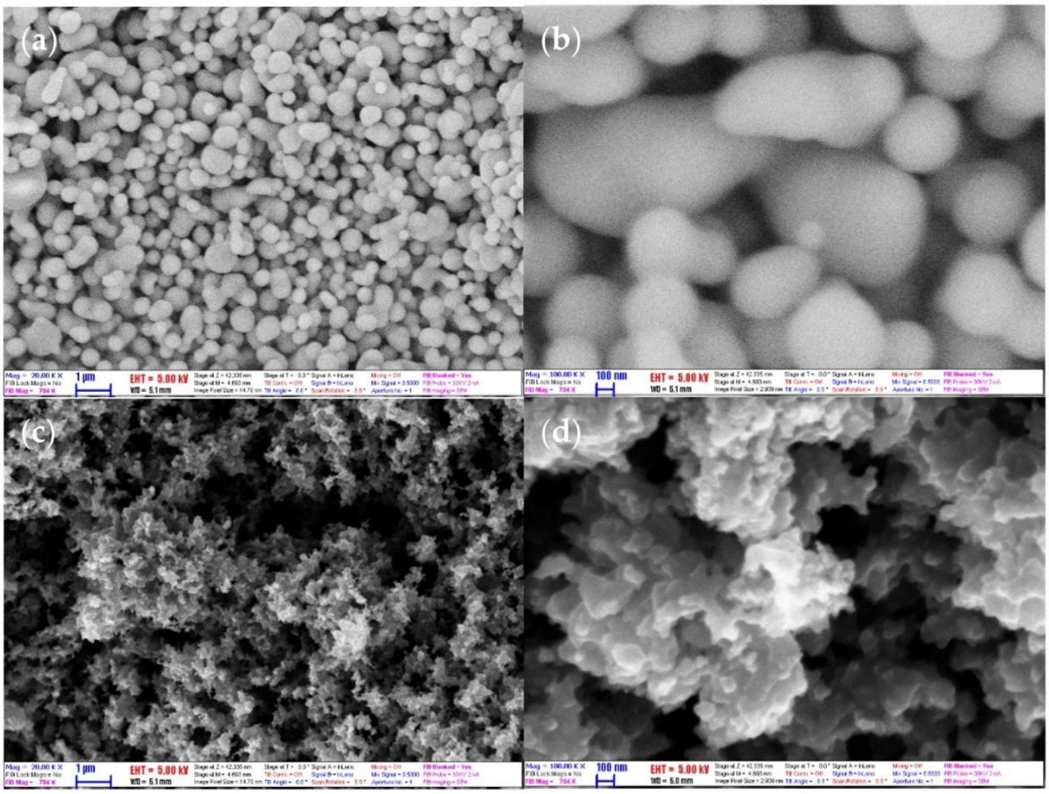

Figure 48. SEM images of (a,b) CNS and (c,d) CNP with magnification ×20000 and ×100000

The nanoparticle shape strongly affects the transport processes in nanofluids [252]. Therefore, the thermal conductivity and viscosity do not depend only on the volume fraction of the nanoparticle but, to another extent, on the particle shape. As the molecular level interactions take place at the particle surface, the particle shape impacts the thermal and momentum transfers. The particle shape influences the particle-particle interaction (e.g., collision) and the particle–fluid interaction (e.g., liquid layering) as well. These complex static and dynamic processes result in differences in augmentation, in the role of radiation of the heat transfer, and in the liquid layering.

There are some oxygen-containing groups on the carbon nanoparticles. These groups are left over in the nanoparticle manufacturing process. In order to investigate the effect of the functional groups of the CNS and CNP to select the type of solvents and stabilizing agents, FTIR analysis was performed. The FTIR spectra of the nanoparticles are shown in Figure 49. For both types of nanoparticles, the vibration of –OH groups was at 3425 cm^{-1}. At 1614 cm^{-1} and 1618 cm^{-1}, the characteristic peaks of the C=C double bonds were observed. The peaks at around 754, 796, and 840 cm^{-1} were caused by the hydrogen wagging of carbon rings [253]. For the CNS, the band at 2930 cm^{-1} referred to the vibration of C–H bonds [250]. The peak at 1700 cm^{-1} and 1026 cm^{-1} was assigned to the –OH and C–O bonds, respectively [254]. For the CNP, the fingerprint bands at 616 and 473 cm^{-1} presented the aromatic structure with mono-substitution [255]. Due to these properties, CNS nanofluids can be more effectively stabilized with polar solvents like water and ethanol, whereas CNP may require the presence of a stabilizing agent to achieve better dispersion.

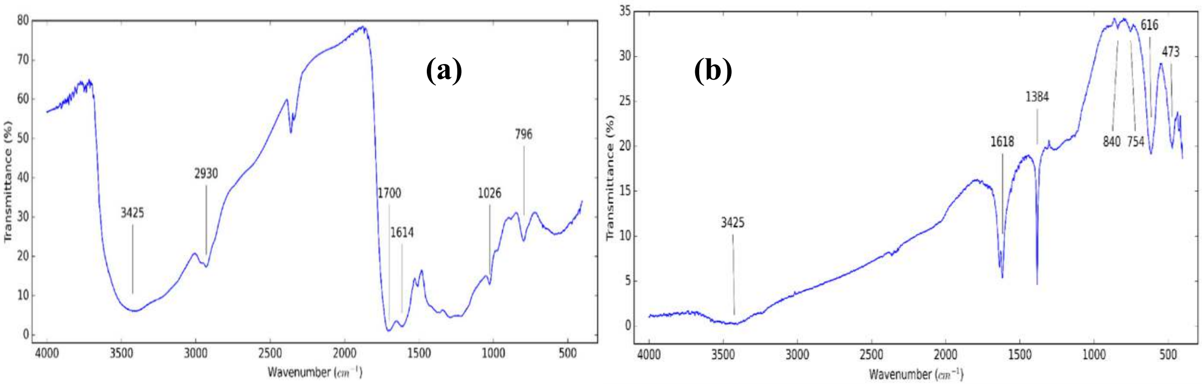

Figure 49. FTIR spectrum of (a) CNS and (b) CNP dry particles.

The chemical composition of the CNS and CNP was obtained by EDX. The main elements, including C and O (H cannot be observed) from EDX and XPS measurements and specific surface area (S_{BET}), are presented in Table 23. The table presents the average of the atomic percentage at five measurement points. The atomic percent of the oxygen content in the CNP was lower than in the CNS. The CNP had 91.6 atomic percent of carbon from EDX analysis. The S_{BET} of CNP was more than 10 times higher than that of CNS.

Table 23. S_{BET}, XPS, and EDX results of CNS and CNP dry particles.

Nanoparticles	**S_{BET}/(m^2/g)**	**Atom% (XPS)**		**Atom% (EDX)**	
		C	**O**	**C**	**O**
CNS	9	76.9	23.1	81.4	18.6
CNP	106	90.7	9.3	91.6	8.4

Figure 50 presents the TGA/DTG/DTA curves of the CNS and CNP samples in air (Appendix D). For the CNS, two stages of weight loss were observed. The first one referred to the removal of the absorbed water, the dehydration of the functional groups, and the densification of the surface layer of the CNS to 245 °C, and the weight loss was around 6.3 %. The next decomposition step could be attributed to the oxidation of the carbonaceous nanomaterials to 470 °C, and in this step, an abrupt change was observed [255]. For the CNP, the first stage lasted to 425 °C, and the weight loss was 3.9 %; then, the oxidizing process proceeded to 700 °C [256]. The oxidation happened with CNP at a higher temperature compared to CNS. This indicated that the thermal stability of CNP was higher than that of CNS. This was similar to the case of reduced graphene oxide and graphene oxide. [257]. The remaining ash from the oxidization was 0.5 % and 5.5 % for the CNS and CNP, respectively. The reason can be related to the content of the residual catalyst. CNS was obtained from sucrose without catalysts, while in CNP, there were remaining catalysts such as transition-metal oxide frequently used.

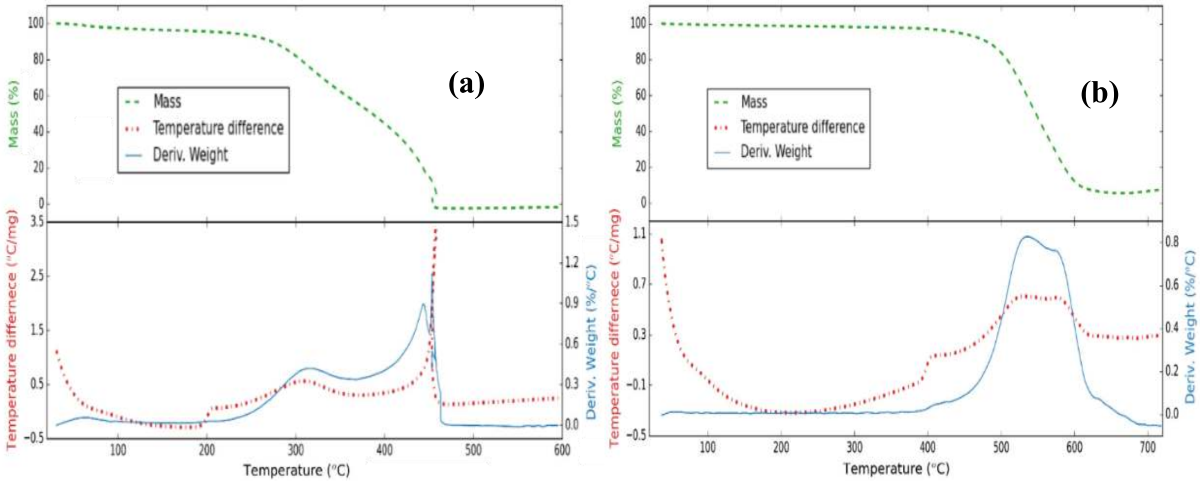

Figure 50. Thermal analysis curve for (a) CNS and (b) CNP with a heating rate of 10 °C/min in airflow (Exothermic direction is up on DTA curves).

XPS spectrum and the deconvolution of the carbon 1s of CNS and CNP are shown in Figure 51 and Figure 52. From the figures, the carbon 1s contained five components: sp^2, sp^3, C–O, C=O, and O–C=O/loss feature observed at 284.3, 285.3, 286.8, 288.3, and 290.7 eV, respectively [258]. At 290.7 eV, the peak could be the mixture of the plasmonic loss feature and carbon peak. Table 24 shows the concentration of chemical bonds from XPS measurements (Appendix F). The percentage of O–H in CNS was greater than in CNP. Also, the percentage of C–O and C=O of CNS was higher than that of CNP, corroborating thermal analysis results. This was also consistent with the results of S_{BET}. With a greater carbon/oxygen ratio, the S_{BET} values of particles were higher due to the effects of functional groups [259].

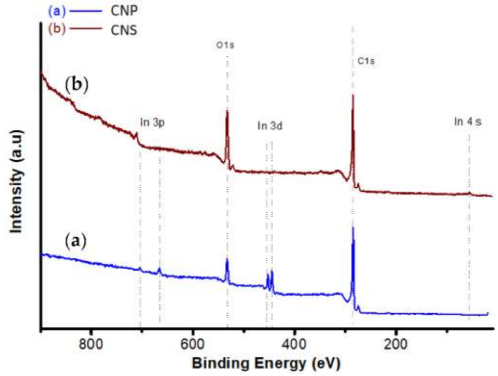

Figure 51. XPS analysis for (a) CNP and (b) CNS with 40 eV pass energy and 0.3 s dwell time.

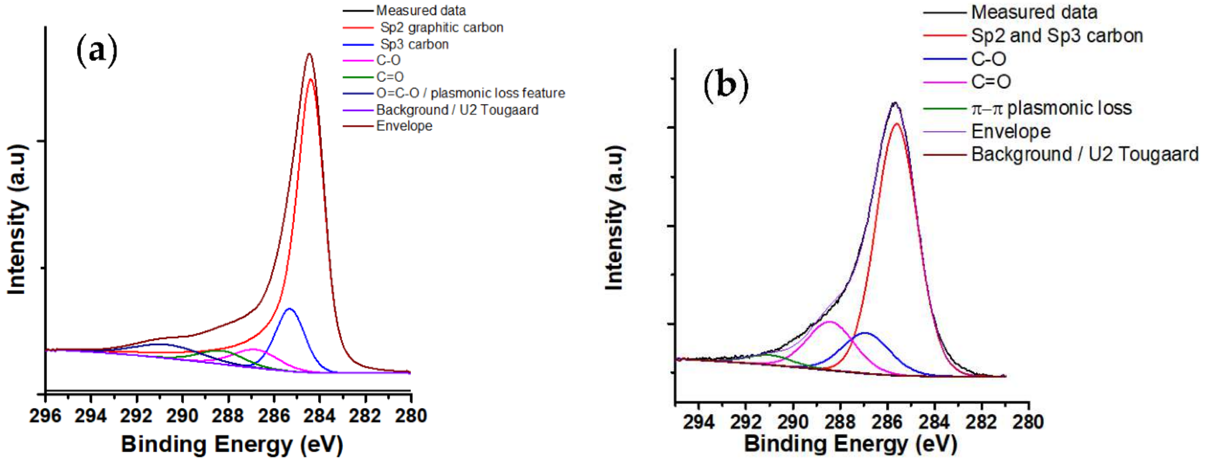

Figure 52. C 1s XPS spectrum of (a) CNP and (b) CNS.

Table 24. Concentration of chemical bonds on the surface of CNS and CNP from XPS.

Nanoparticles	**C 1s (%)**					**O 1s (%)**	
	sp^3	**sp^2**	**C-O**	**C=O**	**O-C=O**	**C=O**	**O-H**
CNP	72.1	12.3	5.5	4.0	6.1	35.4	64.6
CNS	69.3		12.6	15.0	3.1	8.2	91.8

UV-Vis measurement was used to determine the stability of nanofluids. The maximum absorbance was read with a wavelength, then the absorbance at that wavelength was recorded after each time interval. The maximum absorbance of CNS and CNP nanofluids over days is shown in Figure 53. It was obvious that the prepared nanofluids were stable for 4 days.

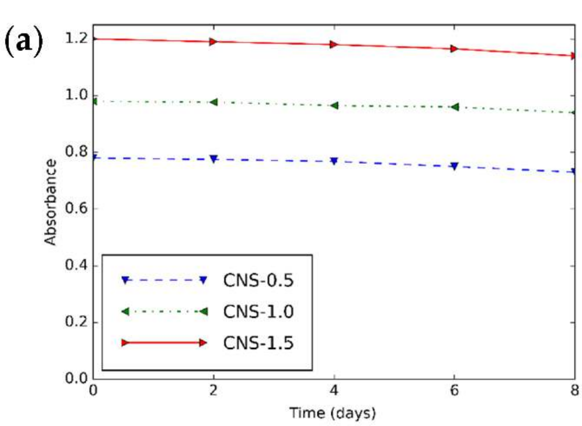

Figure 53. Maximum absorbance-time diagram of (a) CNS at 303 nm and (b) CNP nanofluids at 300 nm for different fractions.

One of the most important factors determining the quality of the heat transfer fluid is viscosity because the increase in viscosity causes higher pumping energy. Similar to other fluids, temperature affects the viscosity of the nanofluids. The viscometer was calibrated with water, and the measured value closely matched the theoretical result. The viscosity measurements were performed on BF, CNS, and CNP nanofluids for three volume fractions of 0.5, 1.0, and 1.5 % at different temperatures. Figure 54 presents the viscosity of 0.5 % CNS and CNP nanofluids as a function of shear rate at different temperatures. The increasing temperature made the shear stress of the nanofluids lower due to the Brownian motion, while the fraction of CNS and CNP increased the shear stress [71,72]. The nanofluids were Newtonian because the chart line can be considered linear.

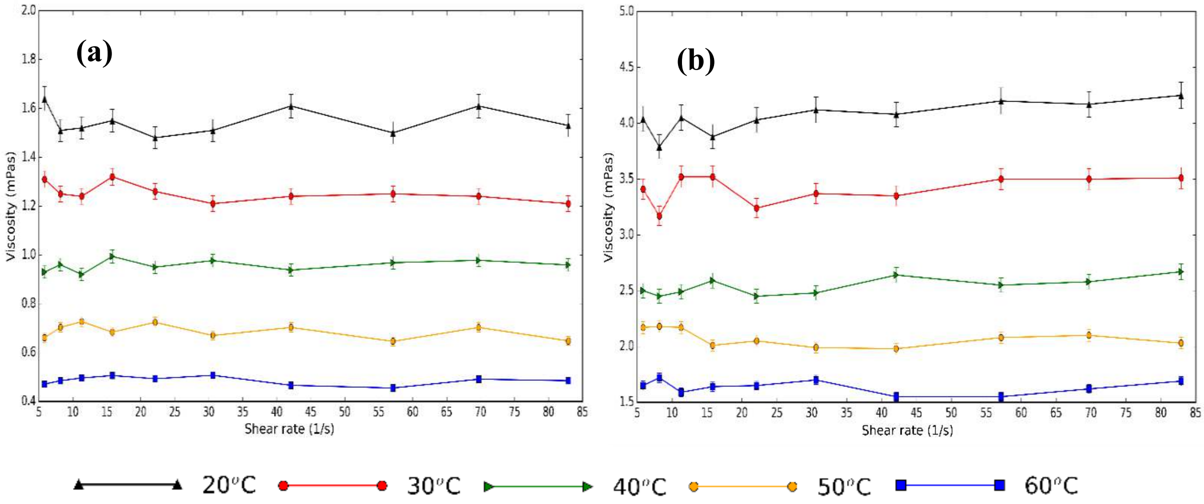

Figure 54. Viscosity-shear rates diagram of (a) CNS and (b) CNP nanofluids for 0.5 % at different temperatures.

The surface to volume ratio was significantly higher (see Figure 48 and Table 23) for CNP compared to the CNS. Forming nanofluid with the same fraction results in more particle–fluid interaction resulting in higher shear stresses and higher viscosity.

The relative viscosity of CNS and CNP nanofluids, which is the ratio of the viscosity of nanofluids and BF, is shown in Figure 55 from 20 to 60 °C. The BF in the case of CNP also contained a stabilizing agent to study the effect of the nanoparticles on the increase in viscosity. The nanoparticle content increased viscosity. This was probably due to the formed clusters. With temperature, the viscosity of nanofluids increased faster than that of the BF. Similar relative viscosities were obtained for both particles. However, the viscosity of CNP nanofluid (at 0.5 % at 20 °C, 3.911 mPas) was much higher than that of the CNS nanofluids (1.545 mPas) due to the usage of stabilizing agent in CNP nanofluid [260]. The viscosity increment is the ratio of the difference between the viscosities of the nanofluid and solvent to the viscosity of the solvent. The viscosity increment of CNS nanofluid was between 3.11 % and 9.31 %, while this range of the CNP nanofluids was 5.31 % and 9.56 %.

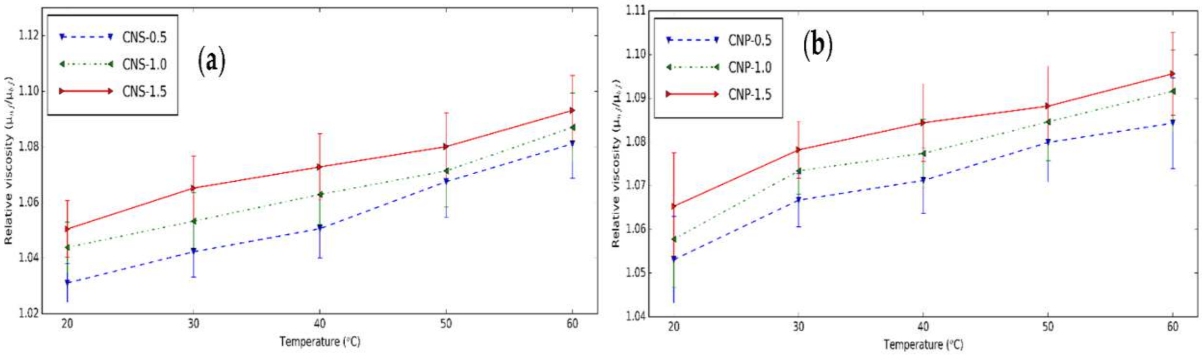

Figure 55. Relative viscosity–temperature diagram of (a) CNS and (b) CNP nanofluids for different fractions at different temperatures.

The relative viscosity obtained in the current study was collated with the values published in the previous investigations to confirm the results (see Table 25).

Table 25 Correlation for relative viscosity from previous studies

Reference	Correlation for relative viscosity
Wang et al. [261]	$1 + 7.3\phi + 123\phi^2$
Hatscheck et al. [262]	$1+4.5\phi$

The collation was performed with different fractions and at 20 °C. Figure 56 shows the comparison between the present study and the previous results. This study has a result similar to the predicted values from Hatscheck et al. [262] and Wang et al. [261] at 0.5 %, while at higher fractions, the Wang formula overestimated the prepared nanofluid viscosities.

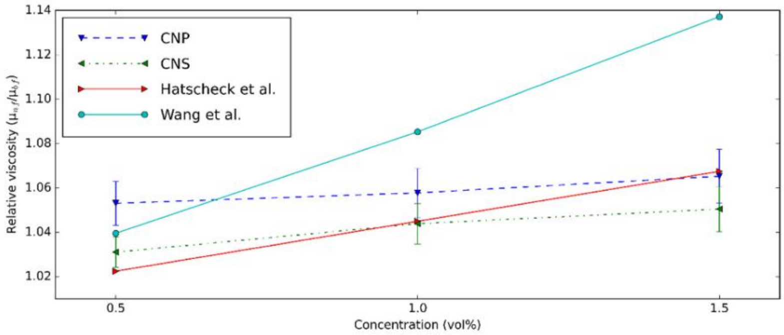

Figure 56. Comparison of the relative viscosity data obtained in this study with the results of Hatscheck et al. [262] *and Wang et al.* [261] *at 20 °C and different fractions.*

The thermal conductivity and its increment of CNS and CNP nanofluids are shown in Figure 57 and Figure 58 at different temperatures. The nanofluids had higher thermal conductivity than the BFs at experimental temperatures. The thermal conductivity of the nanofluids increased with increasing temperature because of the Brownian movement of nanoparticles. At 0.5 %, from 20 to 60 °C, thermal conductivity increased from 0.534 to 0.582 W/(mK) or 8.99 % increment for CNS and from 0.575 to 0.692 W/(mK) or 20.35 % for CNP. The higher number of nanoparticles dispersed in the nanofluids made thermal conductivity greater. At 30 °C, from 0.5 % to 1.5 %, thermal conductivity increased by 0.55 % for CNS and 6.38 % for CNP nanofluids. In literature, from the results of Mirsaeidi et al. [263], the carbon quantum dot (4.5 nm)/water-EG nanofluids had thermal conductivity of 0.261 and 0.27 W/(mK), the thermal conductivity enhancement of 3.6 % and 7.1 % for 0.4 and 1 %. Brzóska et al. [264] showed that the thermal conductivity increments of MWCNT (60-80 nm)/EG nanofluids were 15.4 % and 29.3 % for 0.5 and 1 %. Compared to the carbon quantum dot nanofluids, the CNP nanofluids had a similar result, while the CNS nanofluids had lower thermal conductivity enhancement.

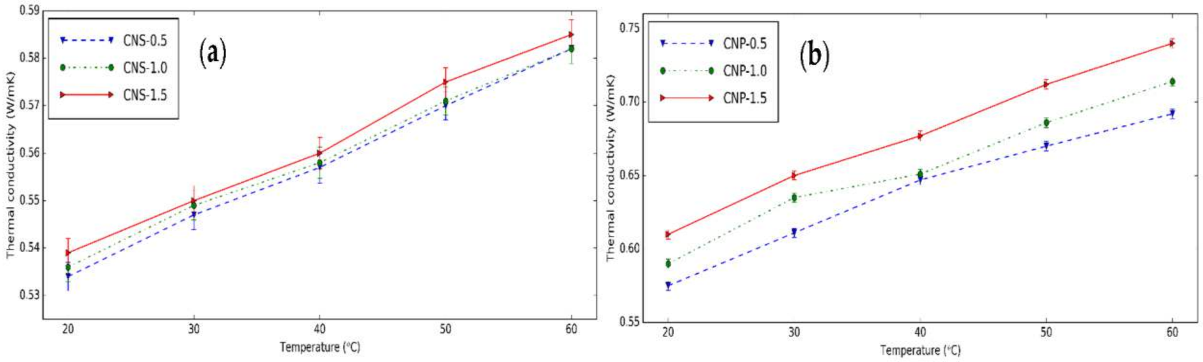

Figure 57. Thermal conductivity of (a) CNS and (b) CNP nanofluids with different fractions at different temperatures.

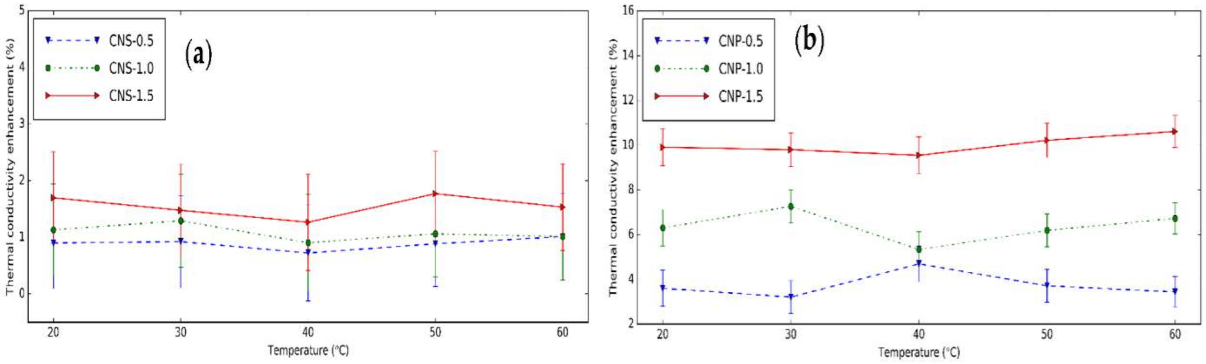

Figure 58. Thermal conductivity enhancement of (a) CNS and (b) CNP nanofluids with different fractions at different temperatures.

The thermal conductivity enhancement of CNP nanofluids was greater than that of the CNS nanofluids. This occurred due to the smaller sizes and higher crystallinity of the CNP nanoparticle. Moreover, based on the XPS analysis, CNP had a higher carbon/oxygen ratio, which improved the thermal conductivity of the CNP nanofluids [259]. It was concluded that although the CNP nanofluids were difficult to stabilize, these nanofluids had better thermal conductivity. The CNS with smaller size improved more thermal conductivity for the nanofluids based on them [263]. These results are lower than the thermal conductivity enhancement of MWCNT nanofluids [264]. This can be explained by the long shape of MWCNT.

The comparison of thermal conductivity enhancement between this study and the previous research is shown in Figure 59. Clearly, the results estimated from Pak's model [265] match with CNP nanofluids, while the Maxwell model [266] was suitable for the CNS nanofluids. In literature, these models have been used as references for solid and liquid solutions.

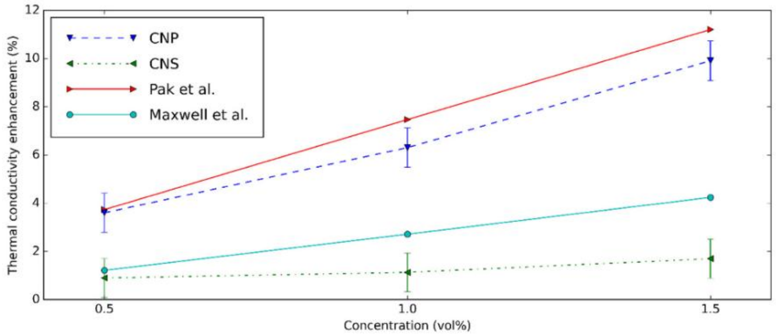

Figure 59. Thermal conductivity enhancement comparison between the present study and the result of Maxwell et al. [266] *and Pak et al.* [265].

5. Conclusion

In my PhD work, I investigated the thermophysical properties (i) and PBHT (ii) of the halloysite nanofluids, the thermophysical properties (iii) and the heat transfer performance in CFD (iv) of SiO_2-TiO_2 hybrid nanofluid, and the comparison of the thermophysical properties of the carbon nanomaterial nanofluids (v). This research has addressed significant gaps in the existing literature, particularly concerning the fundamental behavior and potential applications of these largely unexplored nanofluid types. My studies have successfully synthesized and characterized these novel stable nanofluids, investigated their thermophysical properties, and performed both experimental and numerical experiments in various heat transfer applications.

For halloysite nanofluids, stability can be successfully achieved under high pH conditions or through the use of stabilizing agents, as confirmed by ZP measurements and visual observations indicating strong dispersion. A key advantage of HNTs is their natural abundance, which makes them a potentially more cost-effective and environmentally friendly alternative to synthetic nanomaterials. Their unique tubular morphology characterized by an average diameter of approximately 58 nm and a length of approximately 436 nm plays a critical role in performance. This structure enables the formation of efficient heat transfer pathways within the fluid, resulting in a thermal conductivity enhancement of up to 18.30 % at a volume fraction of 1.5 %. Additionally, halloysite nanofluids exhibit Newtonian rheological behavior, which is advantageous for maintaining stable flow in heat transfer applications. However, a notable limitation is the requirement for a high pH (pH = 12) to achieve stabilization without additives, which may limit applicability in pH-sensitive systems. The presence of quartz impurities, while not detrimental in this study, may also warrant consideration in applications demanding high material purity.

Further investigation into HNT behavior during PBHT revealed that the physical deposition of nanoparticles on the heater surface significantly modifies surface wettability and nucleation site density. These changes lead to enhanced HTC and reduced superheating temperatures, even at very low volume fractions (0.05 % and 0.1 %), underscoring the critical role of nanoparticle–surface interactions in improving boiling heat transfer performance.

Comprehensive investigations of novel SiO_2–TiO_2 hybrid nanofluids demonstrated significant potential by combining the complementary properties of amorphous SiO_2 nanoparticles (15 nm) and crystalline TiO_2 nanoparticles (10–20 nm, predominantly in the rutile and anatase phases). The primary advantage of these hybrid systems is their enhanced thermal conductivity, which reaches 12.24 % at a volumetric concentration of 1.5 %, substantially surpassing the performance of nanofluids containing only SiO_2 or TiO_2. This improvement indicates a strong synergistic effect, whereby the distinct characteristics of each nanoparticle type contribute to a more efficient heat transfer mechanism. The stability of the hybrid nanofluids has been clearly verified through ZP measurements, while the use of a water–EG mixture as the BF extends their applicability across a broader operating temperature range. Nevertheless, a notable limitation is the significant increase in viscosity, up to 24 % at a volumetric concentration of 0.5 %, relative to the BF, which may necessitate higher pumping power in practical applications. From a fundamental standpoint, the interactions among differing particle sizes, morphologies, and crystal structures of SiO_2 and TiO_2 are likely to form a more complex and optimized phonon conduction network within the fluid. This synergistic behavior underscores the capability of hybrid nanofluids to finely tune and enhance thermophysical properties beyond the limits of single-component nanofluids, highlighting their promise for advanced heat transfer fluid design.

In this study, the heat transfer performance of SiO_2–TiO_2 nanofluids in a circular tube was analyzed using CFD under conditions of constant heat flux and constant wall temperature. The analysis provided a thorough examination of turbulent heat transfer, addressing several commonly overlooked yet crucial details of the phenomenon. The following conclusions were drawn: First, while most simplifications made in the context of turbulent flow were reasonable, it is important to acknowledge the limits of these simplifications. Second, when real-world conditions deviated from the simplified assumptions, a more complex treatment of the phenomenon was necessary. Third, for moderate temperature differences, assuming constant properties yielded results similar to those obtained with temperature-dependent properties, with the added benefit of reduced computational costs. Fourth, both the Nusselt number and PD increased with higher concentrations of hybrid nanofluids and increased flow rates, consistent with previous experimental and theoretical studies. Finally, the simulated results were in good agreement with prior research, validating the reliability of the computational model used in this study.

A comparative study of carbon nanofluids, consisting of CNS (500 nm) synthesized from sugar via a hydrothermal method and CNP (60 nm) sourced from a supplier, offers valuable insights into the effect of carbon morphology on nanofluid performance. The carbon nanospheres are amorphous, while the carbon nanopowder exhibits a higher degree of graphitization. Nanofluids containing CNP demonstrated notably better thermal conductivity enhancement, reaching up to 10.61 % at a volumetric concentration of 1.5 %, making them promising candidates for heat transfer applications. Both types of carbon nanofluids exhibited desirable Newtonian flow behavior and maintained reasonable stability for at least four days at higher volumetric concentrations. However, CNS showed limited improvement in thermal conductivity, which restricts their effectiveness for heat transfer purposes in this context. Moreover, although T80 effectively stabilized the CNP nanofluids, it caused a substantial increase in viscosity, presenting a trade-off between stability and flow characteristics. Further analysis revealed that the irregular morphology and larger specific surface area of the CNP, compared to the more uniform but larger spherical carbon nanoparticles, play a critical role in its superior thermal performance. Additionally, the higher thermal stability of the CNP underscores its suitability for high-temperature applications. This comparative analysis emphasizes that while the uniformity of spherical nanoparticles offers certain advantages, the complex structural and surface characteristics of nanopowder are essential for optimizing heat transfer properties.

In conclusion, this study advances both the fundamental understanding and practical application of novel nanofluids. By preparing, characterizing, and validating their enhanced thermophysical and heat transfer properties, it provides key data addressing gaps in the literature. The results highlight strong potential for practical use in electronic device cooling, solar thermal energy systems, and advanced engine cooling, where efficient heat dissipation is essential. Future research should focus on confirming the long-term stability, reusability, and cost-effectiveness of these nanofluids in real-world systems, exploring the performance of various hybrid nanofluid formulations, and rigorously evaluating potential fouling or corrosion effects to facilitate their broader application in energy-efficient technologies.

6. Thesis points

The publications belonging to each thesis points are found in chapter 7.

(1) Halloysite nanotube/water nanofluids were successfully prepared through a new stabilization method using sodium carboxymethylcellulose (SCMC), specifically compared with those stabilized at pH = 12. These nanofluids were analyzed over a range of temperatures (20-60 °C) and volume fractions (0.5 %, 1.0 %, and 1.5 %). The study revealed that the thermal conductivity of the nanofluids containing SCMC was enhanced by 18.3 %, while the pH = 12 nanofluids showed a 12.7 % increase at 1.5 % volume fraction and 60 °C. This confirms that SCMC is a viable and improved alternative for preparing halloysite nanofluids. [P1]

(2) The impact of halloysite nanotube/water nanofluids with pH = 12 on pool boiling heat transfer was explored, showing significant improvements. For dilute volume fractions of 0.05 % and 0.1 %, the nanofluids reduced superheat temperatures and increased the pool boiling heat transfer coefficient, resulting in a leftward shift of the boiling curve. Notably, a 0.05 % volume fraction achieved a 13.8 % enhancement at moderate heat flux (51.74 kW/m^2). [P2]

(3) SiO_2-TiO_2 hybrid nanofluids synthesized using a water-ethylene glycol mixture (5:1 ratio) as the base fluid, without stabilizing agents demonstrated superior thermal conductivity compared to single nanofluids. The hybrid nanofluids exhibited up to 12.2 % improvement in thermal conductivity at a 1.5 % volume fraction and 60 °C, outperforming the individual pure SiO_2 (8.6 %) and TiO_2 (11.5 %) nanofluids at 1.5 % volume fraction. Additionally, the viscosity of the hybrid nanofluids was found to increase by 24 % at a 0.5 % volume fraction and 20 ºC. [P3]

(4) Through computational fluid dynamics analysis of SiO_2-P25 TiO_2 hybrid nanofluids in a water-ethylene glycol mixture (5:1 ratio), a crucial insight for efficient modelling and design has been established. Under a constant heat flux of 7955 W/m^2 and a wall temperature of 67 °C, the study rigorously demonstrated that for Reynolds numbers below 11000, the study found that a constant property model closely matched results from a temperature-dependent model, showing a maximum deviation of approximately 1-2 % in Nusselt number predictions, thereby presenting a computationally efficient alternative. Furthermore, increasing volume fractions directly correlated with enhanced Nusselt numbers (e.g., up to 12.7 % higher for 1.5 % volume fraction compared to 0.5 % at Re=17000 under constant heat flux) and significantly increased pressure drops (e.g., 56 % at 0.5 % and 137 % at 1.5 % volume fraction due to increased viscosity). This work validates the robustness of simplified turbulent flow assumptions and provides quantitative metrics for practical applications. [P4]

(5) Comparative research on the thermophysical properties of stable nanofluids using carbon nanospheres (500 nm) and carbon nanopowders (60 nm) was successfully conducted, revealing distinct performance characteristics. Prepared in ethanol (carbon nanosphere) and in ethylene glycol with Tween 80 as a surfactant (carbon nanopowder), the carbon nanopowder nanofluids exhibited an 11 % increase in thermal conductivity at a 1.5 % volume fraction and 60 °C compared to the base fluid. In contrast, the carbon nanosphere nanofluids achieved only a 2 % enhancement in thermal conductivity at a 1.5 % volume fraction and 50 °C. [P5]

7. List of publications

Total impact factor: 53.395

Total independent citation: 296

- **Journal publications related to thesis**

[P1] **T. Le Ba**, A.Q. Alkurdi, I.E. Lukács, J. Molnár, S. Wongwises, G. Gróf, I.M. Szilágyi, A Novel Experimental Study on the Rheological Properties and Thermal Conductivity of Halloysite Nanofluids, *Nanomaterials*. 10 (2020) 1834. https://doi.org/10.3390/nano10091834.

Impact factor: 5.719 (2021); SCImago Quartile (2020): Q1; Independent Citations: 49

[P2] **Le Ba, T.**, Baqer, A., Saad Kamel, M., Gróf, G., Odhiambo, V.O., Wongwises, S., Ferenc, L., Szilágyi, I.M. Experimental Study of Halloysite Nanofluids in Pool Boiling Heat Transfer, *Molecules*. 27 (2022), 729. https://doi.org/10.3390/molecules27030729

Impact factor: 4,927 (2021); SCImago Quartile (2022): Q2; Independent Citations: 17

[P3] **Le Ba, T.**, Várady, Z.I., Lukács, I.E. et al. Experimental investigation of rheological properties and thermal conductivity of SiO_2–P25 TiO_2 hybrid nanofluids, *J Therm Anal Calorim.* 146 (2021) 493–507. https://doi.org/10.1007/s10973-020-10022-4

Impact factor: 4.755 (2021); SCImago Quartile (2022): Q2; Independent Citations: 28

[P4] **Le Ba, T.**, Gróf, G., Odhiambo, V.O., Wongwises, S., Szilágyi, I.M. A CFD Study on Heat Transfer Performance of SiO_2-TiO_2 Nanofluids under Turbulent Flow, *Nanomaterials*. 12 (2022) 299. https://doi.org/10.3390/nano12030299

Impact factor: 5.719 (2021); SCImago Quartile (2022): Q1; Independent Citations: 17

[P5] **T. Le Ba**, M. Bohus, I.E. Lukács, S. Wongwises, G. Gróf, K. Hernadi, I.M. Szilágyi, Comparative Study of Carbon Nanosphere and Carbon Nanopowder on Viscosity and Thermal Conductivity of Nanofluids, *Nanomaterials*. 11 (2021) 608. https://doi.org/10.3390/NANO11030608.

Impact factor: 5.719 (2021); SCImago Quartile (2021): Q1; Independent Citations: 27

❖ Additional journal publications

[P6] **Le Ba, T.**, Mahian, O., Wongwises, S. et al. Review on the recent progress in the preparation and stability of graphene-based nanofluids, *J Therm Anal Calorim* 142 (2020) 1145–1172. https://doi.org/10.1007/s10973-020-09365-9

Impact factor: 4.755 (2021); SCImago Quartile (2022): Q2; Independent Citations: 113

[P7] V.O. Odhiambo, C.R.M. Mustafa, **L.B. Thong**, Z. Kónya, C. Cserháti, Z. Erdélyi, I.E. Lukác, I.M. Szilágyi, Preparation of $TiO_2/WO_3/C/N$ Composite Nanofibers by Electrospinning Using Precursors Soluble in Water and Their Photocatalytic Activity in Visible Light, *Nanomaterials*. 11 (2021) 351. https://doi.org/10.3390/NANO11020351.

Impact factor: 5.719 (2021); SCImago Quartile (2021): Q1; Independent Citations: 8

[P8] V.O. Odhiambo, **T. Le Ba**, Z. Kónya, C. Cserháti, Z. Erdélyi, M. C Naomi, I. Miklós Szilágyi, Preparation of TiO_2–MoO_3 composite nanofibers by water-based electrospinning process and their application in photocatalysis, *Mater. Sci. Semicond. Process*. 147 (2022) 106699. https://doi.org/10.1016/j.mssp.2022.106699.

Impact factor: 4.644 (2021); SCImago Quartile (2022): Q2; Independent Citations: 24

[P9] Bohus, M.; **Thong, L. B.**; Hernadi, K.; Gróf, G.; Kónya, Z.; Erdélyi, Z.; Parditka, B.; Igricz, T.; Szilágyi, I.M. Thermal Conductivity Enhancement of Atomic Layer Deposition Surface-Modified Carbon Nanosphere and Carbon Nanopowder Nanofluids, *Nanomaterials*. 12 (**2022**) 2226. https://doi.org/10.3390/nano12132226

Impact factor: 5.719 (2021); SCImago Quartile (2022): Q1; Independent Citations: 8

[P10] Zalán, I. V.; **Thong, L. B.**; Bence P.; Zoltán E.; Klara H.; Gábor K.; Gyula G.; Szilágyi, I.M. Experimental investigation of rheological properties and thermal conductivity of SiO_2-TiO_2 composite nanofluids prepared by atomic layer deposition, *Nanomaterials*. 12 (**2022**) 3014. https://doi.org/10.3390/nano12173014

Impact factor: 5.719 (2021); SCImago Quartile (2022): Q1; Independent Citations: 5

❖ Conference

[P11] **Thong, L. B.**, Omid M., Marcell B., Imre, M. S. Natural convection of carbon sphere water-based nanofluids in a differentially heated square cavity. *2nd Journal of Thermal*

Analysis and Calorimetry Conference and 7th V4 (Joint Czech-Hungarian-Polish-Slovakian) Thermoanalytical Conference (JTACC+V4), 18-21 June 2019, Budapest (Hungary). (2019).

[P12] **Thong, L. B.**, Omid M., Zalán I. V., Imre, M. S. Numerical investigation of natural convection of SiO_2-TiO_2 hybrid water-based nanofluids with heated square cavity. *2nd Journal of Thermal Analysis and Calorimetry Conference and 7th V4 (Joint Czech-Hungarian-Polish-Slovakian) Thermoanalytical Conference (JTACC+V4)*, 18-21 June 2019, Budapest (Hungary). (2019).

[P13] **Thong L. B.**, Imre M. S. Recent Progress in Graphene based Nanofluids – A Concise Review. *10th International Engineering Symposium at Bánki*, 21 August 2018, Budapest (Hungary). (2018).

[P14] **Thong L. B.**, Imre M. S. Investigation of thermal conductivity and viscosity of nanofluids containing halloysite. *XVIII Conference of the George Olah Doctoral School*, 28 September 2020, Budapest (Hungary). (2020).

[P15] **Thong L. B.**, Imre M. S. Investigation of thermal conductivity and viscosity of nanofluids containing halloysite. *The Materials science day of PhD student*, 16 November 2020, Veszprem (Hungary). (2020).

[P16] Marcell B., **Thong L. B.**, Imre M. S. Investigation of carbon based nanofluids containing carbon nanospheres and carbon nanopowder. *3rd European Symposium on Nanofluids (ESNf)*, 9-10 September 2021, Iasi (Romania). (2021).

[P17] Zalán I. V., **Thong L. B.**, Imre M. S. Experimental investigation of rheological properties and thermal conductivity of SiO_2–P25 TiO_2 hybrid nanofluids. *3rd European Symposium on Nanofluids (ESNf)*, 9-10 September 2021, Iasi (Romania). (2021).

8. Acknowledgement

I would like to thank all those who helped me during my research:

- My great supervisor, Prof. Imre Miklós Szilágyi (Institute of Physical Metallurgy, Metal Forming and Nanotechnology) for supervising my work and providing support, motivation and encouragement during my work and my life;
- Várady Zalán István (MSc), Bohus Marcell (MSc), Alkurdi Ahmed Qani (MSc) and Baqer Ahmed (MSc), who had the thesis that I supervised during my PhD course and contributed their work to my research topics;
- Dr. Gróf Gyula (BME Department of Energy Engineering) provided expertise in research methods, evaluation, and thermal conductivity measurements. Dr. Somchai Wongwises (Thailand) also assisted with research methods and evaluation. Dr. Molnár János (BME Department of Physical Chemistry and Materials Science) conducted rheological measurements. Dr. István Endre Lukács (MTA Institute of Technical Physics and Materials Science of the Hungarian Academy of Sciences) helped prepare SEM images. Dr. Klára Hernádi and PhD student Anna Szabó (SZTE Applied & Environmental Chemistry Department) were instrumental in preparing TEM images. Tamás Igricz (BME SZKT) assisted with Raman measurements. Dr. Menyhárd Alfréd and Dr. László Krisztina (BME Department of Physical Chemistry and Materials Science) helped prepare DOM images and perform specific surface area measurements, respectively. Dr. Gyarmati Benjámin (BME Department of Physical Chemistry and Materials Science) assisted with zeta potential measurements. Dr. Mohammed Saad Kamel and Dr. Lezsovits Ferenc (BME Department of Energy Engineering) provided support for pool boiling measurements.
- My colleagues, members of the BME TACS research group, for advice, ideas and for unforgettable moments;
- Hungarian government and Tempus Public Foundation, for their financial support in Stipendium Hungaricum Scholarship;
- Research funds: NRDI Fund TKP2021, NRDI K 124212, NRDI TNN_16 123631 (within project No. VEKOP-2.3.2-16-2017-00013), Project no. ADVANCED 153435 (under ADVANCED_25 funding scheme) and Thematic Excellence Programme (TKP2020-IKA-04)
- Finally, my family, especially my dear wife and lovely daughters, supported and encouraged throughout the work.

9. References

[1] A. O. Maselugbo, B. L. Sadiku, and J. R. Alston, “Thermal conductivity of ethylene glycol and propylene glycol nanofluids with boron nitride nano-barbs,” *Nanoscale*, vol. 15, no. 18, pp. 8406–8415, May 2023, doi: 10.1039/D2NR06332H.

[2] J. Fan and L. Wang, “Review of Heat Conduction in Nanofluids,” *J. Heat Transfer*, vol. 133, no. 4, Apr. 2011, doi: 10.1115/1.4002633.

[3] L. Godson, B. Raja, D. Mohan Lal, and S. Wongwises, “Enhancement of heat transfer using nanofluids—An overview,” *Renewable and Sustainable Energy Reviews*, vol. 14, no. 2, pp. 629–641, Feb. 2010, doi: 10.1016/j.rser.2009.10.004.

[4] M. H. Mousa, N. Miljkovic, and K. Nawaz, “Review of heat transfer enhancement techniques for single phase flows,” *Renewable and Sustainable Energy Reviews*, vol. 137, p. 110566, Mar. 2021, doi: 10.1016/j.rser.2020.110566.

[5] S. Kim, S. Kang, and J. Lee, “High-Thermal-Conductivity and High-Fluidity Heat Transfer Emulsion with 89 wt% Suspended Liquid Metal Microdroplets,” *ACS Omega*, vol. 8, no. 20, pp. 17748–17757, May 2023, doi: 10.1021/acsomega.3c00487.

[6] H. Hanif, S. Shafie, R. Roslan, and A. Ali, “Collision of hybrid nanomaterials in an upper-convected Maxwell nanofluid: A theoretical approach,” *J. King Saud Univ. Sci.*, vol. 35, no. 1, p. 102389, Jan. 2023, doi: 10.1016/j.jksus.2022.102389.

[7] S. Kalsi, S. Kumar, A. Kumar, T. Alam, and D. Dobrotă, “Thermophysical properties of nanofluids and their potential applications in heat transfer enhancement: A review,” *Arabian Journal of Chemistry*, vol. 16, no. 11, p. 105272, Nov. 2023, doi: 10.1016/j.arabjc.2023.105272.

[8] J. Buongiorno *et al.*, “A benchmark study on the thermal conductivity of nanofluids,” *J. Appl. Phys.*, vol. 106, no. 9, p. 094312, Nov. 2009, doi: 10.1063/1.3245330.

[9] H. Masuda, A. Ebata, K. Teramae, and N. Hishinuma, “Alteration of Thermal Conductivity and Viscosity of Liquid by Dispersing Ultra-Fine Particles. Dispersion of Al_2O_3, SiO_2 and TiO_2 Ultra-Fine Particles.,” *Netsu Bussei*, vol. 7, no. 4, pp. 227–233, Oct. 1993, doi: 10.2963/jjtp.7.227.

[10] S. U. S. Choi and J. A. Eastman, “Enhancing thermal conductivity of fluids with nanoparticles,” *ASME International Mechanical Engineering Congress and Exposition*, vol. 66, no. March, pp. 99–105, 1995, doi: 10.1115/1.1532008.

[11] S. Kumar Singh, “Review on the Stability of the Nanofluids,” in *Pipeline Engineering - Design, Failure, and Management*, IntechOpen, 2023. doi: 10.5772/intechopen.107154.

[12] K. Apmann, R. Fulmer, A. Soto, and S. Vafaei, “Thermal Conductivity and Viscosity: Review and Optimization of Effects of Nanoparticles,” *Materials*, vol. 14, no. 5, p. 1291, Mar. 2021, doi: 10.3390/ma14051291.

[13] M. F. Nabil, W. H. Azmi, K. A. Hamid, and R. Mamat, “Experimental investigation of heat transfer and friction factor of TiO_2-SiO_2 nanofluids in water:ethylene glycol mixture,” *Int. J. Heat Mass Transf.*, vol. 124, pp. 1361–1369, Sep. 2018, doi: 10.1016/j.ijheatmasstransfer.2018.04.143.

[14] A. Turgut, I. Tavman, M. Chirtoc, H. P. Schuchmann, C. Sauter, and S. Tavman, “Thermal Conductivity and Viscosity Measurements of Water-Based TiO_2 Nanofluids,” *Int. J. Thermophys.*, vol. 30, no. 4, pp. 1213–1226, Aug. 2009, doi: 10.1007/s10765-009-0594-2.

[15] M. F. Nabil, W. H. Azmi, K. Abdul Hamid, R. Mamat, and F. Y. Hagos, “An experimental study on the thermal conductivity and dynamic viscosity of TiO_2-SiO_2 nanofluids in water: Ethylene glycol mixture,” *International Communications in Heat and Mass Transfer*, vol. 86, pp. 181–189, Aug. 2017, doi: 10.1016/j.icheatmasstransfer.2017.05.024.

[16] S. Bobbo, B. Buonomo, O. Manca, S. Vigna, and L. Fedele, “Analysis of the Parameters Required to Properly Define Nanofluids for Heat Transfer Applications,” *Fluids*, vol. 6, no. 2, p. 65, Feb. 2021, doi: 10.3390/fluids6020065.

[17] L. Yang, W. Ji, M. Mao, and J. Huang, “Dynamic stability, sedimentation, and time-dependent heat transfer characteristics of TiO_2 and CNT nanofluids,” *J. Therm. Anal. Calorim.*, vol. 141, no. 3, pp. 1183–1195, Aug. 2020, doi: 10.1007/s10973-019-09103-w.

[18] M. Mehrali *et al.*, “Investigation of thermal conductivity and rheological properties of nanofluids containing graphene nanoplatelets,” *Nanoscale Res. Lett.*, vol. 9, no. 1, p. 15, Jan. 2014, doi: 10.1186/1556-276X-9-15.

[19] A. Asadi *et al.*, “Recent advances in preparation methods and thermophysical properties of oil-based nanofluids: A state-of-the-art review,” *Powder Technol.*, vol. 352, pp. 209–226, Jun. 2019, doi: 10.1016/j.powtec.2019.04.054.

[20] M. Garcia Tobar, R. W. Contreras Urgiles, B. Jimenez Cordero, and J. Guillen Matute, “Nanotechnology in Lubricants: A Systematic Review of the Use of Nanoparticles to Reduce the Friction Coefficient,” *Lubricants*, vol. 12, no. 5, p. 166, May 2024, doi: 10.3390/lubricants12050166.

[21] S. Lee, SU.-S. Choi, S. Li, and J. A. Eastman, “Measuring thermal conductivity of fluids containing oxide nanoparticles,” *J. Heat Transfer*, vol. 121, no. 2, pp. 280–289, May 1999, doi: 10.1115/1.2825978.

[22] J. A. Eastman, S. U. S. Choi, S. Li, W. Yu, and L. J. Thompson, “Anomalously increased effective thermal conductivities of ethylene glycol-based nanofluids containing copper nanoparticles,” *Appl. Phys. Lett.*, vol. 78, no. 6, pp. 718–720, Feb. 2001, doi: 10.1063/1.1341218.

[23] S. U. S. Choi, Z. G. Zhang, W. Yu, F. E. Lockwood, and E. A. Grulke, “Anomalous thermal conductivity enhancement in nanotube suspensions,” *Appl. Phys. Lett.*, vol. 79, no. 14, pp. 2252–2254, Oct. 2001, doi: 10.1063/1.1408272.

[24] S. M. S. Murshed, K. C. Leong, and C. Yang, “Investigations of thermal conductivity and viscosity of nanofluids,” *International Journal of Thermal Sciences*, vol. 47, no. 5, pp. 560–568, May 2008, doi: 10.1016/j.ijthermalsci.2007.05.004.

[25] Y. Raja Sekhar, K. V. Sharma, R. Thundil Karupparaj, and C. Chiranjeevi, “Heat Transfer Enhancement with Al_2O_3 Nanofluids and Twisted Tapes in a Pipe for Solar Thermal Applications,” *Procedia Eng.*, vol. 64, pp. 1474–1484, Jan. 2013, doi: 10.1016/j.proeng.2013.09.229.

[26] S. Suresh, K. P. Venkitaraj, P. Selvakumar, and M. Chandrasekar, “Effect of Al_2O_3–Cu/water hybrid nanofluid in heat transfer,” *Exp. Therm. Fluid Sci.*, vol. 38, pp. 54–60, Apr. 2012, doi: 10.1016/j.expthermflusci.2011.11.007.

[27] S. A. Putnam, D. G. Cahill, P. V. Braun, Z. Ge, and R. G. Shimmin, “Thermal conductivity of nanoparticle suspensions,” *J. Appl. Phys.*, vol. 99, no. 8, p. 084308, Apr. 2006, doi: 10.1063/1.2189933.

[28] M. Farbod, R. Kouhpeymani asl, and A. R. Noghreh abadi, “Morphology dependence of thermal and rheological properties of oil-based nanofluids of CuO nanostructures,” *Colloids Surf. A Physicochem. Eng. Asp.*, vol. 474, pp. 71–75, Jun. 2015, doi: 10.1016/j.colsurfa.2015.02.049.

[29] M. J. Biercuk, M. C. Llaguno, M. Radosavljevic, J. K. Hyun, A. T. Johnson, and J. E. Fischer, “Carbon nanotube composites for thermal management,” *Appl. Phys. Lett.*, vol. 80, no. 15, pp. 2767–2769, Apr. 2002, doi: 10.1063/1.1469696.

[30] H. Xie, H. Lee, W. Youn, and M. Choi, “Nanofluids containing multiwalled carbon nanotubes and their enhanced thermal conductivities,” *J. Appl. Phys.*, vol. 94, no. 8, pp. 4967–4971, Oct. 2003, doi: 10.1063/1.1613374.

[31] W. H. Azmi, K. V. Sharma, P. K. Sarma, R. Mamat, and G. Najafi, “Heat transfer and friction factor of water based TiO_2 and SiO_2 nanofluids under turbulent flow in a tube,” *International Communications in Heat and Mass Transfer*, vol. 59, pp. 30–38, Dec. 2014, doi: 10.1016/j.icheatmasstransfer.2014.10.007.

[32] I. Gonçalves *et al.*, “Thermal Conductivity of Nanofluids: A Review on Prediction Models, Controversies and Challenges,” *Applied Sciences*, vol. 11, no. 6, p. 2525, Mar. 2021, doi: 10.3390/app11062525.

[33] T. Theres Baby and R. Sundara, “Surfactant free magnetic nanofluids based on core-shell type nanoparticle decorated multiwalled carbon nanotubes,” *J. Appl. Phys.*, vol. 110, no. 6, p. 064325, Sep. 2011, doi: 10.1063/1.3642974.

[34] M. Batmunkh *et al.*, “Thermal Conductivity of TiO_2 Nanoparticles Based Aqueous Nanofluids with an Addition of a Modified Silver Particle,” *Ind. Eng. Chem. Res.*, vol. 53, no. 20, pp. 8445–8451, May 2014, doi: 10.1021/ie403712f.

[35] D. Madhesh, R. Parameshwaran, and S. Kalaiselvam, “Experimental investigation on convective heat transfer and rheological characteristics of Cu–TiO_2 hybrid nanofluids,” *Exp. Therm. Fluid Sci.*, vol. 52, pp. 104–115, Jan. 2014, doi: 10.1016/j.expthermflusci.2013.08.026.

[36] K. Y. Leong, Z. A. Najwa, K. Z. Ku Ahmad, and H. C. Ong, “Investigation on Stability and Optical Properties of Titanium Dioxide and Aluminum Oxide Water-Based Nanofluids,” *Int. J. Thermophys.*, vol. 38, no. 5, p. 77, May 2017, doi: 10.1007/s10765-017-2218-6.

[37] M. K. P. C and M. Muruganandam, “Stability Analysis of Heat Transfer MWCNT with Different Base Fluids,” *Journal of Applied Fluid Mechanics*, vol. 10, no. SI, Oct. 2017, doi: 10.36884/jafm.10.SI.28270.

[38] S. Witharana, I. Palabiyik, Z. Musina, and Y. Ding, “Stability of glycol nanofluids — The theory and experiment,” *Powder Technol.*, vol. 239, pp. 72–77, May 2013, doi: 10.1016/j.powtec.2013.01.039.

[39] A. Menbari, A. A. Alemrajabi, and Y. Ghayeb, “Investigation on the stability, viscosity and extinction coefficient of CuO–Al_2O_3/Water binary mixture nanofluid,” *Exp. Therm. Fluid Sci.*, vol. 74, pp. 122–129, Jun. 2016, doi: 10.1016/j.expthermflusci.2015.11.025.

[40] S. Jana, A. Salehi-Khojin, and W.-H. Zhong, “Enhancement of fluid thermal conductivity by the addition of single and hybrid nano-additives,” *Thermochim. Acta*, vol. 462, no. 1–2, pp. 45–55, Oct. 2007, doi: 10.1016/j.tca.2007.06.009.

[41] N. A. Yacob, A. Ishak, I. Pop, and K. Vajravelu, “Boundary layer flow past a stretching/shrinking surface beneath an external uniform shear flow with a convective surface boundary condition in a nanofluid,” *Nanoscale Res. Lett.*, vol. 6, no. 1, p. 314, Dec. 2011, doi: 10.1186/1556-276X-6-314.

[42] M. K. Moraveji and R. M. Ardehali, “CFD modeling (comparing single and two-phase approaches) on thermal performance of Al_2O_3/water nanofluid in mini-channel heat sink,” *International Communications in Heat and Mass Transfer*, vol. 44, pp. 157–164, May 2013, doi: 10.1016/j.icheatmasstransfer.2013.02.012.

[43] I. Razzaq *et al.*, “Nanofluids for Advanced Applications: A Comprehensive Review on Preparation Methods, Properties, and Environmental Impact,” *ACS Omega*, vol. 10, no. 6, p. 5251, Feb. 2025, doi: 10.1021/ACSOMEGA.4C10143.

[44] J. A. Eastman, U. S. Choi, S. Li, L. J. Thompson, and S. Lee, “Enhanced Thermal Conductivity through the Development of Nanofluids,” *MRS Proceedings*, vol. 457, p. 3, Feb. 1996, doi: 10.1557/PROC-457-3.

[45] H. Zhu, Y. Lin, and Y. Yin, “A novel one-step chemical method for preparation of copper nanofluids,” *J. Colloid Interface Sci.*, vol. 277, no. 1, pp. 100–103, Sep. 2004, doi: 10.1016/j.jcis.2004.04.026.

[46] S. Mukherjee and S. Paria, “Preparation and Stability of Nanofluids-A Review,” *IOSR Journal of Mechanical and Civil Engineering (IOSR-JMCE)*, vol. 9, no. 2, pp. 63–69, 2013.

[47] W. Yu, H. Xie, and D. Bao, “Enhanced thermal conductivities of nanofluids containing graphene oxide nanosheets,” *Nanotechnology*, vol. 21, no. 5, p. 055705, Feb. 2010, doi: 10.1088/0957-4484/21/5/055705.

[48] H. Zhang, S. Qing, Q. Gui, X. Zhang, and A. Zhang, “Effects of surface modification and surfactants on stability and thermophysical properties of TiO_2/water nanofluids,” *J. Mol. Liq.*, vol. 349, p. 118098, Mar. 2022, doi: 10.1016/j.molliq.2021.118098.

[49] L. Jia, Y. Chen, S. Lei, S. Mo, X. Luo, and X. Shao, “External electromagnetic field-aided freezing of CMC-modified graphene/water nanofluid,” *Appl. Energy*, vol. 162, pp. 1670–1677, 2016, doi: 10.1016/j.apenergy.2015.08.067.

[50] J. A. Alberola, R. Mondragón, J. E. Juliá, L. Hernández, and L. Cabedo, “Characterization of halloysite-water nanofluid for heat transfer applications,” *Appl. Clay Sci.*, vol. 99, pp. 54–61, Sep. 2014, doi: 10.1016/j.clay.2014.06.012.

[51] M. Hashemi and S. H. Noie, “Study of flow boiling heat transfer characteristics of critical heat flux using carbon nanotubes and water nanofluid,” *J. Therm. Anal. Calorim.*, vol. 130, no. 3, pp. 2199–2209, Dec. 2017, doi: 10.1007/s10973-017-6661-1.

[52] W. Yu, H. Xie, L. Chen, Y. Li, and D. Li, “The Preparation and Thermal Conductivities Enhacement of Nanofluids Containing Graphene Oxide Nanosheets,” in *2010 14th International Heat Transfer Conference, Volume 6*, ASME, Jan. 2010, pp. 569–573. doi: 10.1115/IHTC14-22055.

[53] F. Agresti *et al.*, “Thermal Conductivity and Viscosity Measurements of Water-Based Silica Nanofluids,” *NSTI-Nanotech*, vol. 2, pp. 478–481, 2011.

[54] J. S. Park, K. D. Kihm, H. Kim, G. Lim, S. Cheon, and J. S. Lee, “Wetting and Evaporative Aggregation of Nanofluid Droplets on CVD-Synthesized Hydrophobic Graphene Surfaces,” *Langmuir*, vol. 30, no. 28, pp. 8268–8275, Jul. 2014, doi: 10.1021/la404854z.

[55] A. Ghozatloo, M. Shariaty-Niasar, and A. M. Rashidi, “Preparation of nanofluids from functionalized Graphene by new alkaline method and study on the thermal conductivity and stability,” *International Communications in Heat and Mass Transfer*, vol. 42, pp. 89–94, Mar. 2013, doi: 10.1016/J.ICHEATMASSTRANSFER.2012.12.007.

[56] D. K. Agarwal, A. Vaidyanathan, and S. Sunil Kumar, “Experimental investigation on thermal performance of kerosene-graphene nanofluid,” *Exp. Therm. Fluid Sci.*, vol. 71, pp. 126–137, 2016, doi: 10.1016/j.expthermflusci.2015.10.028.

[57] D. Luo *et al.*, “Nanofluid of graphene-based amphiphilic Janus nanosheets for tertiary or enhanced oil recovery: High performance at low concentration,” *Proceedings of the National Academy of Sciences*, vol. 113, no. 28, pp. 7711–7716, 2016, doi: 10.1073/pnas.1608135113.

[58] X. Su, M. Zhang, W. Han, and X. Guo, “Experimental study on the heat transfer performance of an oscillating heat pipe with self-rewetting nanofluid,” *Int. J. Heat Mass Transf.*, vol. 100, pp. 378–385, 2016, doi: 10.1016/j.ijheatmasstransfer.2016.04.094.

[59] A. H. Alami *et al.*, “A critical insight on nanofluids for heat transfer enhancement,” *Scientific Reports 2023 13:1*, vol. 13, no. 1, pp. 15303-, Sep. 2023, doi: 10.1038/s41598-023-42489-0.

[60] H. Yarmand *et al.*, “Graphene nanoplatelets–silver hybrid nanofluids for enhanced heat transfer,” *Energy Convers. Manag.*, vol. 100, pp. 419–428, Aug. 2015, doi: 10.1016/J.ENCONMAN.2015.05.023.

[61] P. Kulkarni, R. Sureshkumar, and P. Biswas, “Multiscale simulation of irreversible deposition in presence of double layer interactions.,” *J. Colloid Interface Sci.*, vol. 260, no. 1, pp. 36–48, Apr. 2003.

[62] M. R. Tchalala, D. H. Anjum, and S. Chaieb, “Effect of Ionic Liquid (emim BF_4) on the Dispersion of Gold Nanoparticles,” *J. Phys. Conf. Ser.*, vol. 758, no. 012020, p. 012020, Oct. 2016, doi: 10.1088/1742-6596/758/1/012020.

[63] W. Heller, “Effects of macromolecular compounds in disperse systems,” *Pure and Applied Chemistry*, vol. 12, no. 1–4, pp. 249–274, Jan. 1966, doi: 10.1351/pac196612010249.

[64] W. Heller and T. L. Pugh, “``Steric Protection'' of Hydrophobic Colloidal Particles by Adsorption of Flexible Macromolecules,” *J. Chem. Phys.*, vol. 22, no. 10, pp. 1778–1778, Oct. 1954, doi: 10.1063/1.1739899.

[65] S. Askari, R. Lotfi, A. M. Rashidi, H. Koolivand, and M. Koolivand-Salooki, “Rheological and thermophysical properties of ultra-stable kerosene-based Fe_3O_4/Graphene nanofluids for energy conservation,” *Energy Convers. Manag.*, vol. 128, pp. 134–144, Nov. 2016, doi: 10.1016/j.enconman.2016.09.037.

[66] K. S. Pavithra, Fasiulla, M. P. Yashoda, and S. Prasannakumar, “Synthesis, characterisation and thermal conductivity of CuO - water based nanofluids with different dispersants,” *Particulate Science and Technology*, vol. 38, no. 5, pp. 559–567, Jul. 2020, doi: 10.1080/02726351.2019.1574941.

[67] L. G. Bach, Md. R. Islam, J. T. Kim, S. Seo, and K. T. Lim, “Encapsulation of Fe_3O_4 magnetic nanoparticles with poly(methyl methacrylate) via surface functionalized thiol-lactam initiated radical polymerization,” *Appl. Surf. Sci.*, vol. 258, no. 7, pp. 2959–2966, Jan. 2012, doi: 10.1016/j.apsusc.2011.11.016.

[68] J. Turkevich, P. C. Stevenson, and J. Hillier, “A study of the nucleation and growth processes in the synthesis of colloidal gold,” *Discuss. Faraday Soc.*, vol. 11, no. 0, p. 55, Jan. 1951, doi: 10.1039/df9511100055.

[69] J. Turkevich, “Colloidal gold. Part I,” *Gold Bull.*, vol. 18, no. 3, pp. 86–91, Sep. 1985, doi: 10.1007/BF03214690.

[70] M. Mehrali *et al.*, “An ecofriendly graphene-based nanofluid for heat transfer applications,” *J. Clean. Prod.*, vol. 137, pp. 555–566, 2016, doi: 10.1016/j.jclepro.2016.07.136.

[71] A. K. M. M. Haque *et al.*, “Surface modification of graphene nanoparticles by acid treatment and grinding process,” *J. Nanosci. Nanotechnol.*, vol. 18, no. 1, 2018, doi: 10.1166/jnn.2018.13928.

[72] H. Yarmand *et al.*, “Experimental investigation of thermo-physical properties, convective heat transfer and pressure drop of functionalized graphene nanoplatelets aqueous nanofluid in a square heated pipe,” *Energy Convers. Manag.*, vol. 114, pp. 38–49, 2016, doi: 10.1016/j.enconman.2016.02.008.

[73] H. Yarmand *et al.*, “Study of synthesis, stability and thermo-physical properties of graphene nanoplatelet/platinum hybrid nanofluid,” *International Communications in Heat and Mass Transfer*, vol. 77, pp. 15–21, 2016, doi: 10.1016/j.icheatmasstransfer.2016.07.010.

[74] H. Zhang, S. Qing, Y. Zhai, X. Zhang, and A. Zhang, “The changes induced by pH in TiO_2/water nanofluids: Stability, thermophysical properties and thermal performance,” *Powder Technol.*, vol. 377, pp. 748–759, Jan. 2021, doi: 10.1016/j.powtec.2020.09.004.

[75] J. P. Vallejo, J. Pérez-Tavernier, D. Cabaleiro, J. Fernández-Seara, and L. Lugo, “Potential heat transfer enhancement of functionalized graphene nanoplatelet dispersions in a propylene glycol-water mixture. Thermophysical profile,” *Journal of Chemical Thermodynamics*, vol. 123, pp. 174–184, 2018, doi: 10.1016/j.jct.2018.04.007.

[76] W. S. Sarsam, A. Amiri, S. N. Kazi, and A. Badarudin, “Stability and thermophysical properties of non-covalently functionalized graphene nanoplatelets nanofluids,” *Energy Convers. Manag.*, vol. 116, pp. 101–111, 2016, doi: 10.1016/j.enconman.2016.02.082.

[77] S. Askari, R. Lotfi, A. Seifkordi, A. M. Rashidi, and H. Koolivand, “A novel approach for energy and water conservation in wet cooling towers by using MWNTs and nanoporous graphene nanofluids,” *Energy Convers. Manag.*, vol. 109, pp. 10–18, 2016, doi: 10.1016/j.enconman.2015.11.053.

[78] C. Selvam, D. M. Lal, and S. Harish, “Thermal conductivity enhancement of ethylene glycol and water with graphene nanoplatelets,” *Thermochim. Acta*, vol. 642, pp. 32–38, 2016, doi: 10.1016/j.tca.2016.09.002.

[79] M. Mehrali *et al.*, “Effect of nitrogen-doped graphene nanofluid on the thermal performance of the grooved copper heat pipe,” *Energy Convers. Manag.*, vol. 118, pp. 459–473, 2016, doi: 10.1016/j.enconman.2016.04.028.

[80] M. Zhou, G. Xia, J. Li, L. Chai, and L. Zhou, “Analysis of factors influencing thermal conductivity and viscosity in different kinds of surfactant solutions,” *Exp. Therm. Fluid Sci.*, vol. 36, pp. 22–29, 2012, doi: 10.1016/j.expthermflusci.2011.07.014.

[81] R. Choudhary, D. Khurana, A. Kumar, and S. Subudhi, “Stability analysis of Al_2O_3/water nanofluids,” *J. Exp. Nanosci.*, vol. 12, no. 1, pp. 140–151, Jan. 2017, doi: 10.1080/17458080.2017.1285445.

[82] M. Myekhlai, T. Lee, B. Baatar, H. Chung, and H. Jeong, “Thermal Conductivity on the Nanofluid of Graphene and Silver Nanoparticles Composite Material,” *J. Nanosci. Nanotechnol.*, vol. 16, no. 2, pp. 1633–1637, 2016, doi: 10.1166/jnn.2016.10711.

[83] S. Sen, V. Govindarajan, C. J. Pelliccione, J. Wang, D. J. Miller, and E. V. Timofeeva, “Surface Modification Approach to TiO_2 Nanofluids with High Particle Concentration, Low Viscosity, and Electrochemical Activity,” *ACS Appl. Mater. Interfaces*, vol. 7, no. 37, pp. 20538–20547, Sep. 2015, doi: 10.1021/acsami.5b05864.

[84] M. S. Hosseini, M. Khazaei, M. Misaghi, and M. H. Koosheshi, “Improving the stability of nanofluids via surface-modified titanium dioxide nanoparticles for wettability alteration of oil-wet carbonate reservoirs,” *Mater. Res. Express*, vol. 9, no. 3, p. 035005, Mar. 2022, doi: 10.1088/2053-1591/ac4fdf.

[85] M. R. Fahad and B. A. Abdulmajeed, “Surface Modification of TiO_2-Al_2O_3 Nanoparticles for the Enhancement of the Rheological Properties of Base Lubricating Oil,” *Journal of Applied Research and Technology*, vol. 20, no. 1, pp. 37–47, Mar. 2022, doi: 10.22201/icat.24486736e.2022.20.1.1556.

[86] M. Mehrali *et al.*, “Experimental investigation of thermophysical properties, entropy generation and convective heat transfer for a nitrogen-doped graphene nanofluid in a laminar flow

regime," *Advanced Powder Technology*, vol. 27, no. 2, pp. 717–727, 2016, doi: 10.1016/j.apt.2016.02.028.

[87] M. Kole and T. K. Dey, "Thermal performance of screen mesh wick heat pipes using water-based copper nanofluids," *Appl. Therm. Eng.*, vol. 50, no. 1, pp. 763–770, Jan. 2013, doi: 10.1016/j.applthermaleng.2012.06.049.

[88] S. khosrojerdi, A. M. Lavasani, and M. Vakili, "Experimental study of photothermal specifications and stability of graphene oxide nanoplatelets nanofluid as working fluid for low-temperature Direct Absorption Solar Collectors (DASCs)," *Solar Energy Materials and Solar Cells*, vol. 164, no. February, pp. 32–39, 2017, doi: 10.1016/j.solmat.2017.02.007.

[89] D. Wen, G. Lin, S. Vafaei, and K. Zhang, "Review of nanofluids for heat transfer applications," *Particuology*, vol. 7, no. 2, pp. 141–150, Apr. 2009, doi: 10.1016/j.partic.2009.01.007.

[90] A. Asadi, I. M. Alarifi, V. Ali, and H. M. Nguyen, "An experimental investigation on the effects of ultrasonication time on stability and thermal conductivity of MWCNT-water nanofluid: Finding the optimum ultrasonication time," *Ultrason. Sonochem.*, vol. 58, p. 104639, Nov. 2019, doi: 10.1016/j.ultsonch.2019.104639.

[91] K. Pate and P. Safier, "Chemical metrology methods for CMP quality," *Advances in Chemical Mechanical Planarization (CMP)*, pp. 299–325, Jan. 2016, doi: 10.1016/B978-0-08-100165-3.00012-7.

[92] W. Yu and H. Xie, "A Review on Nanofluids: Preparation, Stability Mechanisms, and Applications," *J. Nanomater.*, vol. 2012, no. 1, Jan. 2012, doi: 10.1155/2012/435873.

[93] M. Vakili, S. M. Hosseinalipour, S. Delfani, S. Khosrojerdi, and M. Karami, "Experimental investigation of graphene nanoplatelets nanofluid-based volumetric solar collector for domestic hot water systems," *Solar Energy*, vol. 131, pp. 119–130, 2016, doi: 10.1016/j.solener.2016.02.034.

[94] M. Vakili, S. M. Hosseinalipour, S. Delfani, and S. Khosrojerdi, "Photothermal properties of graphene nanoplatelets nanofluid for low-temperature direct absorption solar collectors," *Solar Energy Materials and Solar Cells*, vol. 152, pp. 187–191, 2016, doi: 10.1016/j.solmat.2016.01.038.

[95] S. N. M. Zainon, W. H. Azmi, and A. H. Hamisa, "Thermo-physical Properties of TiO_2-SiO_2 Hybrid Nanofluids Dispersion with Water/Bio-glycol Mixture," *J. Phys. Conf. Ser.*, vol. 2000, no. 1, p. 012003, Aug. 2021, doi: 10.1088/1742-6596/2000/1/012003.

[96] S. Bharti, "A critical review on flocculants and flocculation," *Non-Metallic Material Science*, vol. 01, no. 01, 2019, doi: 10.30564/omms.v1i1.645.

[97] X. Wei and L. Wang, "Particuology Synthesis and thermal conductivity of microfluidic copper nanofluids," *Particuology*, vol. 8, no. 3, pp. 262–271, 2010, doi: 10.1016/j.partic.2010.03.001.

[98] N. Wang, G. Xu, S. Li, and X. Zhang, "Thermal Properties and Solar Collection Characteristics of Oil-based Nanofluids with Low Graphene Concentration," *Energy Procedia*, vol. 105, pp. 194–199, 2017, doi: 10.1016/j.egypro.2017.03.301.

[99] X. Wei, H. Zhu, T. Kong, and L. Wang, "Synthesis and thermal conductivity of Cu_2O nanofluids," *Int. J. Heat Mass Transf.*, vol. 52, no. 19–20, pp. 4371–4374, Sep. 2009, doi: 10.1016/j.ijheatmasstransfer.2009.03.073.

[100] S. Chakraborty, I. Sengupta, I. Sarkar, S. K. Pal, and S. Chakraborty, "Effect of surfactant on thermo-physical properties and spray cooling heat transfer performance of Cu-Zn-Al LDH nanofluid," *Appl. Clay Sci.*, vol. 168, pp. 43–55, Feb. 2019, doi: 10.1016/j.clay.2018.10.018.

[101] H. Zhu, C. Zhang, Y. Tang, J. Wang, B. Ren, and Y. Yin, "Preparation and thermal conductivity of suspensions of graphite nanoparticles," *Carbon N. Y.*, vol. 45, no. 1, pp. 226–228, Jan. 2007, doi: 10.1016/j.carbon.2006.07.005.

[102] D.-W. Oh, A. Jain, J. K. Eaton, K. E. Goodson, and J. S. Lee, "Thermal conductivity measurement and sedimentation detection of aluminum oxide nanofluids by using the 3ω method," *Int. J. Heat Fluid Flow*, vol. 29, no. 5, pp. 1456–1461, Oct. 2008, doi: 10.1016/j.ijheatfluidflow.2008.04.007.

[103] M. Zimbone, L. Calcagno, G. Messina, P. Baeri, and G. Compagnini, "Dynamic light scattering and UV–vis spectroscopy of gold nanoparticles solution," *Mater. Lett.*, vol. 65, no. 19–20, pp. 2906–2909, Oct. 2011, doi: 10.1016/j.matlet.2011.06.054.

[104] H. Akhavan-Zanjani, M. Saffar-Avval, M. Mansourkiaei, F. Sharif, and M. Ahadi, "Experimental investigation of laminar forced convective heat transfer of Graphene-water nanofluid inside a circular tube," *International Journal of Thermal Sciences*, vol. 100, pp. 316–323, 2016, doi: 10.1016/j.ijthermalsci.2015.10.003.

[105] M. Mehrali *et al.*, "Heat transfer and entropy generation analysis of hybrid graphene/Fe_3O_4 ferro-nanofluid flow under the influence of a magnetic field," *Powder Technol.*, vol. 308, pp. 149–157, Feb. 2017, doi: 10.1016/j.powtec.2016.12.024.

[106] M. Mehrali *et al.*, "Preparation, characterization, viscosity, and thermal conductivity of nitrogen-doped graphene aqueous nanofluids," *J. Mater. Sci.*, vol. 49, no. 20, pp. 7156–7171, Oct. 2014, doi: 10.1007/s10853-014-8424-8.

[107] S. A. Angayarkanni and J. Philip, "Review on thermal properties of nanofluids: Recent developments," *Adv. Colloid Interface Sci.*, vol. 225, pp. 146–176, Nov. 2015, doi: 10.1016/j.cis.2015.08.014.

[108] H. M. Ali and W. Arshad, "Effect of channel angle of pin-fin heat sink on heat transfer performance using water based graphene nanoplatelets nanofluids," *Int. J. Heat Mass Transf.*, vol. 106, pp. 465–472, Mar. 2017, doi: 10.1016/J.IJHEATMASSTRANSFER.2016.08.061.

[109] G. D. Xia, R. Liu, J. Wang, and M. Du, "The characteristics of convective heat transfer in microchannel heat sinks using Al_2O_3 and TiO_2 nanofluids," *International Communications in Heat and Mass Transfer*, vol. 76, pp. 256–264, Aug. 2016, doi: 10.1016/j.icheatmasstransfer.2016.05.034.

[110] T. Tharayil, L. G. Asirvatham, V. Ravindran, and S. Wongwises, "Thermal performance of miniature loop heat pipe with graphene-water nanofluid," *Int. J. Heat Mass Transf.*, vol. 93, pp. 957–968, 2016, doi: 10.1016/j.ijheatmasstransfer.2015.11.011.

[111] L. G. Asirvatham, B. Raja, D. Mohan Lal, and S. Wongwises, "Convective heat transfer of nanofluids with correlations," *Particuology*, vol. 9, no. 6, pp. 626–631, Dec. 2011, doi: 10.1016/j.partic.2011.03.014.

[112] L. Yang and Y. Hu, "Toward TiO_2 Nanofluids—Part 2: Applications and Challenges," *Nanoscale Res. Lett.*, vol. 12, no. 1, p. 446, Dec. 2017, doi: 10.1186/s11671-017-2185-7.

[113] A. Amiri, M. Shanbedi, B. T. Chew, S. N. Kazi, and K. H. Solangi, "Toward improved engine performance with crumpled nitrogen-doped graphene based water–ethylene glycol coolant," *Chemical Engineering Journal*, vol. 289, pp. 583–595, Apr. 2016, doi: 10.1016/J.CEJ.2015.12.083.

[114] R. R. Sahoo and J. Sarkar, "Heat transfer performance characteristics of hybrid nanofluids as coolant in louvered fin automotive radiator," *Heat and Mass Transfer*, vol. 53, no. 6, pp. 1923–1931, Jun. 2017, doi: 10.1007/s00231-016-1951-x.

[115] N. Ahammed, L. G. Asirvatham, and S. Wongwises, "Entropy generation analysis of graphene–alumina hybrid nanofluid in multiport minichannel heat exchanger coupled with thermoelectric cooler," *Int. J. Heat Mass Transf.*, vol. 103, pp. 1084–1097, 2016, doi: 10.1016/j.ijheatmasstransfer.2016.07.070.

[116] M. S. Yılmaz, M. Ünverdi, H. Kücük, N. Akcakale, and F. Halıcı, "Enhancement of heat transfer in shell and tube heat exchanger using mini-channels and nanofluids: An experimental study," *International Journal of Thermal Sciences*, vol. 179, p. 107664, Sep. 2022, doi: 10.1016/j.ijthermalsci.2022.107664.

[117] R. Ranjbarzadeh, A. H. Meghdadi Isfahani, M. Afrand, A. Karimipour, and M. Hojaji, "An experimental study on heat transfer and pressure drop of water/graphene oxide nanofluid in a copper tube under air cross-flow: Applicable as a heat exchanger," *Appl. Therm. Eng.*, vol. 125, pp. 69–79, 2017, doi: 10.1016/j.applthermaleng.2017.06.110.

[118] R. Ranjbarzadeh, A. Karimipour, M. Afrand, A. H. M. Isfahani, and A. Shirneshan, "Empirical analysis of heat transfer and friction factor of water/graphene oxide nanofluid flow in turbulent regime through an isothermal pipe," *Appl. Therm. Eng.*, vol. 126, pp. 538–547, 2017, doi: 10.1016/j.applthermaleng.2017.07.189.

[119] C. Selvam, T. Balaji, D. Mohan Lal, and S. Harish, "Convective heat transfer coefficient and pressure drop of water-ethylene glycol mixture with graphene nanoplatelets," *Exp. Therm. Fluid Sci.*, vol. 80, pp. 67–76, 2017, doi: 10.1016/j.expthermflusci.2016.08.013.

[120] N. Zuber and Novak, "Hydrodynamic Aspects Of Boiling Heat Transfer (Thesis)," Oak Ridge, TN, Jun. 1959. doi: 10.2172/4175511.

[121] S. D. Park *et al.*, "Effects of nanofluids containing graphene/graphene-oxide nanosheets on critical heat flux," *Appl. Phys. Lett.*, vol. 97, no. 2, p. 023103, Jul. 2010, doi: 10.1063/1.3459971.

[122] D. Wen and Y. Ding, "Experimental investigation into the pool boiling heat transfer of aqueous based γ-alumina nanofluids," *Journal of Nanoparticle Research*, vol. 7, no. 2–3, pp. 265–274, Jun. 2005, doi: 10.1007/s11051-005-3478-9.

[123] B. A. J. Rose *et al.*, "Investigations into nanofluids as direct solar radiation collectors," *Solar Energy*, vol. 147, pp. 426–431, 2017, doi: 10.1016/j.solener.2017.03.063.

[124] Y. Li, H. Q. Xie, W. Yu, and J. Li, "Investigation on Heat Transfer Performances of Nanofluids in Solar Collector," *Materials Science Forum*, vol. 694, pp. 33–36, Jul. 2011, doi: 10.4028/www.scientific.net/MSF.694.33.

[125] G. Sadeghi, S. Nazari, M. Ameri, and F. Shama, "Energy and exergy evaluation of the evacuated tube solar collector using Cu_2O/water nanofluid utilizing ANN methods," *Sustainable Energy Technologies and Assessments*, vol. 37, p. 100578, Feb. 2020, doi: 10.1016/j.seta.2019.100578.

[126] S. Choudhary, A. Sachdeva, and P. Kumar, "Investigation of the stability of MgO nanofluid and its effect on the thermal performance of flat plate solar collector," *Renew. Energy*, vol. 147, pp. 1801–1814, Mar. 2020, doi: 10.1016/j.renene.2019.09.126.

[127] M. R. Saffarian, M. Moravej, and M. H. Doranehgard, "Heat transfer enhancement in a flat plate solar collector with different flow path shapes using nanofluid," *Renew. Energy*, vol. 146, pp. 2316–2329, Feb. 2020, doi: 10.1016/j.renene.2019.08.081.

[128] S. M. Parsa, A. Rahbar, M. H. Koleini, S. Aberoumand, M. Afrand, and M. Amidpour, "A renewable energy-driven thermoelectric-utilized solar still with external condenser loaded by silver/nanofluid for simultaneously water disinfection and desalination," *Desalination*, vol. 480, p. 114354, Apr. 2020, doi: 10.1016/j.desal.2020.114354.

[129] P. D. Shima, J. Philip, and B. Raj, "Influence of aggregation on thermal conductivity in stable and unstable nanofluids," *Appl. Phys. Lett.*, vol. 97, no. 15, p. 153113, Oct. 2010, doi: 10.1063/1.3497280.

[130] J. W. Gao, R. T. Zheng, H. Ohtani, D. S. Zhu, and G. Chen, "Experimental investigation of heat conduction mechanisms in nanofluids. Clue on clustering," *Nano Lett.*, vol. 9, no. 12, pp. 4128–4132, Dec. 2009, doi: 10.1021/nl902358m.

[131] C. Wu, T. J. Cho, J. Xu, D. Lee, B. Yang, and M. R. Zachariah, "Effect of nanoparticle clustering on the effective thermal conductivity of concentrated silica colloids," *Phys. Rev. E Stat. Nonlin. Soft Matter Phys.*, vol. 81, no. 1, p. 011406, Jan. 2010, doi: 10.1103/PhysRevE.81.011406.

[132] I. Khoswan, H. Nassar, M. Assali, A. AbuSafa, S. Sawalha, and H. S. Hilal, "Why Carbon Nanotubes Improve Aqueous Nanofluid Thermal Conductivity: A Qualitative Model Critical Review," *Processes*, vol. 12, no. 4, p. 834, Apr. 2024, doi: 10.3390/pr12040834.

[133] X. Shao, Y. Chen, S. Mo, Z. Cheng, and T. Yin, "Dispersion Stability of TiO_2-H_2O Nanofluids Containing Mixed Nanotubes and Nanosheets," *Energy Procedia*, vol. 75, pp. 2049–2054, Aug. 2015, doi: 10.1016/j.egypro.2015.07.282.

[134] H. Chen, Y. Ding, A. Lapkin, and X. Fan, "Rheological behaviour of ethylene glycol-titanate nanotube nanofluids," *Journal of Nanoparticle Research*, vol. 11, no. 6, pp. 1513–1520, Aug. 2009, doi: 10.1007/s11051-009-9599-9.

[135] N. L. N. Yusof, H. S. Shamsuddin, P. Estellé, and N. Mohd-Ghazali, "Optimization of a boron nitride nanotubes nanofluid-cooled microchannel heat sink at different concentrations," *Journal of Thermal Analysis and Calorimetry 2022 148:8*, vol. 148, no. 8, pp. 3117–3127, Sep. 2022, doi: 10.1007/S10973-022-11545-8.

[136] M. O. Kluger *et al.*, "A new attraction-detachment model for explaining flow sliding in clay-rich tephras," *Geology*, vol. 45, no. 2, pp. 131–134, Feb. 2017, doi: 10.1130/G38560.1.

[137] P. Yuan *et al.*, "Functionalization of halloysite clay nanotubes by grafting with γ-aminopropyltriethoxysilane," *Journal of Physical Chemistry C*, vol. 112, no. 40, pp. 15742–15751, Oct. 2008, doi: 10.1021/jp805657t.

[138] P. Yuan, D. Tan, and F. Annabi-Bergaya, “Properties and applications of halloysite nanotubes: recent research advances and future prospects,” *Appl. Clay Sci.*, vol. 112–113, pp. 75–93, Aug. 2015, doi: 10.1016/j.clay.2015.05.001.

[139] D. Tan, P. Yuan, D. Liu, and P. Du, “Surface Modifications of Halloysite,” in *Developments in Clay Science*, vol. 7, Elsevier B.V., 2016, pp. 167–201. doi: 10.1016/B978-0-08-100293-3.00008-X.

[140] S. Yang *et al.*, “Preparation and characterization of non-solvent halloysite nanotubes nanofluids,” *Appl. Clay Sci.*, vol. 126, pp. 215–222, Jun. 2016, doi: 10.1016/j.clay.2016.03.018.

[141] P. Du *et al.*, “Controlling the macroscopic liquid-like behaviour of halloysite-based solvent-free nanofluids via a facile core pretreatment,” *Appl. Clay Sci.*, vol. 156, pp. 126–133, May 2018, doi: 10.1016/j.clay.2018.01.037.

[142] D. G. Shchukin, G. B. Sukhorukov, R. R. Price, and Y. M. Lvov, “Halloysite nanotubes as biomimetic nanoreactors,” *Small*, vol. 1, no. 5, pp. 510–513, May 2005, doi: 10.1002/smll.200400120.

[143] X. Li, QianYang, J. Ouyang, H. Yang, and S. Chang, “Chitosan modified halloysite nanotubes as emerging porous microspheres for drug carrier,” *Appl. Clay Sci.*, vol. 126, pp. 306–312, Jun. 2016, doi: 10.1016/j.clay.2016.03.035.

[144] I. Deen, X. Pang, and I. Zhitomirsky, “Electrophoretic deposition of composite chitosan-halloysite nanotube-hydroxyapatite films,” *Colloids Surf. A Physicochem. Eng. Asp.*, vol. 410, pp. 38–44, Sep. 2012, doi: 10.1016/j.colsurfa.2012.06.011.

[145] J. Wang and W. Azam, “Natural resource scarcity, fossil fuel energy consumption, and total greenhouse gas emissions in top emitting countries,” *Geoscience Frontiers*, vol. 15, no. 2, p. 101757, Mar. 2024, doi: 10.1016/J.GSF.2023.101757.

[146] C. Popescu, E. Hysa, M. Panait, and A. Çela, “Past, Present, and Future of Critical Issues in Energy: Poverty, Transition and Security—A Systematic Review,” *Energies (Basel).*, vol. 16, no. 14, p. 5484, Jul. 2023, doi: 10.3390/en16145484.

[147] L. Xiao *et al.*, “A Review of Pool-Boiling Processes Based on Bubble-Dynamics Parameters,” *Applied Sciences*, vol. 13, no. 21, p. 12026, Nov. 2023, doi: 10.3390/app132112026.

[148] G. Liang and I. Mudawar, “Review of single-phase and two-phase nanofluid heat transfer in macro-channels and micro-channels,” *Int. J. Heat Mass Transf.*, vol. 136, pp. 324–354, Jun. 2019, doi: 10.1016/j.ijheatmasstransfer.2019.02.086.

[149] Yu Min Yang and Jer Ru Maa, “Boiling of suspension of solid particles in water,” *Int. J. Heat Mass Transf.*, vol. 27, no. 1, pp. 145–147, Jan. 1984, doi: 10.1016/0017-9310(84)90248-5.

[150] S. K. Das, N. Putra, and W. Roetzel, “Pool boiling of nano-fluids on horizontal narrow tubes,” *International Journal of Multiphase Flow*, vol. 29, no. 8, pp. 1237–1247, Aug. 2003, doi: 10.1016/S0301-9322(03)00105-8.

[151] M. M. Sarafraz and F. Hormozi, “Experimental investigation on the pool boiling heat transfer to aqueous multi-walled carbon nanotube nanofluids on the micro-finned surfaces,” *International Journal of Thermal Sciences*, vol. 100, pp. 255–266, Feb. 2016, doi: 10.1016/j.ijthermalsci.2015.10.006.

[152] Y. He, H. Li, Y. Hu, X. Wang, and J. Zhu, “Boiling heat transfer characteristics of ethylene glycol and water mixture based ZnO nanofluids in a cylindrical vessel,” *Int. J. Heat Mass Transf.*, vol. 98, pp. 611–615, Jul. 2016, doi: 10.1016/j.ijheatmasstransfer.2016.03.052.

[153] E. Akbari, A. M. Gheitaghy, H. Saffari, and S. M. Hosseinalipour, “Effect of silver nanoparticle deposition in re-entrant inclined minichannel on bubble dynamics for pool boiling enhancement,” *Exp. Therm. Fluid Sci.*, vol. 82, pp. 390–401, Apr. 2017, doi: 10.1016/J.EXPTHERMFLUSCI.2016.11.037.

[154] L. L. Manetti, M. T. Stephen, P. A. Beck, and E. M. Cardoso, “Evaluation of the heat transfer enhancement during pool boiling using low concentrations of Al_2O_3-water based nanofluid,” *Exp. Therm. Fluid Sci.*, vol. 87, pp. 191–200, Oct. 2017, doi: 10.1016/j.expthermflusci.2017.04.018.

[155] M. R. Salimpour, A. Abdollahi, and M. Afrand, “An experimental study on deposited surfaces due to nanofluid pool boiling: Comparison between rough and smooth surfaces,” *Exp. Therm. Fluid Sci.*, vol. 88, pp. 288–300, Nov. 2017, doi: 10.1016/j.expthermflusci.2017.06.007.

[156] M. Karimzadehkhouei, M. Shojaeian, K. Şendur, M. P. Mengüç, and A. Koşar, “The effect of nanoparticle type and nanoparticle mass fraction on heat transfer enhancement in pool boiling,” *Int. J. Heat Mass Transf.*, vol. 109, Jun. 2017, doi: 10.1016/j.ijheatmasstransfer.2017.01.116.

[157] M. Kole and T. K. Dey, “Investigations on the pool boiling heat transfer and critical heat flux of ZnO-ethylene glycol nanofluids,” *Appl. Therm. Eng.*, vol. 37, pp. 112–119, May 2012, doi: 10.1016/j.applthermaleng.2011.10.066.

[158] M. S. Kamel, F. Lezsovits, A. Abdollahi, and M. Izadi, “Amelioration of pool boiling thermal performance in case of using a new hybrid nanofluid,” *Case Studies in Thermal Engineering*, vol. 24, p. 100872, Apr. 2021, doi: 10.1016/J.CSITE.2021.100872.

[159] M. F. Nabil, W. H. Azmi, K. A. Hamid, N. N. M. Zawawi, G. Priyandoko, and R. Mamat, “Thermo-physical properties of hybrid nanofluids and hybrid nanolubricants: A comprehensive review on performance,” *International Communications in Heat and Mass Transfer*, vol. 83, pp. 30–39, Apr. 2017, doi: 10.1016/j.icheatmasstransfer.2017.03.008.

[160] R. B. Ganvir, P. V. Walke, and V. M. Kriplani, “Heat transfer characteristics in nanofluid—A review,” *Renewable and Sustainable Energy Reviews*, vol. 75, pp. 451–460, Aug. 2017, doi: 10.1016/j.rser.2016.11.010.

[161] Z. H. Han, B. Yang, S. H. Kim, and M. R. Zachariah, “Application of hybrid sphere/carbon nanotube particles in nanofluids,” *Nanotechnology*, vol. 18, no. 10, Mar. 2007, doi: 10.1088/0957-4484/18/10/105701.

[162] S. Suresh, K. P. Venkitaraj, P. Selvakumar, and M. Chandrasekar, “Synthesis of Al_2O_3–Cu/water hybrid nanofluids using two step method and its thermo physical properties,” *Colloids Surf. A Physicochem. Eng. Asp.*, vol. 388, no. 1–3, pp. 41–48, Sep. 2011, doi: 10.1016/j.colsurfa.2011.08.005.

[163] D. Madhesh and S. Kalaiselvam, “Experimental analysis of hybrid nanofluid as a coolant,” in *Procedia Engineering*, Elsevier Ltd, Jan. 2014, pp. 1667–1675. doi: 10.1016/j.proeng.2014.12.317.

[164] M. Hemmat Esfe, A. A. Abbasian Arani, M. Rezaie, W. M. Yan, and A. Karimipour, “Experimental determination of thermal conductivity and dynamic viscosity of Ag-MgO/water hybrid nanofluid,” *International Communications in Heat and Mass Transfer*, vol. 66, pp. 189–195, Aug. 2015, doi: 10.1016/j.icheatmasstransfer.2015.06.003.

[165] O. Soltani and M. Akbari, “Effects of temperature and particles concentration on the dynamic viscosity of MgO-MWCNT/ethylene glycol hybrid nanofluid: Experimental study,” *Physica E Low. Dimens. Syst. Nanostruct.*, vol. 84, pp. 564–570, 2016, doi: 10.1016/j.physe.2016.06.015.

[166] M. Afrand, D. Toghraie, and B. Ruhani, “Effects of temperature and nanoparticles concentration on rheological behavior of Fe_3O_4–Ag/EG hybrid nanofluid: An experimental study,” *Exp. Therm. Fluid Sci.*, vol. 77, pp. 38–44, Oct. 2016, doi: 10.1016/j.expthermflusci.2016.04.007.

[167] A. A. Minea, “Hybrid nanofluids based on Al_2O_3, TiO_2 and SiO_2: Numerical evaluation of different approaches,” *Int. J. Heat Mass Transf.*, vol. 104, pp. 852–860, Jan. 2017, doi: 10.1016/j.ijheatmasstransfer.2016.09.012.

[168] M. Bahrami, M. Akbari, A. Karimipour, and M. Afrand, “An experimental study on rheological behavior of hybrid nanofluids made of iron and copper oxide in a binary mixture of water and ethylene glycol: Non-Newtonian behavior,” *Exp. Therm. Fluid Sci.*, vol. 79, pp. 231–237, Dec. 2016, doi: 10.1016/j.expthermflusci.2016.07.015.

[169] H. Maleki, M. R. Safaei, A. A. A. A. Alrashed, and A. Kasaeian, “Flow and heat transfer in non-Newtonian nanofluids over porous surfaces,” *J. Therm. Anal. Calorim.*, vol. 135, no. 3, pp. 1655–1666, Feb. 2019, doi: 10.1007/s10973-018-7277-9.

[170] L. S. Sundar, M. H. Farooky, S. N. Sarada, and M. K. Singh, “Experimental thermal conductivity of ethylene glycol and water mixture based low volume concentration of Al_2O_3 and CuO nanofluids,” *International Communications in Heat and Mass Transfer*, vol. 41, pp. 41–46, Feb. 2013, doi: 10.1016/j.icheatmasstransfer.2012.11.004.

[171] I. Zakaria, W. H. Azmi, W. A. N. W. Mohamed, R. Mamat, and G. Najafi, “Experimental Investigation of Thermal Conductivity and Electrical Conductivity of Al_2O_3 Nanofluid in Water - Ethylene Glycol Mixture for Proton Exchange Membrane Fuel Cell Application,”

International Communications in Heat and Mass Transfer, vol. 61, pp. 61–68, Feb. 2015, doi: 10.1016/j.icheatmasstransfer.2014.12.015.

[172] F. S. Javadi *et al.*, “The effects of nanofluid on thermophysical properties and heat transfer characteristics of a plate heat exchanger,” *International Communications in Heat and Mass Transfer*, vol. 44, pp. 58–63, May 2013, doi: 10.1016/j.icheatmasstransfer.2013.03.017.

[173] G. Paul, J. Philip, B. Raj, P. K. Das, and I. Manna, “Synthesis, characterization, and thermal property measurement of nano-$Al_{95}Zn_{05}$ dispersed nanofluid prepared by a two-step process,” *Int. J. Heat Mass Transf.*, vol. 54, no. 15–16, pp. 3783–3788, Jul. 2011, doi: 10.1016/j.ijheatmasstransfer.2011.02.044.

[174] K. A. Hamid, W. H. Azmi, M. F. Nabil, and R. Mamat, “Experimental investigation of nanoparticle mixture ratios on TiO_2–SiO_2 nanofluids heat transfer performance under turbulent flow,” *Int. J. Heat Mass Transf.*, vol. 118, pp. 617–627, Mar. 2018, doi: 10.1016/j.ijheatmasstransfer.2017.11.036.

[175] K. A. Hamid, W. H. Azmi, M. F. Nabil, R. Mamat, and K. V. Sharma, “Experimental investigation of thermal conductivity and dynamic viscosity on nanoparticle mixture ratios of TiO_2-SiO_2 nanofluids,” *Int. J. Heat Mass Transf.*, vol. 116, pp. 1143–1152, Jan. 2018, doi: 10.1016/j.ijheatmasstransfer.2017.09.087.

[176] H. Yu and W. Feng, “Carbon-Based Multifunctional Nanomaterials,” *Nanomaterials*, vol. 14, no. 19, p. 1600, Oct. 2024, doi: 10.3390/nano14191600.

[177] Y. Yao, J. Xu, Y. Huang, and T. Zhang, “Synthesis and applications of carbon nanospheres: A review,” *Particuology*, vol. 87, pp. 325–338, Apr. 2024, doi: 10.1016/j.partic.2023.09.007.

[178] Y. Wang, F. Su, C. D. Wood, J. Y. Lee, and X. S. Zhao, “Preparation and characterization of carbon nanospheres as anode materials in lithium-ion secondary batteries,” *Ind. Eng. Chem. Res.*, vol. 47, no. 7, pp. 2294–2300, Apr. 2008, doi: 10.1021/ie071337d.

[179] Y. P. Sun *et al.*, “Quantum-sized carbon dots for bright and colorful photoluminescence,” *J. Am. Chem. Soc.*, vol. 128, no. 24, pp. 7756–7757, Jun. 2006, doi: 10.1021/ja062677d.

[180] L. Cao *et al.*, “Carbon dots for multiphoton bioimaging,” *J. Am. Chem. Soc.*, vol. 129, no. 37, pp. 11318–11319, Sep. 2007, doi: 10.1021/ja073527l.

[181] Y. Z. Jin *et al.*, “Large-scale synthesis and characterization of carbon spheres prepared by direct pyrolysis of hydrocarbons,” *Carbon N. Y.*, vol. 43, no. 9, pp. 1944–1953, Aug. 2005, doi: 10.1016/j.carbon.2005.03.002.

[182] V. G. Pol, M. Motiei, A. Gedanken, J. Calderon-Moreno, and M. Yoshimura, “Carbon spherules: Synthesis, properties and mechanistic elucidation,” *Carbon N. Y.*, vol. 42, no. 1, pp. 111–116, Jan. 2004, doi: 10.1016/j.carbon.2003.10.005.

[183] Ph. Serp, R. Feurer, Ph. Kalck, Y. Kihn, J. L. Faria, and J. L. Figueiredo, “A chemical vapour deposition process for the production of carbon nanospheres,” *Carbon N. Y.*, vol. 39, no. 4, pp. 621–626, Apr. 2001, doi: 10.1016/S0008-6223(00)00324-9.

[184] X. Ma *et al.*, “Easy nickel substrate-assisted growth of uniform carbon microspheres and their spectroscopic properties,” *Carbon N. Y.*, vol. 44, no. 13, pp. 2861–2864, Nov. 2006, doi: 10.1016/j.carbon.2006.06.007.

[185] Z. Zhou, Q. Yan, F. Su, and X. S. Zhao, “Replicating novel carbon nanostructures with 3D macroporous silica template,” *J. Mater. Chem.*, vol. 15, no. 26, pp. 2569–2574, Jun. 2005, doi: 10.1039/b503691g.

[186] L. Tosheva, J. Parmentier, V. Valtchev, C. Vix-Guterl, and J. Patarin, “Carbon spheres prepared from zeolite Beta beads,” *Carbon N. Y.*, vol. 43, no. 12, pp. 2474–2480, Oct. 2005, doi: 10.1016/j.carbon.2005.04.030.

[187] B. J. Kim and J. Y. Chang, “Preparation of carbon nanospheres from diblock copolymer micelles with cores containing curable acetylenic groups,” *Macromolecules*, vol. 39, no. 1, pp. 90–94, Jan. 2006, doi: 10.1021/ma051713a.

[188] Z. Liang *et al.*, “Soft-template assisted hydrothermal synthesis of size-tunable, N-doped porous carbon spheres for supercapacitor electrodes,” *Results Phys.*, vol. 12, pp. 1984–1990, Mar. 2019, doi: 10.1016/J.RINP.2019.01.074.

[189] H. K. Versteeg and W. Malalasekera, *An Introduction to Computational Fluid Dynamics: The Finite Volume Method*. Pearson Education, 2007.

[190] B. Joseph, *Application des potentiels à l'étude de l'équilibre et du mouvement des solides élastiques: principalement au calcul des déformations et des pressions que produisent, dans ces solides, des efforts quelconques exercés sur une petite partie de leur surface ou de leur intérieur: mémoire suivi de notes étendues sur divers points de physique, mathematique et d'analyse*, vol. 4. Gauthier-Villars, 1885.

[191] A. M. Hussein, K. V. Sharma, R. A. Bakar, and K. Kadirgama, "The effect of cross sectional area of tube on friction factor and heat transfer nanofluid turbulent flow," *International Communications in Heat and Mass Transfer*, vol. 47, pp. 49–55, Oct. 2013, doi: 10.1016/j.icheatmasstransfer.2013.06.007.

[192] A. M. Hussein, R. A. Bakar, and K. Kadirgama, "Study of forced convection nanofluid heat transfer in the automotive cooling system," *Case Studies in Thermal Engineering*, vol. 2, pp. 50–61, Mar. 2014, doi: 10.1016/j.csite.2013.12.001.

[193] S. Mosayebidorcheh, M. Sheikholeslami, M. Hatami, and D. D. Ganji, "Analysis of turbulent MHD Couette nanofluid flow and heat transfer using hybrid DTM-FDM," *Particuology*, vol. 26, pp. 95–101, Jun. 2016, doi: 10.1016/j.partic.2016.01.002.

[194] S. M. Abbasi, A. Rashidi, A. Nemati, and K. Arzani, "The effect of functionalisation method on the stability and the thermal conductivity of nanofluid hybrids of carbon nanotubes/gamma alumina," *Ceram. Int.*, vol. 39, no. 4, pp. 3885–3891, May 2013, doi: 10.1016/j.ceramint.2012.10.232.

[195] M. Nuim Labib, M. J. Nine, H. Afrianto, H. Chung, and H. Jeong, "Numerical investigation on effect of base fluids and hybrid nanofluid in forced convective heat transfer," *International Journal of Thermal Sciences*, vol. 71, pp. 163–171, Sep. 2013, doi: 10.1016/j.ijthermalsci.2013.04.003.

[196] L. S. Sundar, M. K. Singh, and A. C. M. Sousa, "Enhanced heat transfer and friction factor of MWCNT–Fe_3O_4/water hybrid nanofluids," *International Communications in Heat and Mass Transfer*, vol. 52, pp. 73–83, Mar. 2014, doi: 10.1016/j.icheatmasstransfer.2014.01.012.

[197] M. Sotsu, "Friction factor and Reynolds number correlation for finned tube bundle of the air cooler of Monju reactor," *Nuclear Engineering and Design*, vol. 396, p. 111893, Sep. 2022, doi: 10.1016/j.nucengdes.2022.111893.

[198] W. M. Rohsenow, J. R. Hartnett, and Y. I. Cho, *Handbook of Heat Transfer*. New York: McGraw-Hill, 1998.

[199] P. W. Dittus and L. M. K. Boelter, *Heat Transfer in Automobile Radiators of the Tubular Type* , vol. 2/13. Univ. Calif. Pub. Eng., 1930.

[200] A. P. Colburn, "A method of correlating forced convection heat-transfer data and a comparison with fluid friction," *Int. J. Heat Mass Transf.*, vol. 7, no. 12, pp. 1359–1384, Dec. 1964, doi: 10.1016/0017-9310(64)90125-5.

[201] D. Roger E and M. William H, "Heat-Transfer Coefficients for Air Flowing in Round Tubes, in Rectangular Ducts, and Around Finned Cylinders," *Wartime Report*, vol. W-108, 1945.

[202] V. Gnielinski, "New Equations for Heat and Mass Transfer in Turbulent Pipe and Channel Flow," *Int. Chem. Eng.*, vol. 16, pp. 359–368, 1976.

[203] E. N. Sieder and G. E. Tate, "Heat Transfer and Pressure Drop of Liquids in Tubes," *Ind. Eng. Chem.*, vol. 28, no. 12, pp. 1429–1435, Dec. 2002, doi: 10.1021/IE50324A027.

[204] H. Hausen, "Neue Gleichungen fur die Warmeübertragung bei freier oder erzwungener Stromung," *Allg. Warmetchn.*, vol. 9, pp. 75–79, 1959.

[205] V. Kármán, "The Analogy Between Fluid Friction and Heat Transfer," *Trans. ASME*, vol. 61, pp. 705–710, 1939.

[206] L. Prandtl, *Führrer durch die Stömungslehre*. Braunschweig: Vieweg, 1944.

[207] W. L. Friend and A. B. Metzner, "Turbulent heat transfer inside tubes and the analogy among heat, mass, and momentum transfer," *AIChE Journal*, vol. 4, no. 4, pp. 393–402, Dec. 1958, doi: 10.1002/aic.690040404.

[208] B. S. Petukhov and V. V. Kirillov, "The Problem of Heat Exchange in the Turbulent Flow of Liquids in Tubes, (in Russian)," *Teploenergetika*, vol. 4, pp. 63–68, 1958.

[209] R. L. Webb, "A critical evaluation of analytical solutions and reynolds analogy equations for turbulent heat and mass transfer in smooth tubes," *Wärme- und Stoffübertragung*, vol. 4, no. 4, pp. 197–204, Dec. 1971, doi: 10.1007/BF01002474.

[210] O. C. Sandall, O. T. Hanna, and P. R. Mazet, “A New Theoretical Formula for Turbulent Heat and Mass Transfer with Gases or Liquids in Tube Row,” *Can. J. Chem. Eng.*, vol. 58, pp. 443–447, 1980.

[211] H. Blasius, “Das Ähnlichkeitsgesetz bei Reibungsvorgängen in Flüssigkeiten,” *Forschg. Arb. Ing.Wes.*, vol. 131, 1913.

[212] T. B. Drew, E. C. Koo, and W. H. McAdams, “The friction factor for clean round pipes,” *Trans. AIChE*, vol. 28, pp. 56–72, 1932.

[213] M. S. Bhatti and R. K. Shah, “Turbulent and Transition Flow Convective Heat Transfer in Ducts,” in *Handbook of Single-Phase Convective Heat Transfer*, S. Kakac, R. K. Shah, and W. Aung, Eds., New York: Wiley-Interscience, 1987.

[214] J. Nikuradse, “Gesetzmässigkeiten der turbulenten Strömung in glatten Rohren,” *Forsh. Arb. Ing. Wes.*, vol. 356, 1932.

[215] C. F. Colebrook, “Turbulent Flow in Pipes with Particular Reference to the Transition Region between the Smooth and Rough Pipes Laws,” *J. Inst. Civil Eng.*, vol. 11, pp. 133–156, 1939.

[216] G. K. Filonenko, “Hydraulic Resistance in Pipes (in Russia),” *Teplonergetika*, vol. 1/4, pp. 40–44, 1954.

[217] R. Techo, R. R. Tickner, and R. E. James, “An Accurate Equation for the Computation of the Friction Factor for Smooth Pipes From the Reynolds Number,” *J. Appl. Mech.*, vol. 32, no. 2, pp. 443–443, Jun. 1965, doi: 10.1115/1.3625826.

[218] S. Saedodin, M. Zaboli, and S. S. Mousavi Ajarostaghi, “Hydrothermal analysis of heat transfer and thermal performance characteristics in a parabolic trough solar collector with Turbulence-Inducing elements,” *Sustainable Energy Technologies and Assessments*, vol. 46, p. 101266, Aug. 2021, doi: 10.1016/J.SETA.2021.101266.

[219] A. A. Deshmukh, S. D. Mhlanga, and N. J. Coville, “Carbon spheres,” *Materials Science and Engineering R: Reports*, vol. 70, no. 1–2, pp. 1–28, 2010, doi: 10.1016/j.mser.2010.06.017.

[220] L. P. Bakos *et al.*, “Core-shell carbon nanosphere-TiO_2 composite and hollow TiO_2 nanospheres prepared by atomic layer deposition,” *J. Phys. Conf. Ser.*, vol. 764, no. 1, p. 012005, Oct. 2016, doi: 10.1088/1742-6596/764/1/012005.

[221] M. S. Kamel and F. Lezsovits, “Experimental Study on Pool Boiling Heat Transfer Performance of Magnesium Oxide Nanoparticles Based Water Nanofluid,” *Pollack Periodica*, vol. 15, no. 3, pp. 101–112, Nov. 2020, doi: 10.1556/606.2020.15.3.10.

[222] E. B. Elcioglu, “A High-Accuracy Thermal Conductivity Model for Water-Based Graphene Nanoplatelet Nanofluids,” *Energies (Basel).*, vol. 14, no. 16, p. 5178, Aug. 2021, doi: 10.3390/en14165178.

[223] P. C. Mukesh Kumar and R. Kavitha, “Regression analysis for thermal properties of Al_2O_3/H_2O nanofluid using machine learning techniques,” *Heliyon*, vol. 6, no. 6, p. e03966, Jun. 2020, doi: 10.1016/j.heliyon.2020.e03966.

[224] S. K. Mishra, H. Chandra, and A. Arora, “Effect of velocity and rheology of nanofluid on heat transfer of laminar vibrational flow through a pipe under constant heat flux,” *Int. Nano Lett.*, vol. 9, no. 3, pp. 245–256, Sep. 2019, doi: 10.1007/s40089-019-0276-4.

[225] H. Yan, P. Zhang, J. Li, X. L. Zhao, K. Zhang, and B. Zhang, “PEDOT/PSS-Halloysite Nanotubes (HNTs) Hybrid Films: Insulating HNTs Enhance Conductivity of the PEDOT/PSS Films,” *Sci. Rep.*, vol. 5, Dec. 2015, doi: 10.1038/srep18641.

[226] K. Tazaki, “Microbial formation of a halloysite-like mineral,” *Clays Clay Miner.*, vol. 53, no. 3, pp. 224–233, Jun. 2005, doi: 10.1346/CCMN.2005.0530303.

[227] E. Abdullayev, A. Joshi, W. Wei, Y. Zhao, and Y. Lvov, “Enlargement of halloysite clay nanotube lumen by selective etching of aluminum oxide,” *ACS Nano*, vol. 6, no. 8, pp. 7216–7226, Aug. 2012, doi: 10.1021/nn302328x.

[228] K. P. Nicolini, C. R. B. Fukamachi, F. Wypych, and A. S. Mangrich, “Dehydrated halloysite intercalated mechanochemically with urea: Thermal behavior and structural aspects,” *J. Colloid Interface Sci.*, vol. 338, no. 2, pp. 474–479, Oct. 2009, doi: 10.1016/j.jcis.2009.06.058.

[229] G. Tarì, I. Bobos, C. S. F. Gomes, and J. M. F. Ferreira, “Modification of surface charge properties during kaolinite to halloysite-7Å transformation,” *J. Colloid Interface Sci.*, vol. 210, no. 2, pp. 360–366, Feb. 1999, doi: 10.1006/jcis.1998.5917.

[230] R. L. Frost and J. Kristof, "Intercalation of halloysite: A raman spectroscopic study," *Clays Clay Miner.*, vol. 45, no. 4, pp. 551–563, Aug. 1997, doi: 10.1346/CCMN.1997.0450407.

[231] R. L. Frost, P. M. Fredericks, and J. R. Bartlett, "Fourier transform Raman spectroscopy of kandite clays," *Spectrochim. Acta A*, vol. 49, no. 5–6, pp. 667–674, May 1993, doi: 10.1016/0584-8539(93)80088-R.

[232] T. S. Gaaz, A. B. Sulong, A. A. H. Kadhum, M. H. Nassir, and A. A. Al-Amiery, "Impact of sulfuric acid treatment of halloysite on physico-chemic property modification," *Materials*, vol. 9, no. 8, Jul. 2016, doi: 10.3390/ma9080620.

[233] P. Yuan *et al.*, "Changes in structure, morphology, porosity, and surface activity of mesoporous halloysite nanotubes under heating," *Respir. Care*, vol. 58, no. 3, pp. 561–573, Mar. 2013, doi: 10.1346/CCMN.2012.0600602.

[234] P. M. Costanzo and R. F. Giese, "Ordered halloysite: dimethylsulfoxide intercalate.," *Clays Clay Miner.*, vol. 34, no. 1, pp. 105–107, 1986, doi: 10.1346/CCMN.1986.0340115.

[235] A. Zhang, Y. Zhang, and Z. Zhu, "Thermal properties of Halloysite nanotubes (HNTs) intercalation complexes-A review," *E3S Web of Conferences*, vol. 131, p. 01055, 2019, doi: 10.1051/E3SCONF/201913101055.

[236] S. K. Das, N. Putra, and W. Roetzel, "Pool boiling characteristics of nano-fluids," *Int. J. Heat Mass Transf.*, vol. 46, no. 5, pp. 851–862, Feb. 2003, doi: 10.1016/S0017-9310(02)00348-4.

[237] R. Kathiravan, R. Kumar, A. Gupta, and R. Chandra, "Characterization and pool boiling heat transfer studies of nanofluids," *J. Heat Transfer*, vol. 131, no. 8, pp. 1–8, Aug. 2009, doi: 10.1115/1.3111260.

[238] N. Shiro, "The maximum and minimum values of the heat q transmitted from metal to boiling water under atmospheric pressure," *Int. J. Heat Mass Transf.*, vol. 27, no. 7, pp. 959–970, Jul. 1984, doi: 10.1016/0017-9310(84)90112-1.

[239] T. Zhao, J. Chen, Y. Chen, Y. Zhang, and J. Peng, "Study on synergistic enhancement of oil recovery by halloysite nanotubes and glucose-based surfactants," *J. Dispers. Sci. Technol.*, vol. 42, no. 6, pp. 934–946, 2021, doi: 10.1080/01932691.2020.1721297.

[240] S. J. Kim, I. C. Bang, J. Buongiorno, and L. W. Hu, "Surface wettability change during pool boiling of nanofluids and its effect on critical heat flux," *Int. J. Heat Mass Transf.*, vol. 50, no. 19–20, pp. 4105–4116, Sep. 2007, doi: 10.1016/j.ijheatmasstransfer.2007.02.002.

[241] D. Mitra, P. Howli, B. K. Das, N. S. Das, P. Chattopadhyay, and K. K. Chattopadhyay, "Size and phase dependent thermal conductivity of TiO_2-water nanofluid with theoretical insight," *J. Mol. Liq.*, vol. 302, p. 112499, Mar. 2020, doi: 10.1016/J.MOLLIQ.2020.112499.

[242] Z. I. Várady *et al.*, "Experimental Investigation of Rheological Properties and Thermal Conductivity of SiO_2–TiO_2 Composite Nanofluids Prepared by Atomic Layer Deposition," *Nanomaterials*, vol. 12, no. 17, p. 3014, Aug. 2022, doi: 10.3390/nano12173014.

[243] K. Thangavelu, R. Annamalai, and D. Arulnandhi, "Preparation and Characterization of Nanosized TiO_2 Powder by Sol-Gel Precipitation Route," *International Journal of Emerging Technology and Advanced Engineering*, vol. 3, no. 1, pp. 636–639, 2013.

[244] R. Dong, L. Wang, J. Zhu, L. Liu, and Y. Qian, "A novel SiO_2–GO/acrylic resin nanocomposite: fabrication, characterization and properties," *Applied Physics A*, vol. 125, no. 8, p. 551, Aug. 2019, doi: 10.1007/s00339-019-2847-7.

[245] C. T. Nguyen *et al.*, "Temperature and particle-size dependent viscosity data for water-based nanofluids - Hysteresis phenomenon," *Int. J. Heat Fluid Flow*, vol. 28, no. 6, pp. 1492–1506, Dec. 2007, doi: 10.1016/j.ijheatfluidflow.2007.02.004.

[246] H. Chen and Y. Ding, "Heat Transfer and Rheological Behaviour of Nanofluids – A Review," Springer, Berlin, Heidelberg, 2009, pp. 135–177. doi: 10.1007/978-3-642-02690-4_3.

[247] "Entrance Length," Aerospace, Mechanical & Mechatronic Engg. Accessed: Jun. 07, 2021. [Online]. Available: http://www-mdp.eng.cam.ac.uk/web/library/enginfo/aerothermal_dvd_only/aero/fprops/pipeflow/node9.html

[248] W. Zhi-qing, "Study on correction coefficients of liminar and turbulent entrance region effect in round pipe," *Appl. Math. Mech.*, vol. 3, no. 3, pp. 433–446, Jun. 1982, doi: 10.1007/BF01897224.

[249] Y. A. Cengel, *Heat Transfer. A practical approach*, 2nd ed. McGraw-Hill, 2002.

[250] Y. Wang, R. Yang, M. Li, and Z. Zhao, “Hydrothermal preparation of highly porous carbon spheres from hemp (Cannabis sativa L.) stem hemicellulose for use in energy-related applications,” *Ind. Crops Prod.*, vol. 65, pp. 216–226, Mar. 2015, doi: 10.1016/j.indcrop.2014.12.008.

[251] F. B. Juangsa, Y. Muroya, M. Ryu, J. Morikawa, and T. Nozaki, “Comparative study of thermal conductivity in crystalline and amorphous nanocomposite,” *Appl. Phys. Lett.*, vol. 110, no. 25, p. 253105, Jun. 2017, doi: 10.1063/1.4986920.

[252] R. Mohammad and R. Kandasamy, “Nanoparticle shapes on electric and magnetic force in water, ethylene glycol and engine oil based Cu, Al_2O_3 and SWCNTs,” *J. Mol. Liq.*, vol. 237, pp. 54–64, Jul. 2017, doi: 10.1016/j.molliq.2017.04.045.

[253] M. Zhang, H. Yang, Y. Liu, X. Sun, D. Zhang, and D. Xue, “First identification of primary nanoparticles in the aggregation of HMF,” *Nanoscale Res. Lett.*, vol. 7, no. 1, p. 38, Jan. 2012, doi: 10.1186/1556-276X-7-38.

[254] M. Xue, Z. Zhan, M. Zou, L. Zhang, and S. Zhao, “Green synthesis of stable and biocompatible fluorescent carbon dots from peanut shells for multicolor living cell imaging,” *New Journal of Chemistry*, vol. 40, no. 2, pp. 1698–1703, Feb. 2016, doi: 10.1039/c5nj02181b.

[255] E. Kaçan and C. Kütahyali, “Adsorption of strontium from aqueous solution using activated carbon produced from textile sewage sludges,” *J. Anal. Appl. Pyrolysis*, vol. 97, pp. 149–157, 2012, doi: 10.1016/j.jaap.2012.06.006.

[256] R. C. De Andrade, C. F. De Almeida, A. B. De Siqueira, O. Treu-Filho, F. Caires, and C. T. De Carvalho, “Thermal and spectroscopic study of the 3,4-(methylenedioxy)cinnamate compounds of transition metals in the solid state,” *Thermochim. Acta*, vol. 596, pp. 56–62, Nov. 2014, doi: 10.1016/j.tca.2014.10.004.

[257] T. Kuila, A. K. Mishra, P. Khanra, N. H. Kim, and J. H. Lee, “Recent advances in the efficient reduction of graphene oxide and its application as energy storage electrode materials,” *Nanoscale*, vol. 5, no. 1, pp. 52–71, Jan. 2013, doi: 10.1039/c2nr32703a.

[258] M. Varga *et al.*, “Diamond/carbon nanotube composites: Raman, FTIR and XPS spectroscopic studies,” *Carbon N. Y.*, vol. 111, pp. 54–61, Jan. 2017, doi: 10.1016/j.carbon.2016.09.064.

[259] V. B. Mohan, L. Jakisch, K. Jayaraman, and D. Bhattacharyya, “Role of chemical functional groups on thermal and electrical properties of various graphene oxide derivatives: a comparative x-ray photoelectron spectroscopy analysis,” *Mater. Res. Express*, vol. 5, no. 3, p. 035604, Mar. 2018, doi: 10.1088/2053-1591/aab316.

[260] J. Wang, G. Li, T. Li, M. Zeng, and B. Sundén, “Effect of various surfactants on stability and thermophysical properties of nanofluids,” *J. Therm. Anal. Calorim.*, vol. 143, no. 6, pp. 4057–4070, Mar. 2021, doi: 10.1007/s10973-020-09381-9.

[261] X. Wang, X. Xu, and S. U. S. Choi, “Thermal conductivity of nanoparticle-fluid mixture,” *J. Thermophys. Heat Trans.*, vol. 13, no. 4, pp. 474–480, May 1999, doi: 10.2514/2.6486.

[262] E. Hatschek, “The general theory of viscosity of two-phase systems,” *Transactions of the Faraday Society*, vol. 9, no. 0, pp. 80–92, Jan. 1913, doi: 10.1039/tf9130900080.

[263] A. M. Mirsaeidi and F. Yousefi, “Viscosity, thermal conductivity and density of carbon quantum dots nanofluids: an experimental investigation and development of new correlation function and ANN modeling,” *J. Therm. Anal. Calorim.*, vol. 143, no. 1, pp. 351–361, Jan. 2021, doi: 10.1007/s10973-019-09138-z.

[264] K. Brzóska, B. Jóźwiak, A. Golba, M. Dzida, and S. Boncel, “Thermophysical Properties of Nanofluids Composed of Ethylene Glycol and Long Multi-Walled Carbon Nanotubes,” *Fluids*, vol. 5, no. 4, Dec. 2020, doi: 10.3390/fluids5040241.

[265] B. C. Pak and Y. I. Cho, “Hydrodynamic and heat transfer study of dispersed fluids with submicron metallic oxide particles,” *Experimental Heat Transfer*, vol. 11, no. 2, pp. 151–170, 1998, doi: 10.1080/08916159808946559.

[266] J. C. A. Maxwell, “A Treatise on Electricity and Magnetism,” *Nature*, vol. 7, no. 182, pp. 478–480, Apr. 1873, doi: 10.1038/007478a0.

10. Appendix

10.1. Appendix A

Element	Line	Intensity (c/s)	Atomic (wt.%)	Concentration (wt.%)
O	Ka	252.27	68.24	55.51
Al	Ka	488.35	15.50	21.27
Si	Ka	425.92	16.26	23.22
Total			100.00	100.00

EDX spectra and elemental composition for halloysite at one site

10.2. Appendix B

Processes	Temperature range	Mass loss	Heat effect
Loss of absorbed water	25-150 °C	2.0 %	Endothermic
Loss of interlayer water	150-400 °C	3.4 %	Endothermic
Dehydroxylation	400-700 °C	11.8 %	Endothermic

TG/DTG/DTA analysis result for halloysite

10.3. Appendix C

Element	Line	Intensity (c/s)	Atomic wt %	Concentration wt.%
O	Ka	38.48	66.74	53.338
Si	Ka	228.18	33.26	46.662
Total			100.000	100.000

EDX elemental composition for SiO_2 at one site

Element	Line	Intensity (c/s)	Atomic Wt %	Concentration wt.%
O	Ka	45.11	68.536	42.132
Ti	Ka	1272.85	31.464	57.868
Total			100.000	100.000

EDX elemental composition for TiO_2 at one site

10.4. Appendix D

Processes	Temperature range	Mass loss	Heat effect
Loss of absorbed water	25-245 °C	6.3 %	Endothermic
Oxidation of carbon	245-470 °C	93.7 %	Exothermic

TG/DTG/DTA analysis result for CNS

Processes	Temperature range	Mass loss	Heat effect
Loss of absorbed water	25-425 °C	3.9 %	Endothermic
Oxidation of carbon	425-700 °C	96.1 %	Exothermic

TG/DTG/DTA analysis result for CNP

10.5. Appendix E

Figure shows the percentage differences from the Prandtl–Kármán–Nikuradse friction factor calculation results for $Re = 5000$ and $Re = 17000$. While the seven other correlation results were symmetrical, the CFD simulation results were “one sided”. When the Re value was 5000, the friction factors were less, and when the Re value was 17000, the friction factors were higher than the references calculated by the Prandtl–Kármán–Nikuradse correlation. My observation indicated that the analysis of these results should be reserved for future studies.

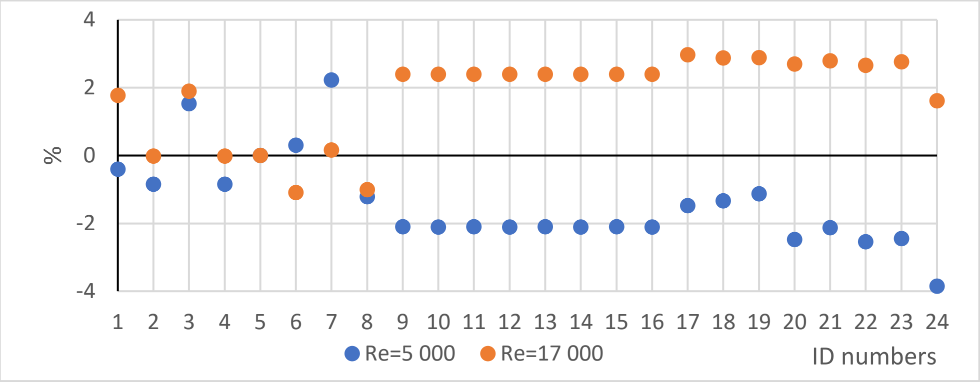

Percentage differences from the Prandtl–Kármán–Nikuradse friction factor.

10.6. Appendix F

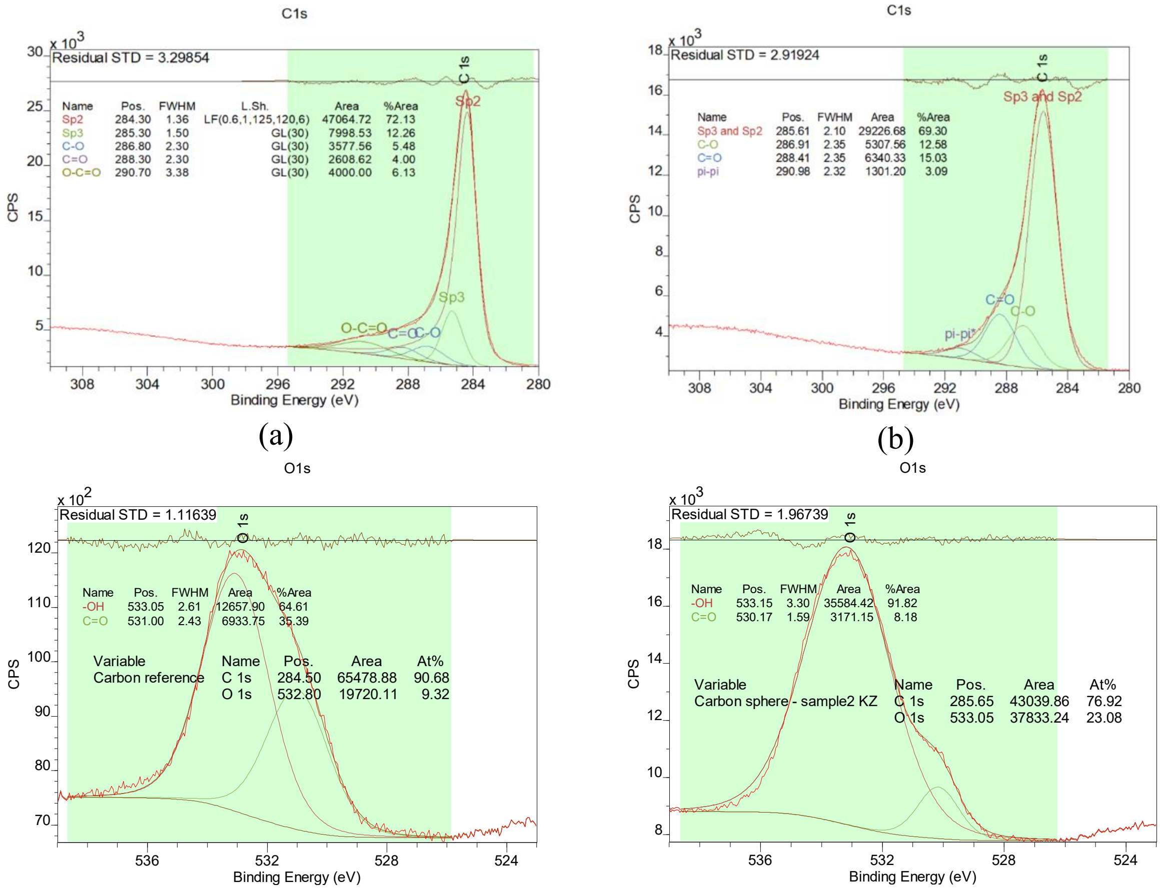

Name	Pos.	FWHM	L.Sh.	Area	%Area
Sp2	284.30	1.36	LF(0.6,1,125,120,6)	47064.72	72.13
Sp3	285.30	1.50	GL(30)	7998.53	12.26
C-O	286.80	2.30	GL(30)	3577.56	5.48
C=O	288.30	2.30	GL(30)	2608.62	4.00
O-C=O	290.70	3.38	GL(30)	4000.00	6.13

(a)

Name	Pos.	FWHM	Area	%Area
Sp3 and Sp2	285.61	2.10	29226.68	69.30
C-O	286.91	2.35	5307.56	12.58
C=O	288.41	2.35	6340.33	15.03
pi-pi	290.98	2.32	1301.20	3.09

(b)

Name	Pos.	FWHM	Area	%Area
-OH	533.05	2.61	12657.90	64.61
C=O	531.00	2.43	6933.75	35.39

Variable	Name	Pos.	Area	At%
Carbon reference	C 1s	284.50	65478.88	90.68
	O 1s	532.80	19720.11	9.32

(c)

Name	Pos.	FWHM	Area	%Area
-OH	533.15	3.30	35584.42	91.82
C=O	530.17	1.59	3171.15	8.18

Variable	Name	Pos.	Area	At%
Carbon sphere - sample2 KZ	C 1s	285.65	43039.86	76.92
	O 1s	533.05	37833.24	23.08

(d)

XPS spectra with calculation for (a) CNP at C1s region, (b) CNS at C1s region, (c) CNP at O1s region and (d) CNS at O1s region